

Accepted to ApJ on July 7, 2005

Chandra Deep X-ray Observation of a Typical Galactic Plane Region and Near-Infrared Identification

K. Ebisawa^{1,2,3}, M. Tsujimoto⁴, A. Paizis^{2,5}, K. Hamaguchi¹, A. Bamba⁶, R. Cutri⁷,
H. Kaneda⁸, Y. Maeda⁸, G. Sato⁸, A. Senda⁹, M. Ueno⁹, S. Yamauchi¹⁰, V. Beckmann¹,
T. J.-L. Courvoisier^{2,11}, P. Dubath^{2,11}, & E. Nishihara¹²

ebisawa@milkyway.gsfc.nasa.gov

ABSTRACT

Using the *Chandra* Advanced CCD Imaging Spectrometer Imaging array (ACIS-I), we have carried out a deep hard X-ray observation of the Galactic plane region at $(l, b) \approx (28.^\circ5, 0.^\circ0)$, where no discrete X-ray source had been reported previously. We have detected 274 new point X-ray sources (4σ confidence) as well as strong Galactic diffuse emission within two partially overlapping ACIS-I fields (~ 250 arcmin² in total). The point source sensitivity was

¹code 662, NASA/GSFC, Greenbelt, MD 20771

²INTEGRAL Science Data Centre, Chemin d'Écogia 16, 1290, Versoix, Switzerland

³Universities Space Research Association

⁴Department of Astronomy and Astrophysics, Pennsylvania State University, University Park, PA 16802

⁵IASF, Sezione de Milano, via Bassini 15, I-20133, Milano, Italy

⁶Cosmic Radiation Laboratory, RIKEN (The Institute of Physical and Chemical Research), 2-1, Hirosawa, Wako, Saitama 351-0198, Japan

⁷IPAC, California Institute of Technology, Mail Code 100-22, 770 South Wilson Avenue, Pasadena, CA 91125

⁸Institute of Space and Astronautical Science/JAXA, Yoshinodai, Sagamihara, Kanagawa, 229-8510 Japan

⁹Department of Physics, Kyoto University, Kitashirakawa Oiwake-cho, Sakyo-ku, Kyoto, 606-8502, Japan

¹⁰Faculty of Humanities and Social Sciences, Iwate University, Iwate, 020-8550, Japan

¹¹Observatory of Geneva, 51 chemin des Maillettes, 1290 Sauverny, Switzerland

¹²Gunma Astronomical Observatory, 6860-86 Nakayama Takayama-mura Agatsuma-gun Gunma, 377-0702, Japan

$\sim 3 \times 10^{-15}$ erg s $^{-1}$ cm $^{-2}$ in the hard X-ray band (2 – 10 keV) and $\sim 2 \times 10^{-16}$ erg s $^{-1}$ cm $^{-2}$ in the soft band (0.5 – 2 keV). Sum of all the detected point source fluxes accounts for only ~ 10 % of the total X-ray flux in the field of view. Even hypothesizing a new population of much dimmer and numerous Galactic point sources, the total observed X-ray flux cannot be explained. Therefore, we conclude that X-ray emission from the Galactic plane has truly diffuse origin. Removing point sources brighter than $\sim 3 \times 10^{-15}$ erg s $^{-1}$ cm $^{-2}$ (2– 10 keV), we have determined the Galactic diffuse X-ray flux as 6.5×10^{-11} erg s $^{-1}$ cm $^{-2}$ deg $^{-2}$ (2–10 keV). Only 26 point sources were detected both in the soft and hard bands, indicating that there are two distinct classes of the X-ray sources distinguished by the spectral hardness ratio. Surface number density of the hard sources is only slightly higher than that measured at the high Galactic latitude regions, indicating that majority of the hard sources are background AGNs. Following up the *Chandra* observation, we have performed a near-infrared (NIR) survey with SOFI at ESO/NTT. Almost all the soft X-ray sources have been identified in NIR and their spectral types are consistent with main-sequence stars, suggesting most of them are nearby X-ray active stars. On the other hand, only 22 % of the hard sources had NIR counterparts, which are presumably Galactic. From X-ray and NIR spectral study, they are most likely to be quiescent cataclysmic variables. Our observation suggests a population of $\gtrsim 10^4$ cataclysmic variables in the entire Galactic plane fainter than $\sim 2 \times 10^{33}$ erg s $^{-1}$. We have carried out a precise spectral study of the Galactic diffuse X-ray emission excluding the point sources. Confirming previous results, we have detected prominent emission lines from highly ionized heavy elements in the diffuse emission. In particular, central energy of the iron emission line was determined as $6.52^{+0.08}_{-0.14}$ keV (90 % confidence), which is significantly lower than what is expected from a plasma in thermal equilibrium. The downward shift of the iron line center energy suggests non-equilibrium ionization states of the plasma, or presence of the non-thermal process to produce 6.4 keV fluorescent lines.

Subject headings: Galaxy: structure — X-rays: stars — galaxies: active

1. INTRODUCTION

The Galactic X-ray source population has been studied from the very beginning of X-ray astronomy. The *Uhuru* satellite detected 339 X-ray sources all over the sky brighter than $\sim 2 \times 10^{-12}$ erg s $^{-1}$ cm $^{-2}$ in 2 – 10 keV (Forman et al. 1978). Most bright X-ray sources are

concentrated near the Galactic bulge and/or distributed along the Galactic plane, indicating their Galactic origin. A high sensitive X-ray observation with direct imaging was made for the first time with the *Einstein* satellite (Hertz and Grindlay 1984) in the soft X-rays below ~ 4 keV. The *ROSAT* Galactic Plane Survey (Motch et al. 1991) was made as a part of the *ROSAT* all sky survey, but the energy range was again limited to below ~ 2 keV. These soft X-ray surveys were not able to penetrate the Galactic heavy absorption ($N_H \approx 10^{23} \text{ cm}^{-2}$), hence did not allow us to observe those X-ray sources located deepest in the Galactic plane or behind.

In order to observe completely through the Galactic plane and to determine the Galactic source population, hard X-ray ($\gtrsim 2$ keV) observation is indispensable. This was made possible with *ASCA*, the first imaging satellite in the hard X-ray energy band (Tanaka, Inoue, & Holt 1994). *ASCA* carried out systematic surveys on the Galactic plane (Sugizaki et al. 2001) and the center region (Sakano et al. 2002) down to the sensitivity limit $\sim 3 \times 10^{-13} \text{ erg s}^{-1} \text{ cm}^{-2}$ in 2 – 10 keV. *ASCA*’s point source sensitivity was limited by source confusion due to its moderate X-ray mirror point spread function ($\sim 1'$). *ASCA* discovered more than two hundreds new X-ray sources on the Galactic plane region within the longitudes of $|l| \leq 45^\circ$ (Yamauchi et al. 2002; Ebisawa et al. 2003). Many of them are heavily absorbed and not detected in soft X-ray bands. *ASCA* suggested an intriguing possibility that there may be still more dimmer, undetected hard X-ray sources in the Galactic plane. *How many Galactic hard X-ray sources are there in the Galactic plane? What is the origin of dimmest Galactic hard X-ray sources?* Using *Chandra*, the most sensitive X-ray telescope in the history, we want to answer to these fundamental questions in X-ray astronomy.

Besides the discrete Galactic X-ray sources, the Galactic plane itself has been known to emit hard X-rays (e.g., Worrall et al. 1982; Warwick et al. 1985; Koyama et al. 1986). The emission forms a narrow continuous Galactic ridge, thus it is called the *Galactic Ridge X-ray Emission* (GRXE). GRXE exhibits emission lines from highly ionized heavy elements such as Si, S and Fe, which suggests that GRXE originates in thin hot plasmas with a temperature of several keV (Koyama et al. 1986; Yamauchi and Koyama 1993; Kaneda et al. 1997). Whether GRXE is composed of numerous point sources or truly diffuse emission has been a big problem for a long time. *ASCA* was expected to answer this crucial question, but not powerful enough to clearly separate numerous dim point sources and diffuse emission (Yamauchi et al. 1996; Kaneda et al. 1997; Sugizaki et al. 2001). The origin of GRXE remained unresolved with *ASCA*.

Chandra is an ideal satellite that is able to resolve GRXE into point sources with a superb spatial resolution of $\sim 0.''6$ (Weisskopf et al. 2002). For this purpose, using the *Chandra* Advanced CCD Imaging Spectrometer Imaging array (ACIS-I; Garmire et al. 2003), we have

carried out deep hard X-ray observations of the Galactic plane region at $(l, b) \approx (28.^\circ 5, 0.^\circ 0)$, where extensive observation had been already made but no discrete X-ray source detected with *ASCA*. Our first result was presented in Ebisawa et al. (2001); we have found that only $\sim 10\%$ of the hard X-ray flux ($2 - 10$ keV) in the *Chandra* field is explained by the point sources brighter than $\sim 3 \times 10^{-15}$ erg s $^{-1}$ cm $^{-2}$. Also, by comparing the observed source number density with those measured at high Galactic regions, we suggested that most of these hard X-ray point sources on the Galactic plane are background AGNs.

We have made two slightly overlapping *Chandra* deep observations for our project, only the first one was analyzed in Ebisawa et al. (2001). In the present paper, we will give full analysis of our two *Chandra* observations, as well as the result of near-infrared (NIR) follow-up observation using the New Technology Telescope (NTT) at the European Southern Observatory (ESO). Main purposes of this paper are the following; (1) to study nature of the dimmest X-ray point sources on the Galactic plane in details using X-ray and NIR data, (2) to constrain the population of faint Galactic hard X-ray sources, and (3) to investigate for origin of the Galactic diffuse emission through precise spectral analysis. Clean separation of the diffuse emission and the point sources has been made possible for the first time by superb *Chandra* spatial resolution.

2. OBSERVATION AND DATA REDUCTION

2.1. X-ray Observation and Data Reduction

We observed the “empty” Galactic plane region at around $(l, b) \approx (+28.^\circ 5, 0.^\circ 0)$ in order to study the Galactic diffuse X-ray emission and dim point X-ray sources. This direction is toward the Scutum arm and is known to have strong diffuse emission, thus already extensively observed with *ASCA* (Yamauchi et al. 1996; Kaneda et al. 1997). *ASCA* did not detect any point sources brighter than $\sim 2 \times 10^{-13}$ erg s $^{-1}$ cm $^{-2}$ ($2 - 10$ keV), while found an intriguing hard X-ray diffuse feature (AX J1843.8–0352; Bamba et al. 2001), which was another motivation for our *Chandra* observation in this region. Using ACIS-I, we carried out each 100 ksec pointing on February 25, 2000 (AO1; sequence number 900021) and May 20, 2001 (AO2; sequence number 900125), respectively, with slightly overlapping fields. The total area of the observed field is ~ 250 arcmin 2 . Detailed spatial and spectral study of AX J1843.8–0352 using both AO1 and AO2 observations was already published in Ueno et al. (2003).

In this paper, we use the event data processed by the *Chandra* X-ray Center with the latest processing system in early 2003. Furthermore, we have applied position and energy

calibration (CTI correction) using the CIAO package (version 3.0.1). The Two Micron All Sky Survey (2MASS)¹ was adopted for the astrometric reference for the *Chandra* data as well as the NTT/SOFI data (see Section 2.3). Using the positions of those *Chandra* sources that have obvious NIR counterparts, we estimate our *Chandra* position accuracy as $\sim 0.''6$ (see also Section 3.4), which is limited by statistical error and distortion of the point spread function for off-axis sources.

2.2. X-ray Point Source Extraction

First, we made exposure and vignetting corrected images in 0.5 – 2 keV, 2 – 4 keV and 4 – 8 keV, and superposed them by assigning red, green and blue color respectively, followed by adaptive smoothing to enhance visibility (Fig. 1). We can clearly see many point sources as well as strong diffuse emission. We carried out point source search using the “wavdetect” program in the CIAO data analysis package. We searched for sources in the 0.5 – 3 keV (soft band), 3 – 8 keV (hard band) and 0.5 – 8 keV (total band) independently. We did not use data below 0.5 keV and above 8 keV for the source detection in order to avoid high backgrounds in both energy ends. Sources that exceed 4σ significance (given by “wavdetect”) in any of the three energy bands were considered to be true detections. On the AO1 and AO2 overlapping field, we searched for the sources in the AO1 and AO2 data separately, and combined the two significances quadratically. We have detected 274 point sources within the total field of view. Source position and significance in each energy band are given in Table 1. Position errors are the statistical ones calculated by wavdetect, not including any systematic errors.

None of these point sources have been reported in X-rays before. In the soft band, 182 sources have been detected, while in the hard band 79 sources. Only 26 sources were detected both in the soft and hard bands, suggesting an intriguing dichotomy in the source population (see Sections 3.3 and 3.4 for more details). Those 4σ sources near the on-axis roughly corresponds to $\sim 3 \times 10^{-15}$ erg s⁻¹ cm⁻² (2 – 10 keV) or $\sim 2 \times 10^{-16}$ erg s⁻¹ cm⁻² (0.5 – 2 keV), depending on the spectral hardness ratio and assumed spectral shapes (Section 3.2).

A new acronym “CXOGPE” (Galactic Plane sources reported by Ebisawa et al. 2005) is registered at CDS² for the sources in Table 1. Hence, the first source in Table 1 at

¹<http://www.ipac.caltech.edu/2mass>

²<http://vizier.u-strasbg.fr/viz-bin/DicForm>

(18:42:51.77, $-3^{\circ}51'11.''2$) may be formally designated as “CXOGPE J184251.7–035111”, and so on. In this paper, however, the sources in Table 1 are referred as Source 1, 2, etc. for simplicity.

Sources 208, 210, 213, and 216, detected at around (R.A., Decl.) = (18 : 43 : 57, $-3^{\circ}54'48''$) seem to be parts of a single extended feature, which is designated as CXOU J184357-035441 by Ueno et al. (2003). This extended feature has a characteristic thermal spectrum (Ueno et al. 2003), and is probably a blob associated with the supernova remnant AX J 1843.8–0352/G28.6–0.1 (Bamba et al. 2001). All the other sources are consistent with the *Chandra* point spread function, thus they are considered as point sources.

2.3. NIR Observation and NTT/SOFI Data Reduction

Because of the heavy Galactic absorption, the NIR band has a great advantage over the optical waveband to identify dim X-ray sources on the Galactic plane. In fact, radio observation toward our field has been made (Dickey and Lockman 1990; Dame, Hartman and Thaddeus 2001; Minter et al. 2001), and the total hydrogen column density was estimated not less than $\sim 6 \times 10^{22} \text{ cm}^{-2}$ (Ebisawa et al. 2001). This corresponds to $A_V \approx 33 \text{ mag}$ using the standard extinction formula ($N_H/A_V \approx 1.8 \times 10^{21} \text{ cm}^{-2} \text{ mag}^{-1}$; Predehl and Schmitt 1995), so that there is hardly a hope to identify extragalactic sources or the most distant Galactic sources in the optical band. On the other hand, NIR extinction formulas $N_H/A_J \approx 5.6 \times 10^{21} \text{ cm}^{-2} \text{ mag}^{-1}$ (Vuong et al. 2003) and $N_H/E(J - K) \approx 10^{22} \text{ cm}^{-2} \text{ mag}^{-1}$ (Harjunpää and Mattila 1996) lead to $A_J \approx 11 \text{ mag}$ and $A_K \approx 5 \text{ mag}$, hence NIR extinction is much smaller, and NIR observation will allow us to probe deeper into the Galactic plane.

The 2MASS database covers all the sky, and its Point Source Catalog gives the accurate positions and J , H and K_S magnitudes of all the major stars in our *Chandra* field of view (Fig. 2). In order to study more deeply than 2MASS, we have carried out a NIR follow-up observation at ESO using NTT (Tarenghi and Wilson 1989) with the SOFI infrared camera during the nights of 2002 July 28th and 29th. SOFI has 1024×1024 HgCdTe pixels with a moderately large field of view ($4.''94 \times 4.''94$). The pixel size is $0.''2884$, which is comparable to the *Chandra* one ($\sim 0.''5$ pixel), thus very suitable to identify *Chandra* X-ray sources. We performed a mosaic observation composed of the 16 pointings slightly-overlapping each other to cover the central region of the two *Chandra* fields (Fig. 3). We defined seven central “A” fields and nine surrounding “B” fields to cover $\sim 75\%$ of the total *Chandra* field. The total exposure times for J , H and K_S bands for each A-field are 10, 10, and 14 minutes, respectively, and those for each B-field are 5, 5, and 7.47 minutes respectively. According

to the standard SOFI observation procedure, we carried out a dithering observation, such that each field is covered by 5 (J and H band in B-field), 8 (K_S band in B-field), 10 (J and H band in A-field) or 15 (K_S band in A-field) sequential “frames”, each jittered by $\sim 40''$. Exposure time for each frame was 60 (J and H bands) or 56 seconds (K_S band), and each frame was furthermore divided into 6 (J and H bands) or 8 (K_S band) read-out segments in order to avoid saturation. Thus, each frame was the average of the 6 (J and H bands) or 8 (K_S band) snap-shot images. The seeing was best in the first night ($\sim 0.''6$) when we observed fields A1 through A6 (but only H and K_S bands for A6), whereas in the second night, the seeing was worse ($\sim 1.''5$) when we observed the remaining fields.

IRAF³ was mainly used to reduce the data following the standard procedure, i.e., subtraction of the dark current, flat-fielding using the dome flat, subtraction of sky using the median-sky technique, removal of bad pixels and cosmic-ray events, and trimming the frame edges. SExtractor (Bertin & Arnouts 1996) was used to extract sources. We searched for sources in each J , H and K_S band separately, and detected 16,890, 26,285 and 27,174 sources (with the DETECT_MINAREA, DETECT_THRESH, and ANALYSIS_THRESH SExtractor parameter values 5, 1.5, and 1.5, respectively) in J , H and K_S bands, respectively. After removing the overlapping sources, 32,398 sources have been detected at least in one of the three bands (Table 2).

Using the 2MASS database as a reference, we have carried out astrometric correction and absolute magnitude calibration. In Fig. 4, we compare 2MASS and SOFI positions after the astrometric correction. The standard deviation of the shifts between 2MASS and SOFI is $0.''2$ in R.A. and Decl., which is smaller than the SOFI pixel size ($0.''2884$), and may be taken as a typical 2MASS and/or SOFI positional uncertainty. Considering the 2MASS source within $0.''2884$ radius as a counterpart, 8,655 SOFI sources are identified in 2MASS (Table 2).

In Fig. 5 we show correlation of the 2MASS and SOFI J , H and K_S magnitudes after the photometric correction. SOFI magnitudes tend to be greater than those of 2MASS for sources brighter than ~ 10 mag, where SOFI starts to saturate. Also, there is increasing confusion in the 2MASS-SOFI correlation for stars fainter than $J \approx 14$, $H \approx 13$ and $K_S \approx 12$, because of the relatively large 2MASS pixels. This leads to the increasing scatter in the 2MASS-SOFI photometric comparison. For the cleanest samples between 10 and 12 mag, the standard deviations of the 2MASS – SOFI magnitude differences are 0.08, 0.10, and

³IRAF (Image Reduction and Analysis Facility) is distributed by the National Optical Astronomy Observatories, which are operated by Association of Universities for Research in Astronomy, Inc., under cooperative agreement with the National Science Foundation.

0.12 mag in J , H , and K_S bands, respectively (for comparison, the 2MASS measurement precision for bright, non-saturated sources is ~ 0.01 to 0.02 mags). These values may be considered as our typical photometric uncertainties.

In Fig. 6 we show cumulative histograms of the SOFI and 2MASS sources as a function of the SOFI magnitudes. We can see that our sample is almost complete down to ~ 18 , 17 or 16 mag in J , H , or K_S bands, respectively, if we assume extrapolation of the power-law source distribution at the brighter counts. The depletion of the sources dimmer than these limiting magnitudes may be due to our sensitivity limit and/or depletion of the intrinsic source population. We can also see the depth of our SOFI observation relative to 2MASS which saturates at around ~ 16 , 15 or 14 mag in J , H , or K_S bands, respectively.

Finally, we estimate our SOFI sensitivity for normal stars. We assume an A0 star with the K -band absolute magnitude $M(K) = 0$. At the sensitivity 16 mag in the K -band, we would be observing the A0 star as far as ~ 7 kpc, since the source will have $m(k) = 14.2$ mag without reddening, and $A(K) \approx 1.6$, assuming $N_H/A_K \approx 1.3 \times 10^{22} \text{ cm}^{-2} \text{ mag}^{-1}$ and an interstellar hydrogen density of $n_H \approx 1 \text{ cm}^{-3}$.

3. DATA ANALYSIS AND RESULTS

3.1. Separation of the Diffuse Emission and Point Sources

One of the main goals of the present observation is to separate the diffuse X-ray emission from the point sources, and to study the diffuse spectrum free from the point source contamination. We have extracted an energy spectrum from both AO1 and AO2 data excluding the AX J 1843.8–0352/G28.6–0.1 region (marked in Fig. 1). Using the non-X-ray background database provided by *Chandra* X-ray Center (CXC), we have subtracted the background spectrum.

The CXC background database is constructed from a set of blank sky observations at high Galactic latitudes excluding recognized celestial sources. We have made background spectrum for each CCD chip, and the relative normalization of the background subtraction was adjusted for each chip and pointing to cancel the X-ray flux in the range of $10.5 - 12.5$ keV (where ACIS is not sensitive to X-rays; Fig. 7). Note that there are several conspicuous instrumental lines in the background spectrum (Fig. 7; Townsley et al. 2002a,b). After background was subtracted for each chip and pointing in this manner, all the spectra from different chips and pointings have been combined for subsequent spectral study. After the background is thus subtracted, our spectrum is expected to include only point X-ray sources (Galactic and extragalactic) and Galactic plane diffuse emission. We notice that our results

on the Galactic diffuse emission may not escape from uncertainty of the background subtraction. For example, the CXC background might include local soft diffuse emission which is presumably higher at high Galactic latitudes. However, in the 2 – 10 keV energy band, which we are most interested in, the particle background dominates, and its normalization may be correctly estimated (Fig. 7).

We have made an energy spectrum combining all the point sources in Table 1, subtracting the background in the same manner. In Fig. 8, we show the total energy spectrum and the combined point source spectrum, as well as the difference between the two. We can see that only $\sim 10\%$ of the total X-ray emission in the *Chandra* field of view is explained by the sum of all the detected point sources. Therefore, the difference spectrum, explaining $\sim 90\%$ of the total flux, is considered to be mostly the Galactic diffuse emission, though it should include some contribution from the point sources below our detection threshold (see detailed discussion in Section 4.4). We can see that emission lines from highly ionized heavy elements are associated with the diffuse emission. Although presence of the various emission lines in GRXE has been known for a long time (e.g., Koyama et al. 1986; Yamauchi and Koyama 1993; Kaneda et al. 1997), it is now clearly seen that these emission lines are from the diffuse emission, not from the point sources. More detailed diffuse emission spectral analysis is presented in Section 3.6.

3.2. Spectral Hardness-ratio and Source Fluxes

In order to study spectral characteristics of these new point sources, we computed energy flux and spectral hardness ratio (HR) for each source. The detected raw source counts do not represent the correct source intensities, since they are affected by positional dependence of the detector response (mostly mirror vignetting). Hence, we define and calculate the “normalized count rate” for each energy band, that is the count rate expected when the source is located on the ACIS-I aim point (on-axis direction) and observed for 100 ksec exposure. We define the spectral hardness ratio as $HR \equiv (H - S)/(H + S)$, where H is the normalized count rate in the hard energy band (3 – 8 keV), and S is that in the soft energy band (0.5 – 2 keV). The normalized count rates and HR are also shown in Table 1.

To determine source energy fluxes, we need to assume spectral models, but most sources are too dim to determine their energy spectra individually. Therefore, we took the following approach: first, energy spectra are extracted for all the sources, and corresponding instrumental responses were calculated. We categorized the sources into four spectral groups according to the hardness ratio; $HR < -0.8$, $-0.8 \leq HR < -0.2$, $-0.2 \leq HR < 0.6$ and $0.6 \leq HR$. For each spectral group, all the source spectra and responses were averaged. The

background spectrum was extracted in the blank detector field for AO1 and AO2 separately, and subtracted from the average spectra (thus, the Galactic diffuse emission is subtracted). Then, we fitted these four average spectra with an absorbed power-law model, and determined the average hydrogen column density and power-law index for each spectral group. The best-fit spectral model parameters, from the softest spectrum to the hardest one, are the following : $N_H = 0.66, 0.83, 3.4$ and $8.0 \times 10^{22} \text{ cm}^{-2}$ and photon-index = 4.0, 2.1, 1.9 and 1.2. As expected, the higher the HR goes up, the larger the absorption becomes and the flatter the spectral slope is. Finally, each source in the same spectral group was “fitted” with the average spectral model after background subtraction, only by adjusting the normalization. From the spectral model thus determined for each source, we calculated the 0.5 – 2 keV and 2 – 10 keV energy fluxes (Table 1). Note, individual source energy fluxes thus estimated may not help suffering from uncertainty of the spectral assumption. However, if we integrate all the sources, the *total* point-source energy flux should be valid, since we have assumed the average source spectrum for each spectral group.

3.3. $\log N - \log S$ and Source Population

We study the point source number densities with the $\log N - \log S$ analysis in the hard band (2 – 10 keV) and soft band (0.5 – 2 keV) separately, adopting the source energy fluxes determined above (Fig. 9). The $\log N - \log S$ curve in the hard band using only the AO1 data was already presented in Ebisawa et al. (2001). We set the lower flux limits at $3 \times 10^{-15} \text{ erg s}^{-1} \text{ cm}^{-2}$ in the hard band and $2 \times 10^{-16} \text{ erg s}^{-1} \text{ cm}^{-2}$ in the soft band, respectively, which approximately correspond to the 4σ detection limits near the on-axis.

We compare our Galactic plane $\log N - \log S$ curves with those of bright *ASCA* Galactic sources (Sugizaki et al. 2001), extragalactic point sources detected with *ASCA* (Ueda et al. 1999), *ROSAT* and *Chandra* (Giacconi et al. 2001). The extragalactic sources are significantly absorbed on the Galactic plane with a hydrogen column density of $N_H \approx 6 \times 10^{22} \text{ cm}^{-2}$ (Section 2.3). Assuming a typical photon index of 1.7, we took into account the flux reduction due to the Galactic absorption, and made $\log N - \log S$ curves of the extragalactic sources expected to be seen through the Galactic plane (dashed lines in Fig. 9).

Let’s compare our Galactic plane $\log N - \log S$ curves with those for extragalactic sources. In the soft energy band, number of the *Chandra* sources detected above the lowest flux limit is more than 20 times higher than that expected from the extragalactic sources through the Galactic plane (dashed line). Therefore, it is no doubt that most of the soft sources are Galactic. On the other hand in the hard energy band, the situation is quite different; the extragalactic $\log N - \log S$ curve explains most of the observed sources on the

Galactic plane. Hence, the observed dichotomy of the source population (Section 2.2) may be naturally explained in that *most of the soft X-ray sources have the Galactic origin, while majority of the hard X-ray sources are extragalactic.*

3.4. NIR Identification and Source Classification

We may classify the new X-ray sources according to the HR . We define the “soft” sources whose HR are equal or less than the median $HR = -0.60$. For the rest, the median is $HR = 0.11$, so the “medium” and the “hard” sources are defined as those with $-0.59 < HR \leq 0.10$ and $0.1 < HR$, respectively. Excluding the sources obviously associated with the extended structure CXOU J184357-035441 (Ueno et al. 2003), number of the soft, medium and hard sources we have detected is 136, 65 and 69, respectively (Table 3). Also, we plot the locations of the soft, medium and hard *Chandra* sources on the 2MASS image with different colors (Fig. 2).

Our *Chandra* position accuracy is mostly limited by photon statistics and distortion of the point spread function. We may expect an error of $\sim 1''$ for dim sources far from the aim points. We consider the NIR sources found within $\sim 1''$ of the *Chandra* positions as counterparts. For the *Chandra* sources in the SOFI fields ($\sim 75\%$ of all the *Chandra* sources; Table 3), we show SOFI counterparts in Table 1. 2MASS counterparts are given in Table 1 for the *Chandra* sources outside of the SOFI fields.

The SOFI detected $\sim 32,000$ sources (Table 2) from the $\sim 0.08 \text{ deg}^2$ field (Fig. 2 and 3), namely, the SOFI source number density is $\sim 0.03 \text{ arcsec}^{-2}$. Therefore, within $1''$ circle around any *Chandra* sources, ~ 0.1 SOFI source is expected by chance. In other words, we should be reminded that $\sim 10\%$ of the *Chandra* sources will have accidental SOFI counterparts.

In Fig. 10, for each of the *Chandra* sources in the SOFI fields, we plot the relative positional difference to the nearest SOFI source. It is easily seen that most of the soft sources have the NIR counterparts, while medium and hard sources are less likely to have counterparts. In fact, the percentage of the *Chandra* sources having the SOFI counterparts is 83, 53, and 22 % for soft, medium, and hard sources, respectively (Table 3). For all the *Chandra* sources, the percentage with 2MASS counterparts is 45, 26 and 12 %, respectively (Table 3). The fact that the detectability of the NIR counterparts decreases with HR is consistent with the idea that most soft sources are Galactic, while most hard sources are extragalactic. In fact, if these hard X-ray sources are background AGNs, assuming a typical X-ray/NIR luminosity ratio and the significant Galactic extinction, they are too dim to

be detected in the NIR band (see Section 4.1). Examples of the NIR counterparts for the *Chandra* sources are shown in Fig.11. This is for the SOFI “A4” field (Fig. 3), which is covered by both AO1 and AO2 observations. Note that all the 16 soft and medium sources have NIR counterparts, though none of the four hard X-ray sources are identified.

In Fig. 12 (top), we show histograms of the number of sources as a function of HR . It is curious to see that the softest sources are most numerous, and that the number of sources first decreases with HR till $HR \sim 0.5$ and then increases again. On the other hand, number of the sources having NIR counterparts decreases monotonically with increasing HR . This also suggests that our source population is composed of the two distinct spectral classes, the most numerous Galactic soft sources and the less numerous extragalactic hard sources.

The bottom panel of Fig. 12 shows the normalized X-ray counting rates (Section 3.2) versus HR , as well as presence or absence of the NIR counterpart for each source. We see that almost all the soft sources have NIR counterparts except several dimmest ones. On the other hand for the hard sources, presence or absence of the NIR counterparts is not related to the X-ray brightness. Those identified soft X-ray sources are presumably nearby stars, and the small number of unidentified soft sources are considered to be farther NIR dim stars (see also Section 3.5.2). The hard X-ray sources without NIR counterparts are mostly likely to be background AGNs, whose fluxes are distributed in a wide range. In particular, the brightest hard source (Source 200) is not identified in NIR, thus considered to be a strong AGN candidate.

3.5. X-ray Characteristics of the Point Sources

3.5.1. X-ray Spectra/Hardness

Since most X-ray sources are too dim (as low as ~ 10 counts) to make individual spectra, we combined the sources having similar spectral hardness and made average energy spectra to investigate their spectral characteristics as a class. We categorized all the point sources into six groups, three ranges of the X-ray spectral hardness (Section 3.4), and further grouped according to the presence or absence of the NIR counterparts. We made an averaged energy spectrum for each group.

In Table 4, we show the spectral parameters of the six spectra fitted with a simple absorbed power-law model to quantify spectral characteristics. For a given spectral hardness, the photon index was determined for the group having more sources, either with or without NIR counterpart, and fixed for the other group. This helps to clarify the difference of the hydrogen column densities and normalizations between the two groups in the same spectral

hardness.

Since the hydrogen column density can be a measure of the distance to the sources, the gradual increase of the column density from soft to hard suggests that the medium and the hard sources are more likely to be located further than the soft sources. Also, the medium and hard sources without NIR counterparts show clear excess of the hydrogen column densities compared to those with the counterparts, which implies that the the sources without NIR counterparts tends to locate further (presumably extragalactic) than those with NIR counterparts (likely to be Galactic). Interestingly, in spite that the sources without NIR counterparts are presumably further, they are *brighter* in both the observed fluxes and the intrinsic fluxes than the sources with NIR counterparts (Table 4). This will make sense that most hard and medium sources are background AGNs which are bright in X-rays but not seen NIR.

On the other hand, if we compare the soft sources without NIR counterparts and those with counterparts, the average X-ray energy flux of the formers is ~ 40 % smaller than the latter (Table 4). This suggests that the soft X-ray sources without NIR counterparts are further than and/or intrinsically dimmer than those with NIR counterparts. This makes sense considering that almost all the soft sources are X-ray active stars in the Galaxy.

3.5.2. Spectral Fitting

In the previous section, we used a simple absorbed power-law model to study the difference of the six average spectra (Table 4). Here, we fit the average source spectra with more physically meaningful models, and also study the iron line feature more carefully.

The X-ray energy spectrum of an active stars is characterized by a two temperature plasma model. Therefore, we used a two temperature MEKAL model in XSPEC (version 11.3.1) for the soft spectrum with NIR counterparts. The spectrum is well fitted with a two temperature plasma at 0.2 keV and 2.0 keV (Table 5). An ionized iron emission line is expected from the high temperature plasma, and indeed there is an evidence of iron emission line though not very strong (Fig. 13, top left). Assuming that the soft sources without NIR counterpart have the same X-ray spectral properties, we tried exactly the same spectral model (including N_H) and allowed only the overall normalization to be a free parameter. We found the fit is reasonably well, with 52 % of the normalization of the soft sources with NIR counterpart (Fig. 13, top right). So, soft X-ray sources without NIR counterparts are dimmer in X-rays than those with NIR counterparts due to intrinsic low X-ray and NIR luminosity and/or due to large distances.

Average energy spectrum of the hard sources with NIR counterparts exhibits a conspicuous narrow iron emission line (Fig. 13, bottom left). The line center energy is 6.67 keV and the equivalent width is 540 eV (Table 5). These iron line parameters and the flat spectrum (photon-index = 1.47) correspond to a plasma temperature of $kT \sim 8$ keV. Such a high temperature thermal spectrum is a characteristic of quiescent cataclysmic variables (e.g., Ezuka and Ishida 1999). In fact, cataclysmic variables have been considered prime candidates for faint Galactic hard X-ray sources (e.g., Mukai and Shiokawa 1993; Verbant et al. 1997; Watson 1999). On the other hand, the hard sources without NIR counterparts do not show a narrow iron emission line, but have a broad line and an edge feature which may be modeled with a neutral iron edge (at 7.11 keV) and a broad emission line (at 6.67 keV, EW = 340 eV). These iron features as well as the flat spectrum (photon-index = 0.77) are reminiscent of the disk reflection spectrum often seen in Type II AGN.

The average spectrum of medium sources with NIR counterpart can be fitted with two temperature plasma model, in which the soft component temperature (0.2 keV) is similar to that of the soft spectrum but the hard component temperature is higher (2.9 keV), suggesting a mixture of the relatively hot stars and soft cataclysmic variables. The average spectrum of medium sources without NIR counterpart can be fitted with a power-law which is steeper and less absorbed than the hard sources, presumably indicating a composite of faint hot stars and soft AGNs. A schematic view is shown in Fig. 14 for classification of the X-ray sources based on X-ray spectral hardness ratio and presence or absence of the NIR counterparts.

3.5.3. Time Variation

We study time variation of the point sources. For each source, we have made two light curves with bin-widths of 3,000 sec and 10,000 sec. We performed the Kolmogorov-Smirnov test, and if both light curves show variations above 99.9 % significance level, we consider the source to be significantly variable. In our sample, 17 sources are found to be variable, which are marked in Table 1 (“*T*” in the first column). The distribution of the hardness ratio for these variable sources is shown in Fig. 12 (blue circles). Flare-like variation of “rapid-rise and slow-decay”, which is distinctive to X-ray active stars, has been found from seven sources (Fig. 15). The average *HR* of these seven sources is -0.51 , which reinforces our idea that nature of these sources is X-ray active stars.

3.6. Spectral Study of the Diffuse X-ray Emission

3.6.1. Line Emission

First, we concentrate on the iron and other emission lines of the diffuse emission. We fit the iron energy band (5.5 – 7.2 keV) and soft energy band (0.8 – 3.5 keV) separately with a simple power-law plus gaussian model, and determine the line parameters.

We point out that ACIS-I iron line measurement has a significant merit in that contaminating instrumental iron line, which was problematic in *ASCA* and *XMM-Newton* diffuse spectral study, is almost fully negligible. In the iron energy band, a single narrow gaussian model is successful (Table 6; Fig. 16, top). The central line energy is $6.52^{+0.08}_{-0.14}$ keV (90 % error), which is consistent with Kaneda et al. (1997; 6.61 ± 0.02 keV), and significantly lower than what expected from He-like iron in a thermally equilibrium plasma (6.67 keV). A possible explanation of the line energy shift is that the plasma is in non-equilibrium ionization (NEI) state (Yamauchi and Koyama 1993; Kaneda et al. 1997), or the line is composed of a fluorescent 6.4 keV line and a thermal 6.67 keV line (Valinia et al. 2000b). Considering the latter possibility, we fit the same spectrum with a multiple line model. In addition to these two lines, if the charge exchange takes place between the cosmic-ray iron nuclei and interstellar hydrogen atoms (Tanaka, Miyaji, & Hasinger 1999; Tanaka 2002), a hydrogenic iron line at 6.97 keV is expected. Thus, we fit the observed spectrum with the three lines with fixed energies (Table 6; Fig. 16, bottom). The fit is acceptable, though slightly worse than with the single line model. The cosmic-ray charge exchange model predicts significantly broadened emission lines due to the energetic cosmic-ray bulk motion (Tanaka, Miyaji, & Hasinger 1999; Tanaka 2002), but from our statistics we could not constrain the intrinsic iron line width.

We found that the iron line equivalent width in GRXE is significantly dependent on the spectral model, and difficult to be determined uniquely. With a single narrow line model we obtained $EW = 170 \pm 120$ eV, which is smaller than the *ASCA* value with the same model and same sky region, 405 ± 80 eV (Kaneda et al. 1997). Contamination of the point sources with strong iron emission in the *ASCA* spectrum might explain the different at least to some extent. On the other hand, with the three line model, our equivalent width values are $100 \pm^{50}_{100}$ eV, $180 \pm^{360}_{140}$, and $160 \pm^{260}_{160}$ eV, which are consistent with the *ASCA* result using the same three line model on the same sky, < 70 eV, 280 ± 70 and 120 ± 70 eV (Tanaka 2002), though errors are large.

Similarly, the soft band energy spectrum was fitted with a power-law continuum and eleven gaussians (Table 7; Fig. 17). These are the same lines detected in *ASCA* (Kaneda et al. 1997), with an additional line at 2.19 keV which probably originates in the instrumental

Au M complex (Fig. 7). Equivalent width values are consistent with those in Table 4 in Kaneda et al. (1997), except that we find weaker 1.74 keV (low ionized Si) and 2.00 keV (Si XIV, Ly α) lines.

3.6.2. *Fit with Non-Equilibrium Ionization Plasma Model*

We now try to fit the observed diffuse spectrum with a more physically reasonable model. As a working hypothesis, we adopt the same spectral model used by Kaneda et al. (1997), which is a two temperature NEI model (Masai 1984), such that there are soft and hard NEI components which have different temperatures, normalizations, ionization parameters and are affected by different amounts of interstellar absorption.

First, we fix the element abundances for the soft component and hard component, respectively (Table 8 left; Fig. 18 top). The fit is not satisfactory (reduced $\chi^2 = 1.97$), and in particular, the observed iron and neon emission lines are not explained. Next, we adjust abundances of Ne, Mg, and Si in the soft component, and Fe abundance in the hard component (Table 8 right; Fig. 18 bottom). Now the fit is better (reduced $\chi^2 = 1.52$), though artificial adjustment of the abundances is unexplained. Still, we notice a hint of high energy excess above iron line energy, which may be related to the non-thermal component reported above ~ 10 keV (Yamasaki et al. 1997; Valinia et al. 2000b).

With the two component model fit, we have determined the observed flux from the soft and hard component as 2.6×10^{-8} and 2.1×10^{-7} erg cm $^{-2}$ s $^{-1}$ str $^{-1}$ (0.7 – 10 keV), respectively. Note that the observed flux and spectral shape are significantly affected by the heavy interstellar absorption (Fig. 19). Although the soft component is dominant in the observed flux below 2 keV, the hard component is more dominant over the entire energy band if absorption is removed. If the absorption is removed, the intrinsic fluxes are 1.1×10^{-7} and 7.6×10^{-7} erg cm $^{-2}$ s $^{-1}$ str $^{-1}$ (0.7 – 10 keV) from the soft and hard component, respectively⁴.

⁴Using the same two component model, Kaneda et al. (1997) gave the intrinsic (= absorption removed) soft and hard component fluxes 1.9×10^{-6} and 5.3×10^{-7} erg cm $^{-2}$ s $^{-1}$ str $^{-1}$ (0.5 – 10 keV), respectively. We remark that, in the NEI models we assume, strong oxygen lines are expected between 0.5 keV and 0.7 keV (Fig. 19), which are hardly observable below the low energy thresholds of both *ASCA* and *Chandra*. Therefore, it will be more reasonable to compare the fluxes in 0.7 – 10 keV, not in 0.5 – 10 keV. Calculated from the NEI model parameters by Kaneda et al. (1997), the observed soft and hard component fluxes with *ASCA* are 5.3×10^{-8} and 1.2×10^{-7} erg cm $^{-2}$ s $^{-1}$ str $^{-1}$ (0.7 – 10 keV), respectively, and the intrinsic soft and hard component fluxes are 1.9×10^{-7} and 4.3×10^{-7} erg cm $^{-2}$ s $^{-1}$ str $^{-1}$ (0.7 – 10 keV), respectively. Note that excluding the 0.5 – 0.7 keV energy range makes the intrinsic soft component flux 10 times less. Flux difference between *ASCA* and *Chandra* is discussed in Section 4.3.

4. Discussion

4.1. Origin of the Faint X-ray Point Sources on the Galactic Plane

We have detected 270 point X-ray sources (above 4σ significance) on a typical Galactic plane field at around $(l, b) \approx (28.^\circ5, 0.^\circ0)$ within ~ 250 arcmin², down to the flux limits $\sim 3 \times 10^{-15}$ erg s⁻¹ cm⁻² (2 – 10 keV) or $\sim 2 \times 10^{-16}$ erg s⁻¹ cm⁻² (0.5 – 2 keV). Thereby we extended the X-ray $\log N - \log S$ curves on the Galactic plane to much dimmer levels than previous observations. In the brightest ends, our $\log N - \log S$ curves match well with those by *XMM-Newton* (Hands et al. 2004) and *ASCA* (Sugizaki et al. 2001) carried out on larger Galactic plane regions.

Based on the X-ray spectral properties and presence or absence of the NIR counterparts, we have proposed a schematic view for origin of the point X-ray sources on the Galactic plane; soft X-ray sources are nearby active stars, whereas hard X-ray sources without NIR counterpart are extragalactic and hard sources with NIR counterpart are Galactic cataclysmic variables (Fig. 14). In the following, we are going to confirm this simple picture through more detailed analysis.

Considering background AGNs, assuming typical X-ray fluxes (Table 4) and a broad-band photon-index of 2 (flat energy spectrum in the νF_ν plot), we estimate the expected J , H and K_S magnitudes as 21 mag to 23 mag. Taking into account the further reddening $A_K \approx 5$ (Section 2.3), there is no hope to detect those background AGNs in NIR through the Galactic plane. Therefore, we may assume that all the sources with NIR identification are Galactic.

To better understand properties of the Galactic point sources with NIR counterpart, we have made a NIR color-color diagram (Fig. 20). Also, we investigate correlation between the X-ray fluxes and the NIR magnitudes (Fig. 21), and correlation between the X-ray spectral hardness and the X-ray to NIR flux ratios (Fig. 22). From Fig. 20 to 22, we notice the following X-ray and NIR characteristics of these sources:

1. On the NIR color-color diagram, soft X-ray sources are mostly on the main-sequence track (Fig. 20), while medium and hard sources are more scattered.
2. Soft X-ray and NIR fluxes are correlated (Fig. 21 top), and the correlation is along the slope expected for the constant luminosity sources at different distances. On the other hand, such a correlation is not clearly seen between the hard X-ray and NIR fluxes (Fig. 21 bottom).
3. The X-ray spectral hardness and the *hard* X-ray to NIR flux ratio shows a correlation

(Fig. 22 bottom), while such a correlation is not obvious between the X-ray spectral hardness and the *soft* X-ray to NIR flux ratio (Fig. 22 top).

The fact (1), together with the thin thermal X-ray spectra (Fig. 13), confirms stellar origin of the soft X-ray sources. The above fact (2) suggests that the observed soft X-ray and NIR flux distributions are both explained primarily due to various source distances.

The above fact (3) suggests that cataclysmic variables, hard X-ray sources, can emit hard X-rays more efficiently than X-ray active stars at a given NIR flux. Also, the wide distribution of the hard X-ray sources on the NIR color-color diagram (Fig. 20) looks similar to that of the known cataclysmic variables (Hoard et al. 2002; Cutri et al. 2005).

What about origin of the sources without NIR counterpart? Let's first consider the soft X-ray sources. Background AGNs are unlikely, since they are almost completely absorbed in the soft X-ray band (Fig. 9 bottom). It is suggested that isolated neutron stars may be dim soft X-ray sources without optical/NIR counterparts (e.g., Popov et al. 2000). However, there is hardly an isolated neutron star among our 38 soft X-ray sources without NIR counterparts, since expected surface number density of such isolated neutron star is one per square degree (Popov et al. 2000), namely, ~ 0.07 in our *Chandra* field. Consequently it will be more natural to assume that those soft X-ray sources without NIR counterpart are X-ray active stars whose NIR fluxes are below our sensitivity, because of the intrinsic low NIR luminosities and/or large distances.

Regarding the hard X-ray sources without NIR counterpart (55 among the total 69 hard sources), most of them are considered to be background AGNs. In fact, the Galactic flux attenuation is minor (Fig. 9 top), thus we *must* be observing almost all the background AGNs on the Galactic plane. In fact, our $2 - 10$ keV $\log N - \log S$ curve is successfully modeled by assuming that all the hard X-ray sources without NIR counterpart are extragalactic, and those with NIR counterpart are Galactic (Section 4.2).

4.2. Modeling the 2– 10 keV $\log N - \log S$ Curve on the Galactic Plane

We are going to model the observed $2 - 10$ keV $\log N - \log S$ curves on the Galactic plane by *Chandra*, *XMM-Newton* and *ASCA*, following earlier attempts by, e.g., Grimm, Gilfanov & Sunyaev (2002) and Hands et al. (2004). We assume three populations, high L_x population (neutron star binaries), low L_x population (white dwarf binaries) and extragalactic sources. We adopt the same Galactic disk model by Hands et al. (2004), namely, the Galactic source

population depends on the Galactic radius R and height z as,

$$N[\text{pc}^{-3}] = N_0[\text{pc}^{-3}] \exp(-R/R_G) \exp(-z/200 \text{ pc}), \quad (1)$$

where R_G is the Galactocentric radius 8.5 kpc, and N_0 is determined from the differential luminosity function, as

$$N_0 = \int_{L_{min}}^{L_{max}} AL^{-\alpha} dL. \quad (2)$$

The maximum diameter of the Galactic disk is assumed 20 kpc, and the hydrogen density of 0.55 cm^{-3} (Hands et al. 2004). We integrate the sources in the line of sight ($l = 28.^\circ 5$) until the edge of the Galactic plane (distance will be 27 kpc). Note that in the small *Chandra* field of view ($\sim 17'$), the vertical distance from the Galactic plane is $\sim 130 \text{ pc}$ even at the edge of the Galaxy, smaller than the 200 pc Galactic scale height. Therefore, if we assume the constant luminosity sources, the $\log N - \log S$ curve is expected to have the slope -1.5 only determined by observing volume increase. For the extragalactic sources attenuated by Galactic extinction ($\sim 6 \times 10^{23} \text{ cm}^{-2}$), we assumed the following functional shape (Ueda et al. 1999; Giacconi et al. 2001):

$$N(> S) = \begin{cases} 25 (S/4.9 \times 10^{-14})^{-1.5} & \text{for } S \geq 2.6 \times 10^{-14} \text{ erg cm}^{-2} \text{ s}^{-1} \\ 1200 (S/1.4 \times 10^{-15})^{-1.0} & \text{for } S < 2.6 \times 10^{-14} \text{ erg cm}^{-2} \text{ s}^{-1}. \end{cases} \quad (3)$$

Now we are free to choose four parameters in equation (2) for high L_x population and low L_x population each. For the high L_x population, we took $A = 3$, $\alpha = 1.3$, $L_{min} = 10^{32.5} \text{ erg s}^{-1}$ and $L_{max} = 10^{36.5} \text{ erg s}^{-1}$ (Fig. 23). These values are similar to those used by Grimm, Gilfanov & Sunyaev (2002) and Hands et al. (2004). Integrating the luminosity function over the Galactic plane, there will be ~ 200 such neutron star binaries, which is reasonable (Fig. 23). In any case, our *Chandra* observation is not sensitive to the choice of high L_x population parameters, since they affect only bright sources above $\sim 10^{-12} \text{ erg s}^{-1} \text{ cm}^{-2}$.

On the other hand, *Chandra* $\log N - \log S$ curve below $2 \times 10^{-13} \text{ erg s}^{-1} \text{ cm}^{-2}$ is significantly dependent on the low L_x population. In particular, we are sensitive to L_{max} and the normalization there. We found the choice of $A = 300$, $\alpha = 1.3$ and $L_{max} = 2 \times 10^{33} \text{ erg s}^{-1}$ (Fig. 23) can explain the observed *Chandra*, *XMM-Newton* and *ASCA* $\log N - \log S$ curves reasonably well (Fig. 24). In particular, the low L_x population model curve can approximate the *Chandra* $\log N - \log S$ curve of the hard X-ray sources with NIR counterpart (line in cyan in Fig. 9 and 24), which is reasonable since these sources are considered to be Galactic (see also Section 4.1). We tried three very different $L_{min} = 10^{28}$, 10^{28} and $10^{30} \text{ erg s}^{-1}$ (Fig. 23), but resultant differences in $\log N - \log S$ are hardly noticeable (Fig. 24). If integrated over the Galactic plane, we need at least 10^4 such dim X-ray sources below $2 \times 10^{33} \text{ erg s}^{-1}$

(Fig. 23). There may be orders of magnitude more such dim Galactic sources depending on L_{min} , but we may not constrain from the *Chandra* $\log N - \log S$ analysis above $\sim 3 \times 10^{-15}$ erg s $^{-1}$ cm $^{-2}$.

In summary, from *Chandra* and *XMM-Newton* $\log N - \log S$ analysis, it is no doubt that there is a low L_x population of Galactic sources below $\sim 2 \times 10^{33}$ erg s $^{-1}$ and greater than 10^4 in number, in addition to the well-established bright neutron star population. From our X-ray and NIR study, these dim Galactic sources are most likely to be cataclysmic variables (Section 4.1). Presence of such dim and numerous cataclysmic variables had been in fact expected (e.g., Mukai & Shiokawa 1993; Verbant et al. 1997; Watson 1999), but with *Chandra* and *XMM-Newton* we are for the first time able to measure their population and X-ray characteristics accurately.

4.3. Absolute GRXE Flux and Comparison with Other Measurements

Excluding the point sources in our field of view brighter than $\sim 3 \times 10^{-15}$ erg s $^{-1}$ cm $^{-2}$ (2 – 10 keV) or $\sim 2 \times 10^{-16}$ erg s $^{-1}$ cm $^{-2}$ (0.5 – 2 keV), we have extracted and studied the Galactic diffuse emission spectra. Using the best-fit spectral model (Section 3.6), we determine the observed diffuse emission flux as 6.5×10^{-11} erg s $^{-1}$ cm $^{-2}$ deg $^{-2}$ (2 – 10 keV) and 8.7×10^{-12} erg s $^{-1}$ cm $^{-2}$ deg $^{-2}$ (0.5 – 2 keV). The soft X-ray flux we measured might be affected by uncertainty of the background subtraction (Section 3.1). On the other hand, our measurement in the hard X-ray band is considered to be most precise to date with accurate background subtraction, well-determined mirror response and, most of all, hardly contamination from point sources.

Let's compare our measurement in the 2 – 10 keV band with those by *ASCA* or *XMM-Newton*. In Table 9, we show the 2 – 10 keV GRXE fluxes measured by *ASCA* (Kaneda et al. 1997; Sugizaki et al. 2001), *XMM-Newton* (Hands et al. 2004) and *Chandra* (present paper). We should be careful that point source sensitivities in these measurements are very different, and the GRXE fluxes thus obtained necessarily contain contributions from both diffuse emission and point sources below the thresholds. If all the resolved point sources are included, our *Chandra* observation gives the GRXE flux 7.4×10^{-11} erg s $^{-1}$ cm $^{-2}$ deg $^{-2}$ in 2 – 10 keV, where the brightest point source (Source 200 in Table 1) has the flux $\sim 2 \times 10^{-13}$ erg s $^{-1}$ cm $^{-2}$. In the *XMM-Newton* survey (Hands et al. 2004) where point sources between 2×10^{-14} to 2×10^{-12} erg s $^{-1}$ cm $^{-2}$ deg $^{-2}$ are detected, if we exclude the point sources above $\sim 2 \times 10^{-13}$ erg s $^{-1}$ cm $^{-2}$ (brightest *Chandra* source flux), the GRXE flux is 9.3×10^{-11} erg s $^{-1}$ cm $^{-2}$ deg $^{-2}$. The *XMM-Newton* GRXE flux is $\sim 25\%$ higher than our *Chandra* flux, but considering the lower Galactic longitudes of the *XMM-Newton* survey, which should result

in higher GRXE fluxes, we consider the *Chandra* and *XMM-Newton* flux agreement pretty well.

On the other hand, the two independent *ASCA* surveys (Kaneda et al. 1997; Sugizaki et al. 2001) report much smaller GRXE fluxes than *Chandra* and *XMM-Newton* (Table 9). We suspect this might be due to systematic effects of the *ASCA* X-ray telescope; when largely extended sources are observed with *ASCA*, stray-lights from outside of the field of view (~ 25 arcmin radius) are significant. This effect is taken into account in both Kaneda et al. (1997) and Sugizaki et al. (2001) to calculate the GRXE flux, such that the diffuse flux *per sky area* is derived *assuming* the diffuse emission is uniformly distributed over the $1.^\circ5$ radius. In reality, the GRXE scale height may not be as large as $1.^\circ5$, in that case *ASCA* measurements *underestimate* the GRXE surface flux per sky area.

4.4. Ultimate Point Source Contribution to GRXE

Let’s consider if the Galactic “diffuse” emission we obtained by removing resolved *Chandra* point sources may be accounted for by superposition of still dimmer point sources below our detection limits. The total energy flux observed in our *Chandra* field, F_{total} , may be expressed as follows:

$$F_{total}[\text{erg s}^{-1} \text{ cm}^{-2} \text{ deg}^{-2}] = F_{S \leq S_{th}} + \int_{S' > S_{th}}^{S_{max}} S' \frac{dN(> S')}{dS'} dS', \quad (4)$$

where the first term in the right hand side includes the diffuse emission and the contribution of the point sources equal to or dimmer than the threshold flux S_{th} . The second term is the contribution from the point sources brighter than S_{th} . We may define the hypothetical point source number density,

$$N(S_{th}) \equiv F_{S \leq S_{th}} / S_{th}, \quad (5)$$

whose meaning is as follows: if point source detection above flux S_{th} is complete, in addition to the sources brighter than S_{th} , the hypothetical $N(S_{th})$ sources having the same flux S_{th} would account for the total X-ray flux observed in the field of view. In the present case, we have set the threshold flux $\sim 3 \times 10^{-15} \text{ erg s}^{-1} \text{ cm}^{-2}$ (2 – 10 keV) and $\sim 2 \times 10^{-16} \text{ erg s}^{-1} \text{ cm}^{-2}$ (0.5 – 2 keV), then the first term in equation (4) is the “diffuse” flux we determined earlier. The second term in Eq. 4 can be obtained by integrating the detected point source fluxes above S_{th} ; for the same threshold fluxes, they are $\sim 8.5 \times 10^{-12} \text{ erg s}^{-1} \text{ cm}^{-2} \text{ deg}^{-2}$ (2 – 10 keV) and $\sim 1.0 \times 10^{-12} \text{ erg s}^{-1} \text{ cm}^{-2} \text{ deg}^{-2}$ (0.5 – 2 keV), respectively. Therefore, the total observed flux in the field view is $\sim 7.4 \times 10^{-11} \text{ erg s}^{-1} \text{ cm}^{-2} \text{ deg}^{-2}$ (2 – 10 keV) and $\sim 9.7 \times 10^{-12} \text{ erg s}^{-1} \text{ cm}^{-2} \text{ deg}^{-2}$ (0.5 – 2 keV), respectively.

In Fig. 9 and 24, we show $N(S_{th})$ defined in Eq. 5 for different values of S_{th} . In order to account for the total X-ray fluxes in the field of view with 100 % of point sources, it is required that the $\log N - \log S$ curves rapidly steepen by an order of magnitude somewhere below our sensitivity limits, which is extremely unlikely. In particular, even if we significantly extrapolate the low L_x luminosity function to the dimmer side (Fig. 23), increase of $\log N - \log S$ curve is very tiny (Fig. 24).

Furthermore, we examine if introducing another unknown, still dimmer Galactic source population might explain the 100 % of the GRXE flux in 2 – 10 keV. Now we consider luminosity functions as shown in Fig. 25. There is a hypothetical source population below $10^{30} \text{ erg s}^{-1}$, and the total number of such sources in the Galaxy is $\gtrsim 10^9$, in addition to neutron star (high L_x) and white dwarf (low L_x) populations. Although combination of these populations can more or less explain the observed *Chandra* $\log N - \log S$ curve above $3 \times 10^{-15} \text{ erg s}^{-1} \text{ cm}^{-2}$ (Fig. 26), it is not sufficient at all to explain the 100 % of GRXE. The point is that any $\log N - \log S$ curves of Galactic source populations, whatever the luminosity function is, cannot have a slope steeper than -1.5 . Hence, no Galactic source population can explain both the observed *Chandra* $\log N - \log S$ curve and the 100 % of the GRXE flux simultaneously. Consequently, we conclude GRXE is primarily diffuse emission.

4.5. Origin of the Galactic Diffuse X-ray Emission

We found that GRXE has a truly diffuse origin, then the question is how to produce and maintain such high energetic plasma. There are obvious problems in interpreting GRXE in terms of simple equilibrium thermal plasma, such that the plasma temperature needed to explain the observed spectra, $kT \approx 5 - 10 \text{ keV}$, is much higher than can be bound by Galactic gravity (Warwick et al. 1985). Also, the energy density of GRXE, $\sim 10 \text{ eV/cm}^3$, is one or two orders of magnitude higher than those of other constituents in the interstellar space, such as cosmic rays, Galactic magnetic fields, or ordinary interstellar medium (Koyama et al. 1986; Kaneda et al. 1997). Currently there are no accepted theoretical models that can explain the origin of GRXE. Some argue that the interstellar magnetic field is playing a significant role to heat and confine the hot plasma (Tanuma et al. 1999). Others propose that the interstellar medium is mainly responsible for GRXE and gamma-ray emission, via interactions with, for instance, low energy cosmic-ray electrons (Valinia et al. 2000b), in situ accelerated quasi-thermal electrons (Dogiel et al. 2002; Masai et al. 2002), or heavy ions (Tanaka, Miyaji, & Hasinger 1999). Galactic particle acceleration is considered to be taking place in supernova remnants. In fact, serendipitous discovery of the hard X-ray emitting supernova remnant AXJ 1843.8–0352 in our field (Bamba et al. 2001; Ueno et al. 2003)

strongly suggests a close tie between GRXE and supernova remnants.

Various theoretical models of GRXE have to be tested through observations. Different heating or acceleration mechanism of the plasma will result in different plasma conditions, which are reflected in the emission lines. Therefore, from precise measurements of the GRXE emission lines, we may in principle diagnose the plasma conditions and constrain the theoretical models. In particular, iron line spectroscopy is essential. We have shown that the GRXE iron line central energy is $6.52 \pm_{0.14}^{0.08}$ keV (Section 3.6), significantly lower than what expected from thermally equilibrium plasma (~ 6.67 keV). Although from our data we could not distinguish if this iron line is really a single line or composite of two or three lines, the *Chandra* Galactic center diffuse spectrum clearly indicates the three emission lines from low ionized iron, He-like iron and H-like iron (Muno et al. 2004). If we assume similar origins of Galactic center and plane diffuse emission (see Section 4.6), then the three line interpretation of GRXE iron line emission seems plausible (see also Tanaka 2002). If this is the case, the 6.4 keV line is considered from fluorescence in cool interstellar medium, which may be induced, for instance, by low energy cosmic-ray electrons (Valinia et al. 2000b). The He-like and H-like lines may be from hot thermal equilibrium plasma (Valinia et al. 2000b), charge exchange process of iron ions (Tanaka, Miyaji, & Hasinger 1999; Tanaka 2002), or recombination cascades of quasi-thermal electrons (Masai et al. 2002). In the second case, the lines are expected to be significantly broadened by the iron nucleus bulk motion (Tanaka et al. 2000). In the last case, the emission lines are accompanied by recombination continuum above He-like and H-like iron K-edges (Masai et al. 2002). These three cases may be distinguished from precise spectral observation in the iron line/edge energy range.

We emphasize that the precise iron line diagnostic (including line intrinsic width measurement) is a key to resolve origin of the Galactic center and Galactic plane diffuse emission. In this context, planned Galactic center observations with *Astro-E2* XRS, the first X-ray microcalorimeter in space with ~ 6 eV resolution, will be an enormous help. GRXE may be too dim for *Astro-E2* XRS (our simulation suggests that a million second exposure is required), but we believe that the long standing mystery of GRXE will be certainly solved by future calorimeter observations with much higher throughputs and better spectral resolution, expected to be made by *Con-X*, *NEXT* and/or *XEUS*.

4.6. Comparison with the Galactic Center

It will be interesting to compare our point source populations in the Galactic plane ($l \approx 28.^\circ 5$) with those at Sgr A ($l \approx 0^\circ$) and Sgr B2 ($l \approx 0^\circ.5$). We have analyzed the *Chandra* Galactic center Sgr B2 region data (observed in 2000 March 29 for 100 ksec, obsID=944;

Murakami, Koyama and Maeda 2001) in a similar manner to our Galactic plane data analysis, and made $\log N - \log S$ curves for both energy bands in Fig. 9. The $\log N - \log S$ curves in the Sgr A region are also plotted (from Munro et al. 2003). In the hard energy band, the source number density increases dramatically toward the Galactic center, significantly exceeding that on the Galactic plane and extragalactic one. This indicates that there are much more Galactic hard point sources in the Galactic center region than in the Galactic plane. In the soft band, on the other hand, the source number density at the lowest flux level is not so different on the Galactic plane and at the Galactic center regions. This is probably because the faintest observable soft sources are mostly located in our neighborhood, so that the direction toward the Galactic center or Galactic plane will not make a big difference. In fact, such dim soft sources at the Galactic center will be more significantly absorbed ($N_H \approx 10^{23} \text{ cm}^{-2}$) than those extragalactic sources in our Galactic plane field ($N_H \approx 6 \times 10^{22} \text{ cm}^{-2}$), and thus hardly detected.

We also compare diffuse emission from the Galactic plane and Galactic center. Considering the diffuse spectral similarity on the Galactic plane (Section 3.6) and Galactic center (Munro et al. 2004), we are tempted to conclude that they have similar origins (see also Tanaka 2002). Recent INTEGRAL observations have detected hard X-ray emission above 20 keV in the Galactic center region whose centroid is slightly offset of Sgr A* (Bélanger et al. 2004). This suggests that a non-thermal hard-tail of the Galactic center diffuse spectrum is extended above 20 keV. GRXE also has a power-law hard-tail component which extends above ~ 20 keV (Yamasaki et al. 1997; Valinia and Marshall 1998). On the other hand, strong diffuse gamma-ray ($\sim 100 \text{ keV} - 1 \text{ MeV}$) emission is observed from the Galactic center and plane region (e.g., Gehrels and Tueller 1993; Skibo et al. 1997; Valinia et al. 2000a; Strong et al. 2003), which is suggested to have a non-thermal origin. Intriguingly, the Galactic center and plane diffuse hard X-ray components seem to be smoothly connected to the gamma-ray components. We suspect there is a common physical mechanism in the Galactic center and plane diffuse emission to produce hard X-ray and gamma-ray emission from several keV to $\sim \text{MeV}$.

5. Conclusion

Using *Chandra* ACIS-I, we have carried out a deep X-ray observation ($0.5 - 10 \text{ keV}$) on a typical Galactic region at $(l, b) \approx (28.^\circ 5, 0.^\circ 0)$ within $\sim 250 \text{ arcmin}^2$ to study characteristics of Galactic Ridge X-ray Emission (GRXE), followed by a NIR identification observation with NTT/SOFI at ESO. Our main results are summarized below:

1. We have detected 274 new X-ray sources (4σ confidence) down to $\sim 3 \times 10^{-15} \text{ erg s}^{-1}$

cm^{-2} in $2 - 10$ keV or $\sim 2 \times 10^{-16} \text{ erg s}^{-1} \text{ cm}^{-2}$ in $0.5 - 2$ keV. Only 26 sources are detected both in the soft and hard bands. In the SOFI field, 83 % of the soft sources are identified in NIR, while only 22 % of the hard sources have NIR counterparts. Most of the soft X-ray sources are considered to be X-ray active stars, while most of the unidentified hard X-ray sources are extragalactic.

2. Only ~ 10 % of the observed X-ray flux in the *Chandra* field is accounted for by the sum of point source fluxes. Even if we assume an unknown population of much dimmer and numerous Galactic sources, the observed GRXE flux is not explained. Therefore, we conclude that GRXE has truly diffuse origin, confirming our early report using half of the current *Chandra* data (Ebisawa et al. 2001) and in agreement with the *XMM-Newton* Galactic survey with a larger sky coverage (Hands et al. 2004).
3. Soft X-ray sources exhibit thin thermal spectra, characteristics of active stars. In fact, they follow the track of main-sequence stars on the NIR color-color diagram. Small number of the hard X-ray sources with NIR counterpart exhibit a narrow iron emission line at 6.67 keV as a signature of the Galactic cataclysmic variables. To explain the observed $2 - 10$ keV $\log N - \log S$ curve, we suppose there are at least 10^4 cataclysmic variables in the Galactic plane dimmer than $\sim 2 \times 10^{33} \text{ erg s}^{-1}$.
4. Removing contamination of point X-ray sources brighter than $3 \times 10^{-15} \text{ erg s}^{-1} \text{ cm}^{-2}$ ($2 - 10$ keV), we have precisely measured the Galactic diffuse X-ray emission flux as $6.5 \times 10^{-11} \text{ erg cm}^{-2} \text{ s}^{-1} \text{ deg}^{-2}$ in $2 - 10$ keV. The energy spectrum of the diffuse emission can be modeled with a two temperature non-equilibrium ionization model, such that the soft, less absorbed component is more highly ionized than the hard, more absorbed component.
5. We have measured the diffuse iron emission line energy as $6.52 \pm_{0.14}^{0.08} \text{ keV}$ (90 % error). This is significantly lower than what is expected from thermally equilibrium plasma (6.67 keV). This shift of the iron line energy may be explained either by non-equilibrium ionization of the plasma, or hybrid of the 6.4 keV fluorescent line and the 6.67 keV line from equilibrium plasma.

We are grateful to R. Mushotzky, Y. Yang and K. D. Kuntz for useful comments on the *Chandra* data analysis and discussion. We thank the second referee for his/her insight of the ACIS intrinsic background spectral feature. Support for this work was provided by the National Aeronautics and Space Administration (NASA) through *Chandra* Guest Observer program (Sequence number 900021 and 900125) issued by the Chandra X-ray Observatory Center, which is operated by the Smithsonian Astrophysical Observatory for and on behalf of

NASA under contract NAS8-03060. This publication is based on observations collected at the European Southern Observatory, Chile (ESO N° 69.D-0664). Also, this paper makes use of data products from the Two Micron All Sky Survey, which is a joint project of the University of Massachusetts and the Infrared Processing and Analysis Center/California Institute of Technology, funded by NASA and the National Science Foundation. An image used in this paper was produced with Montage, an image mosaic service supported by the NASA Earth Sciences Technology Office Computing Technologies program, under Cooperative Agreement Notice NCC 5-6261 between NASA and the California Institute of Technology. M.T. is financially supported by the Japan Society for the Promotion of Science.

REFERENCES

- Bamba, A., Ueno, M., Koyama, K. , & Yamauchi, S. 2001, PASJ, 63, L21
- Bélanger, G. et al. 2004, ApJ, 601, L163
- Bertin, E. & Arnouts, S. 1996, A&AS, 117, 393
- Cox, A. N. 1999, “Allen’s Astrophysical Quantities”, fourth edition, Springer
- Cutri, R. et al. 2005, in preparation
- Dame, T. M., Hartmann, D. & Thaddeus, P. 2001, ApJ, 547, 792
- Dickey, J. M. & Lockman, F. J. 1990, ARAA, 28, 215
- Dogiel, V.A., Inoue, H., Masai, K., Schönfelder, V. & Strong, A. W. 2002, ApJ, 581, 1061
- Ebisawa, K., Maeda, K., Kaneda, H. & Yamauchi, S. 2001, Science, 293, 1633
- Ebisawa, K., Yamauchi, S., Bamba, A., Ueno, M. & Senda, A. 2003, Astron. Nachr. 324, 52
- Ezuka, H. & Ishida, M. 1999, ApJS, 120, 277
- Forman, W., Jones, C., Cominsky, L., Julien, P., Murray, S., Peters, G., Tananbaum, H. & Giacconi, R. 1978, ApJS, 38 357
- Garmire, G. et al. 2003, SPIE, 4851, 28
- Gehrels, N. & Tueller, J. 1993, ApJ, 407, 597
- Giacconi, R. et al. 2001, ApJ, 551, 624

- Grimm, H.-J., Gilfanov, M. & Sunyaev, R. 2002, *A&A*, 391, 923
- Hands, A. D. P., Warwick, R. S., Watson, M. G. & Helfand, D. J. 2004, *MNRAS*, 351, 31
- Harjunpaae, P. & Mattila, K. 1996, *A&A*, 305, 920
- Hertz, P. & Grindlay, J. E. 1984, *ApJ*, 278, 137
- Hoard, D. W., Wachter, S. Clark, L. L. & Bowers, T. P. 2002, *ApJ*, 565, 511
- Kaneda, H., Makishima, K., Yamauchi, S., Koyama, K., Matsuzaki, K. & Yamasaki, N. Y. 1997, *ApJ*, 491, 638
- Koyama, K., Makishima, K., Tanaka, Y. , & Tsunemi, H. 1986, *PASJ*, 38, 121
- Masai, K. 1984, *Ap&SS*, 98, 367
- Masai, K., Dogiel, V.A., Inoue, H., Schönfelder, V. & Strong, A. W. 2002, *ApJ*, 581, 1071
- Minter, A.H., Lockman, F. J., Langston, G. I. & Lockman, J. A. 2001, *ApJ*, 555, 868
- Motch, C., Belloni, T., Buckley, D. et al. 1991, *A&A*, 246, L24
- Mukai, K. & Shiokawa, K. 1993, *ApJ*, 418, 863
- Muno, M. P. et al. 2003, *ApJ*, 589, 225
- Muno, M. P. et al. 2004, *ApJ*, 613, 326
- Murakami, H., Koyama, K. , & Maeda, Y. 2001, *ApJ*, 558, 687
- Popov, S. B., Colpi, M. Prokhorov, M. E., Treves, A. & Turolla, R. 2000, *ApJ*, 544, L53
- Predehl, P. & Schmitt, J. 1995, *A&A*, 293, 889
- Sakano, M., Koyama, K., Murakami, H., Maeda, Y. & Yamauchi, S. 2002, *ApJS*, 138, 19
- Skibo, J. G. et al. 1997, *ApJ*, 483, L95
- Strong, A. W., Bouchet, L., Diehl, R., Mandrou, P., Schönfelder, V. & Teegarden, B. J. 2003, *A&A*, 411, L447
- Sugizaki, M., Mitsuda, K., Kaneda, H., Matsuzaki, K., Yamauchi, S. & Koyama, K. 2001, *ApJS*, 134, 77
- Tanaka, Y., Inoue, H. & Holt, S. S. 1994, *PASJ*, 46, L37

- Tanaka, Y., Miyaji, T. & Hasinger G. 1999, *Astron. Nachr.*, 320, 181
- Tanaka, Y. 2002, *A&A*, 382, 1052
- Tanaka, Y., Koyama, K., Maeda, Y. & Sonobe, T. 2000, *PASJ*, 52, L25
- Tanuma, S., Yokoyama, T., Kudoh, T., Matsumoto, R., Shibata, K. & Makishima, K. 1999, *PASJ*, 51, 161
- Tarenghi, M. & Wilson, R. N.; 1989, *SPIE*, 1114, 302
- Townsley, L. K., Broos, P. S., Chartas, G., Moskalenko, E., Nousek, J. A., & Pavlov, G. G. 2002a, *Nuc. Instru. & Meth.* 486, 716
- Townsley, L. K., Broos, P. S., Nousek, J. A. & Garmire, G. P. 2002b, *Nuc. Instru. & Meth.*, 486, 751
- Ueda, Y. et al. 1999, *ApJ*, 518, 656
- Ueno, M., Bamba, A., Koyama, K. & Ebisawa, K. 2003, *ApJ*, 588, 338
- Valinia, A. & Marshall, F. E. 1998, *ApJ*, 505, 134
- Valinia, A., Kinzer, R. L. & Marshall, F. E. 2000a, *ApJ*, 534, 277
- Valinia, A. et al. 2000b, *ApJ*, 543, 733
- Verbunt, F., Bunk, W. H., Ritter, H. & Pfeffermann, E. 1997, *A&A*, 327, 602
- Vuong, M. H., Montmerle, T., Grosso, N., Feigelson, E. D., Verstraete, L. & Ozawa, H. 2003, *A&A*, 408, 581
- Watson, M. G. 1999, in “Annapolis Workshop on Magnetic Cataclysmic Variables”, ASP conference series, vol. 157, p. 291
- Warwick, R. S., Turner, M. J. L., Watson, M. G. & Willingale, R. 1985, *Nature*, 317, 218
- Weisskopf, M. C., Brinkman, B., Canizares, C., Garmire, G., Murray, S. & Van Speybroeck, L. P. 2002, *PASP*, 114, 1
- Worrall, D. M., Marshall, F. E., Boldt, E. A. & Swank, J. H. 1982, *ApJ*, 255, 111
- Yamasaki, N. et al. 1997, *ApJ*, 481, 821
- Yamauchi, S. & Koyama, K. 1993, *ApJ*, 404, 620

Yamauchi, S., Kaneda, H. Koyama, K., Makishima, K., Matsuzaki, K., Sonobe, T. Tanaka, Y. & Yamasaki, N. 1996, PASJ, 48, L15

Yamauchi, S. et al. 2002, in the Proceedings of the IAU 8th Asian-Pacific Regional Meeting, Volume II, Edited by S. Ikeuchi, J. Hearnshaw, & T. Hanawa, the Astronomical Society of Japan, p.81

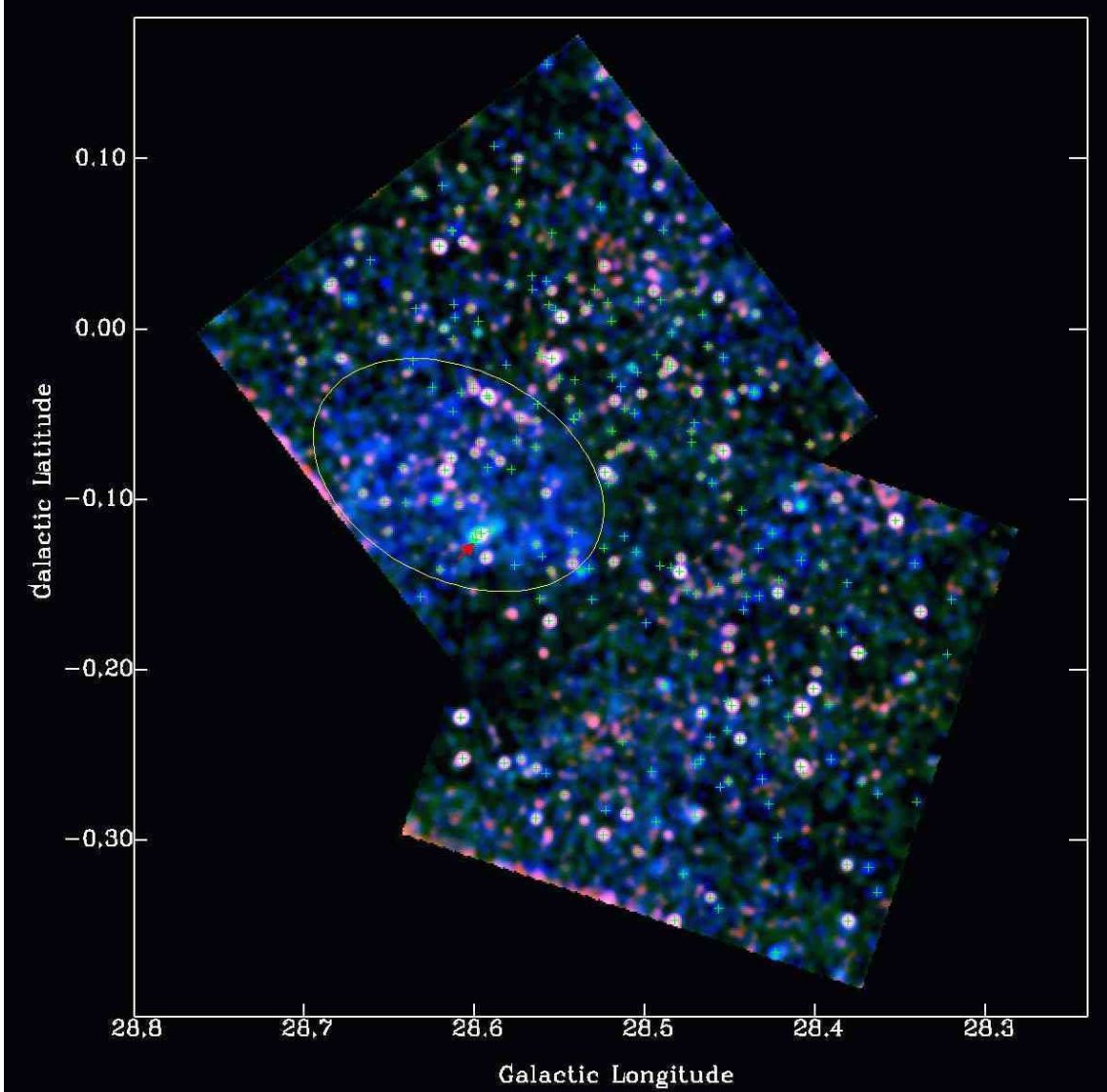


Fig. 1.— Superposed image of the two *Chandra* observations with exposure and vignetting correction (in Galactic coordinates). The upper and lower *Chandra* pointing was made in AO1 and AO2, respectively (each 100 ksec). This is a pseudo-color *Chandra* image where soft X-rays in 0.5 – 2 keV are represented in red, medium X-rays in 2 – 4 keV in green, and hard X-rays in 4 – 8 keV in blue. The image is adaptively smoothed so that both the point sources and the diffuse emission are clearly visible. The 274 detected point sources (Table 1) are marked with crosses. The region including the supernova remnant AX J 1843.8–0352/G28.6–0.1 (Bamba et al. 2001; Ueno et al. 2003) is shown with a yellow ellipse, within which the thermal blob structure CXOU J184357-035441 (Ueno et al. 2003) is marked with a red arrow. Note that the supernova remnant AX J 1843.8–0352/G28.6–0.1, which exhibits non-thermal energy spectrum (Bamba et al. 2001; Ueno et al. 2003), is more prominent in hard X-rays (“bluish” in this representation) than in soft X-rays.

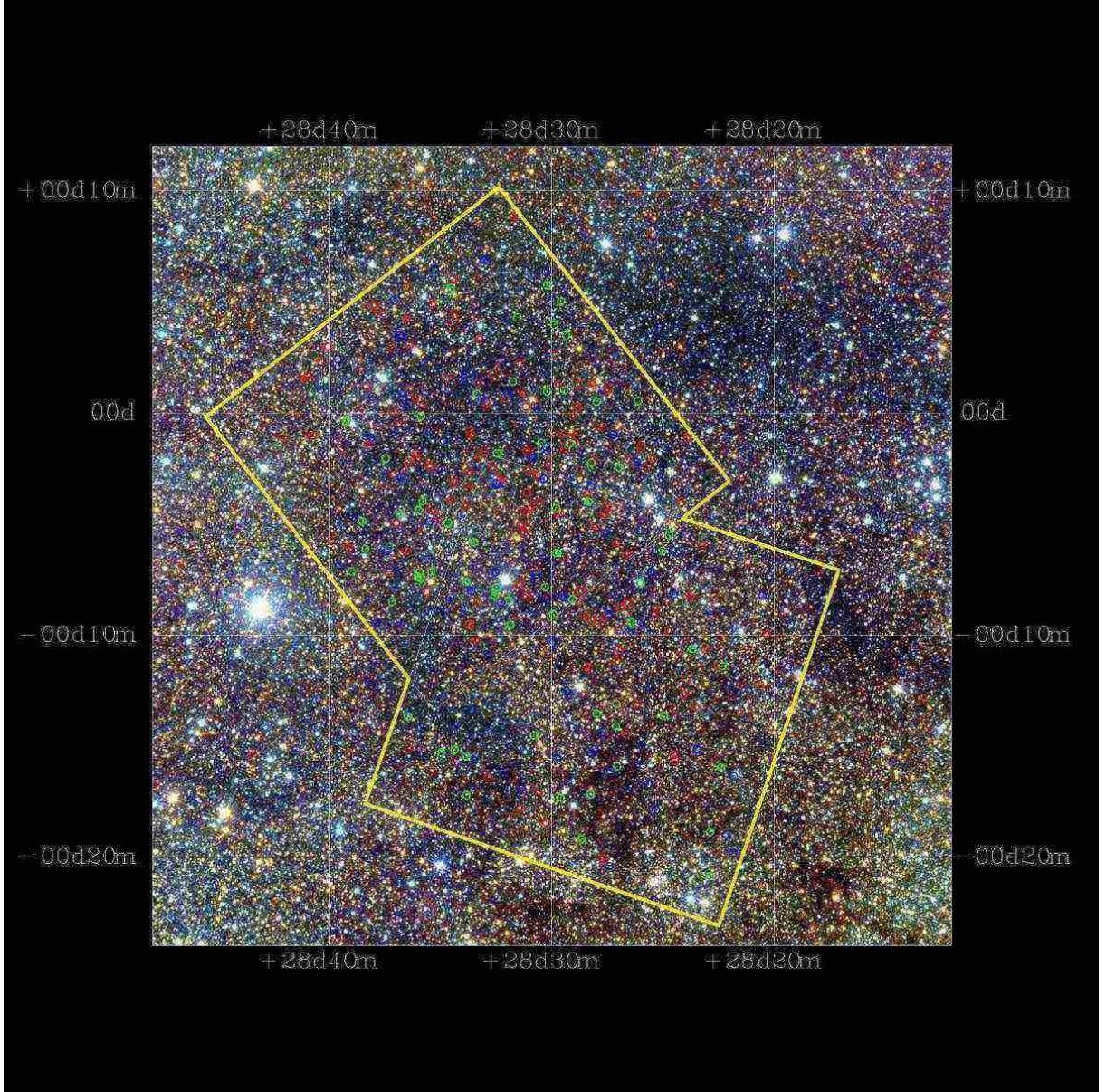


Fig. 2.— 2MASS pseudo-color image of the region including our *Chandra* field (in Galactic coordinates). The *Chandra* field of view is drawn, and the *Chandra* sources are marked in red, green or blue, for soft, medium and hard sources, respectively. For the definition of the source spectral hardness, see Section 3.2.

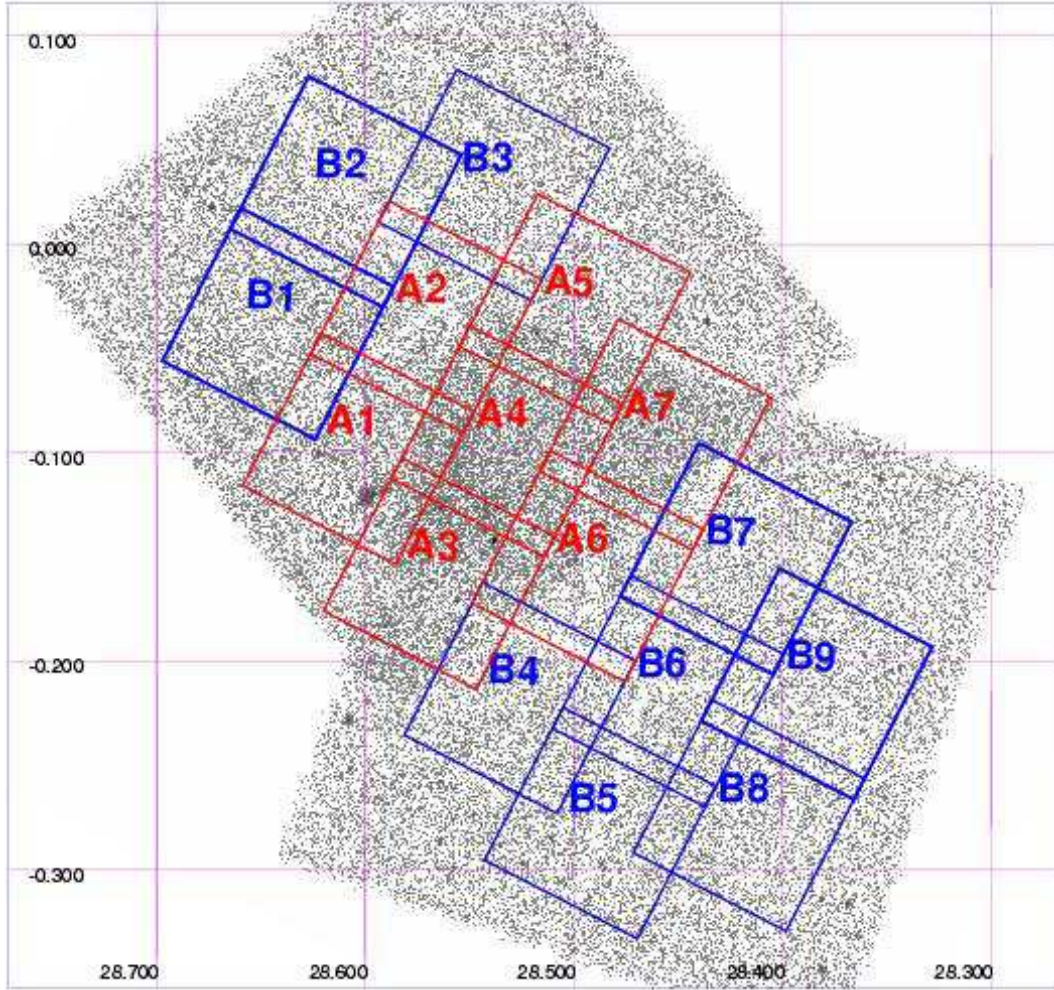


Fig. 3.— SOFI pointing positions on the *Chandra* image (without exposure correction) in Galactic coordinates. Without exposure correction, the AO1 and AO2 overlapping fields and CCD gaps are noticeable (compare with Fig. 1).

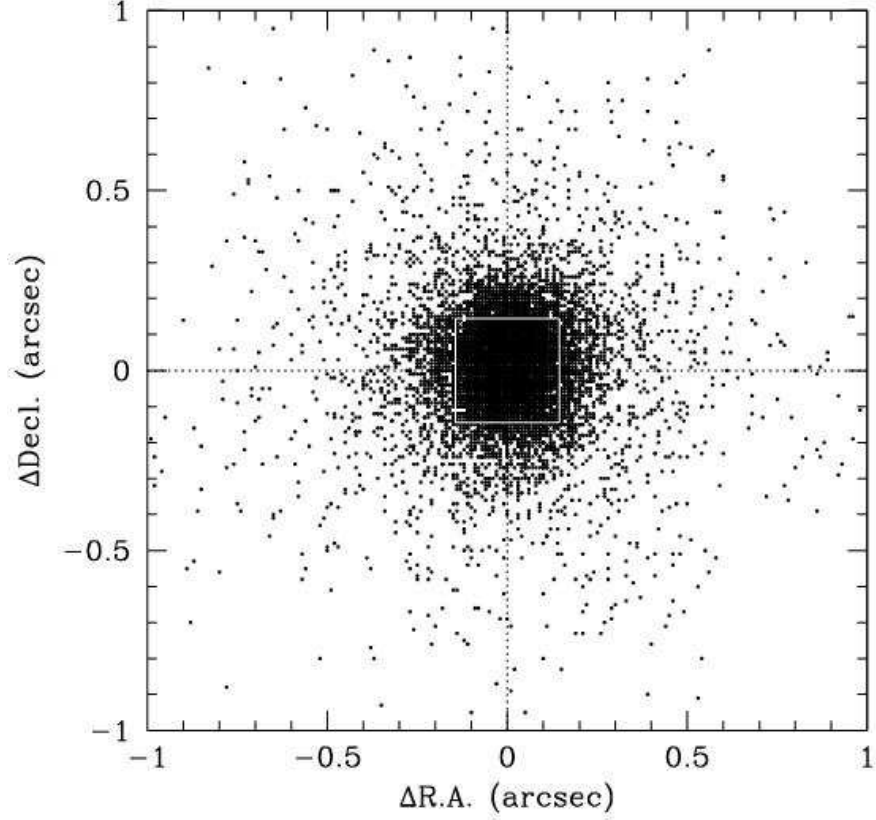


Fig. 4.— For all the 2MASS sources in the SOFI field of view, relative position of the nearest SOFI source (after astrometric correction) is plotted. The central square indicates the SOFI pixel size ($0.''2884 \times 0.''2884$). Standard deviation of the positional shift between 2MASS and SOFI is $0.''2$ in R.A. and Decl.

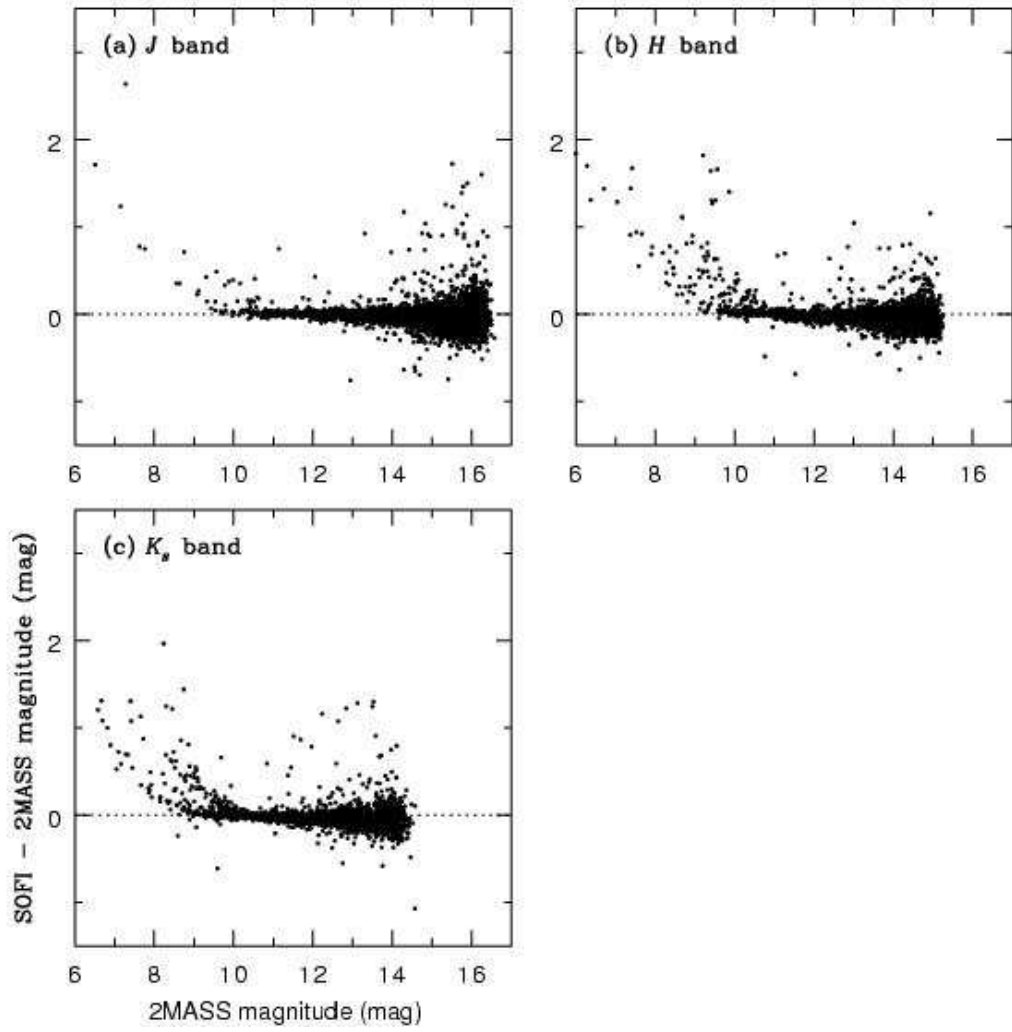


Fig. 5.— Correlation of the *J*, *H* and *K_S* magnitudes of the sources detected by both 2MASS and SOFI. Difference of the magnitudes is plotted as a function of the 2MASS magnitudes.

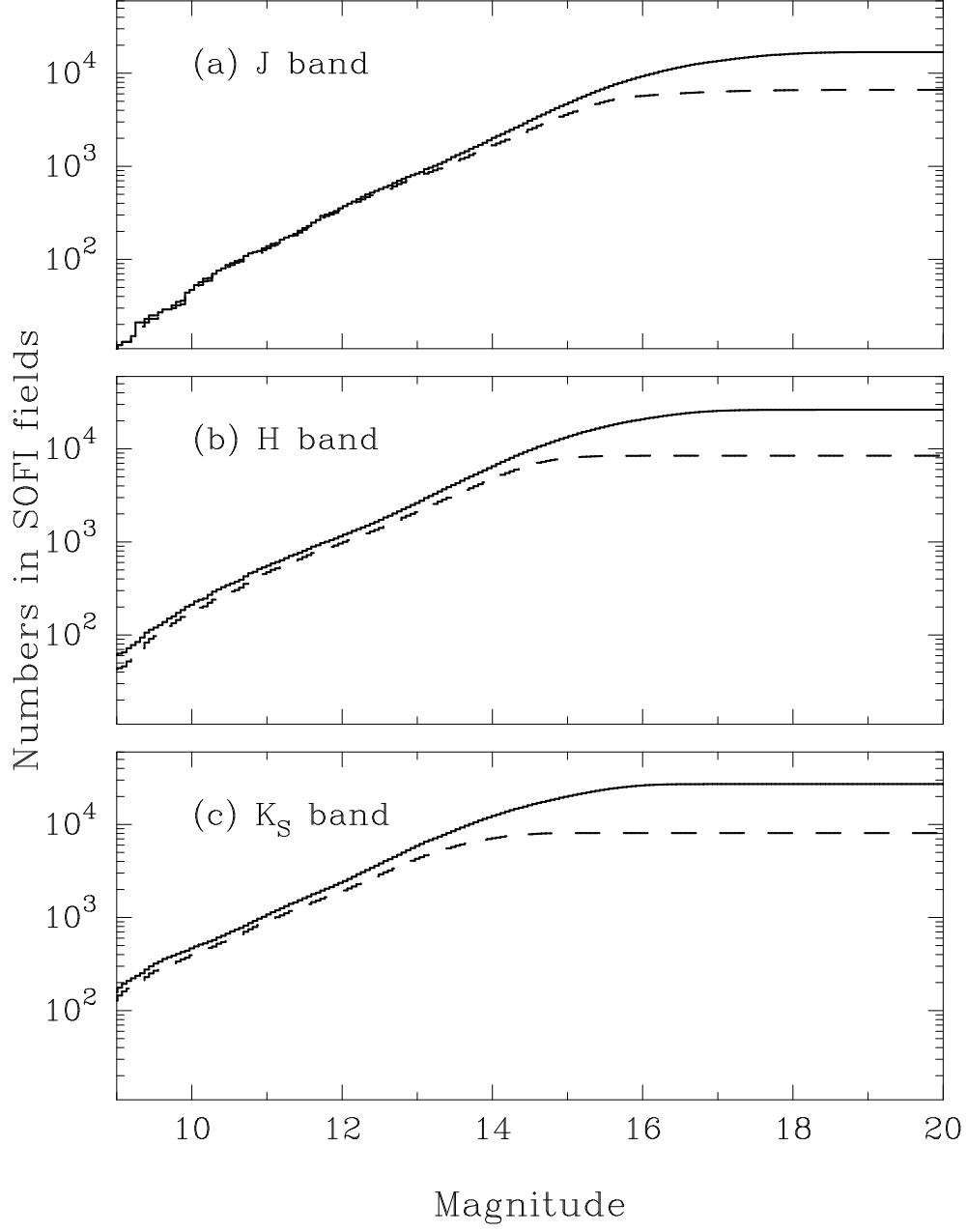


Fig. 6.— Cumulative histograms of the number of SOFI sources (*solid line*) detected in J , H and K_S bands, as a function of the SOFI magnitudes. Number of 2MASS sources in the SOFI fields are also shown with dashed line. Sources detected in two or three bands are counted in each detected band.

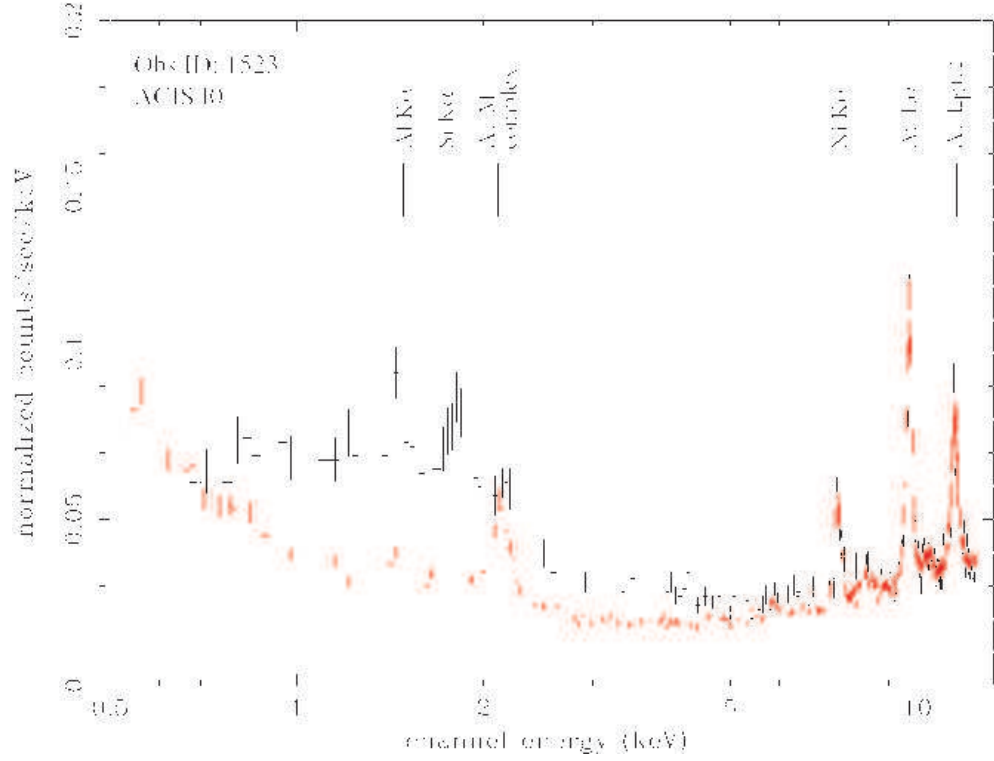


Fig. 7.— Histograms of the event count rates of ACIS I0 in our observation ID1523 (*black*) and in the CXC background database (*red*). The background is normalized in the energy range 10.5–12.5 keV. Emission lines with the instrumental origin are identified.

Chandra Galactic Plane Diffuse & Point Source Spectra

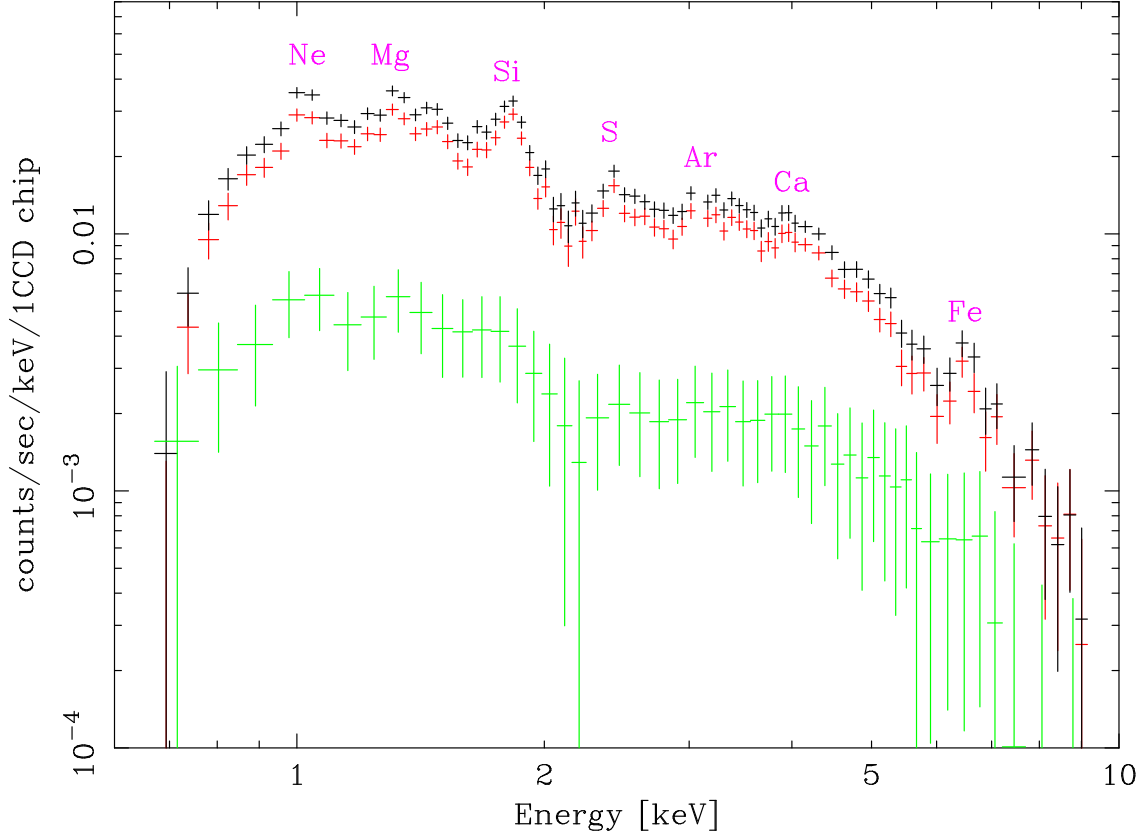


Fig. 8.— Energy spectra of the total X-rays in the field of view (black; the AX J 1843.8–0352/G28.6–0.1 region in Fig. 1 is excluded), of the sum of all the point sources (green), and of their difference, namely, the Galactic diffuse emission (red). It is found that $\sim 90\%$ of the X-ray emission is from the diffuse emission, with which emission lines from highly ionized heavy elements are associated (prominent emission lines are annotated with element names). The ordinate is normalized with the average counting rate per CCD chip.

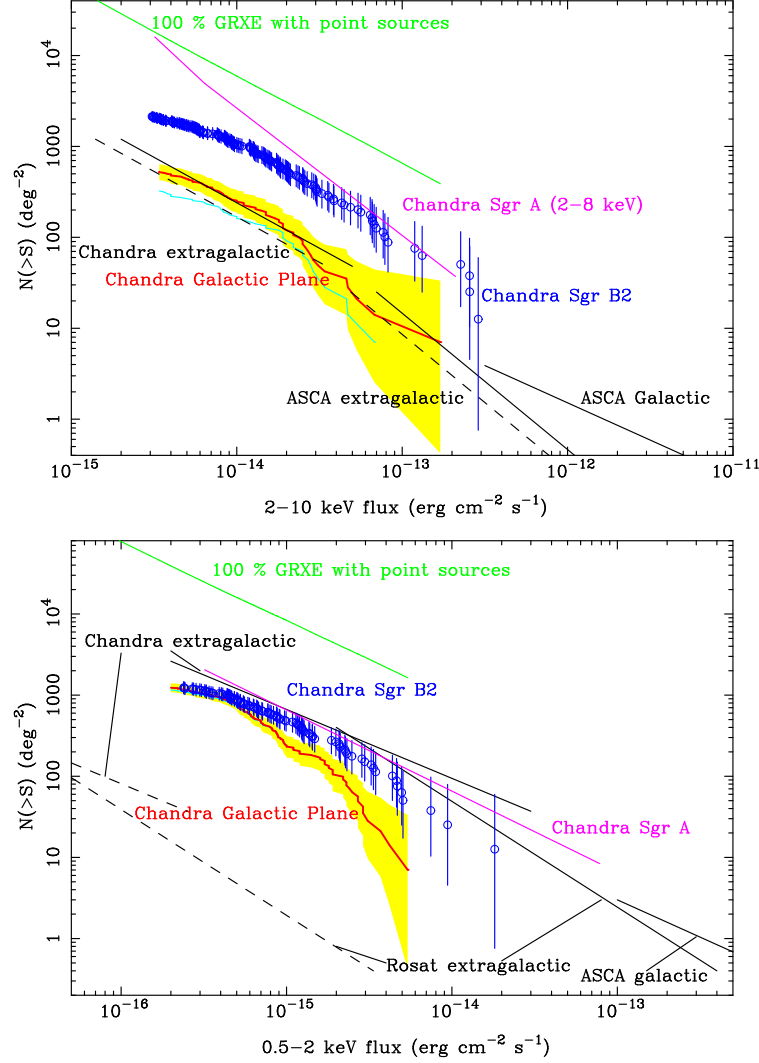


Fig. 9.— The $\log N - \log S$ curves of the point sources detected in our *Chandra* Galactic plane field in 2 – 10 keV (top) and 0.5 – 2 keV (bottom). They are indicated in red lines, and the 90 % error regions are shown in yellow. Also the $\log N - \log S$ curves of only the sources having the near infrared counterparts are shown in cyan (in the soft band, it is almost completely overlapped with red-line, and barely seen only at the lowest flux). In addition, number of the hypothetical point sources which would account for 100 % of the Galactic ridge X-ray emission at a given point source flux is indicated in green (see Section 4.4 for precise definition). Together, other $\log N - \log S$ relations are shown for the bright *ASCA* Galactic sources (Sugizaki et al. 2001), *Chandra* Galactic center Sgr B2 and Sgr A (Muno et al. 2003), and extragalactic point sources detected with *ASCA* (Ueda et al. 1999), *ROSAT* and *Chandra* (Giacconi et al. 2001). For the extragalactic sources, both the original $\log N - \log S$ curves at high Galactic latitudes (black solid lines) and the ones corrected on the Galactic plane after being extinguished by a hydrogen column density of 6×10^{22}

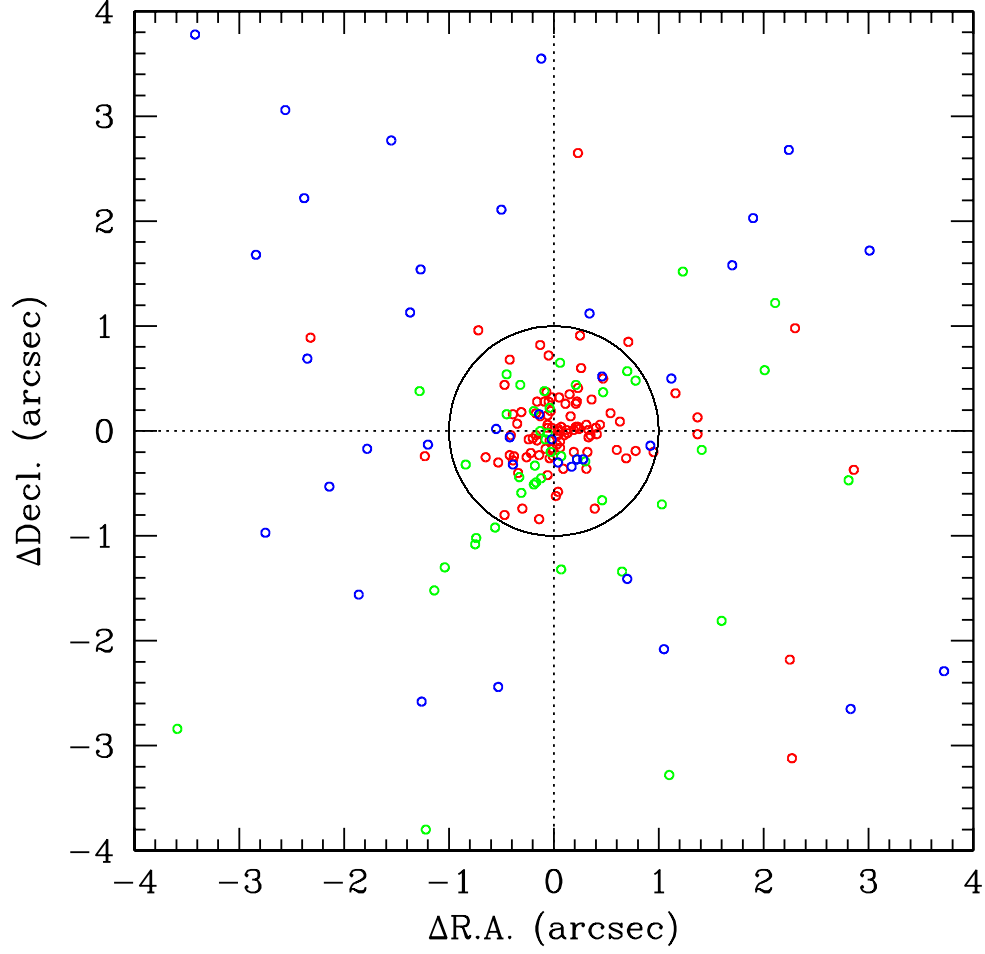


Fig. 10.— For all the *Chandra* sources detected in the fields covered by SOFI, positional offsets of the nearest SOFI sources are plotted. Red, green and blue are soft, medium and hard X-ray sources, respectively. We consider sources within 1'' (central circle) as the counterparts. It is obvious that soft X-ray sources are more likely to have NIR counterparts than harder X-ray sources (see also Table 3).

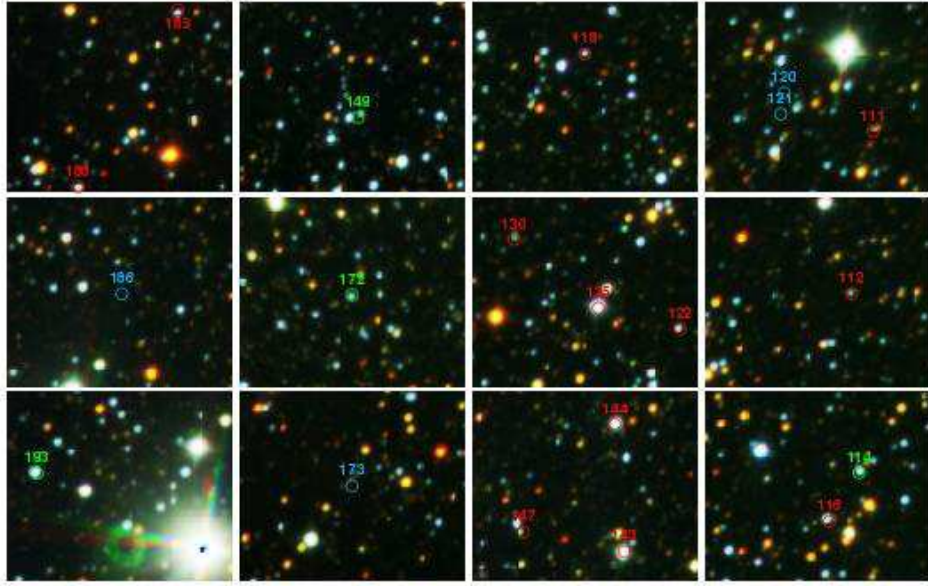


Fig. 11.— NIR identification of the *Chandra* sources in the SOFI “A4” field (see Fig. 3). The pseudo-color image is made by superposing the SOFI *J*, *H* and *K_S* band images in the RGB scheme. All the 20 *Chandra* sources in this field are marked and labeled with source ID numbers in Table 1 in red, green and blue for soft, medium and hard sources, respectively (see section 3.4 for definition of the spectral hardness). Radius of each circle is 1″, which is used to identify the NIR counterparts. Note that all the 16 soft and medium sources have NIR counterparts, whereas none of the four hard sources are identified.

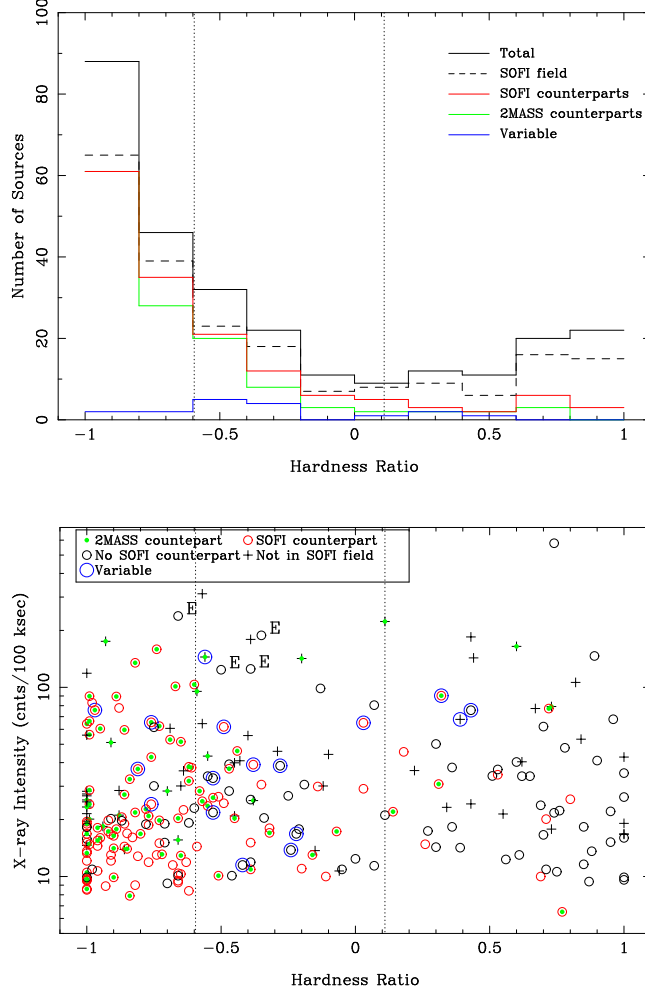


Fig. 12.— Histogram of the number of sources as a function of the spectral hardness ratio (HR) (top) and HR vs. the count rate (bottom). In the top panel, the dashed line indicates the number of sources within the SOFI fields (Fig. 3), and the red line shows the sources having the SOFI near-infrared counterpart. The green line indicates the number of sources having 2MASS counterpart, and the blue line indicates the number of variable sources (Section 3.5.3). In the bottom panel, the sources outside of the SOFI field are shown with crosses, and those inside are with circles: black circles indicate the sources without SOFI counterparts, while red circles are those having the SOFI counterparts. In addition, sources having the 2MASS counterparts are marked with green dots, and variable sources are marked with blue circle. The vertical dotted lines in both figures indicate the boundaries we defined between the soft and medium sources ($HR = -0.595$), and the medium and hard sources ($HR = 0.11$). Source marked with “E” (Sources 208, 210, 213 and 126) in the bottom panel are parts of the extended feature CXOU J184357-035441 (Section 2.2; Ueno et al. 2003).

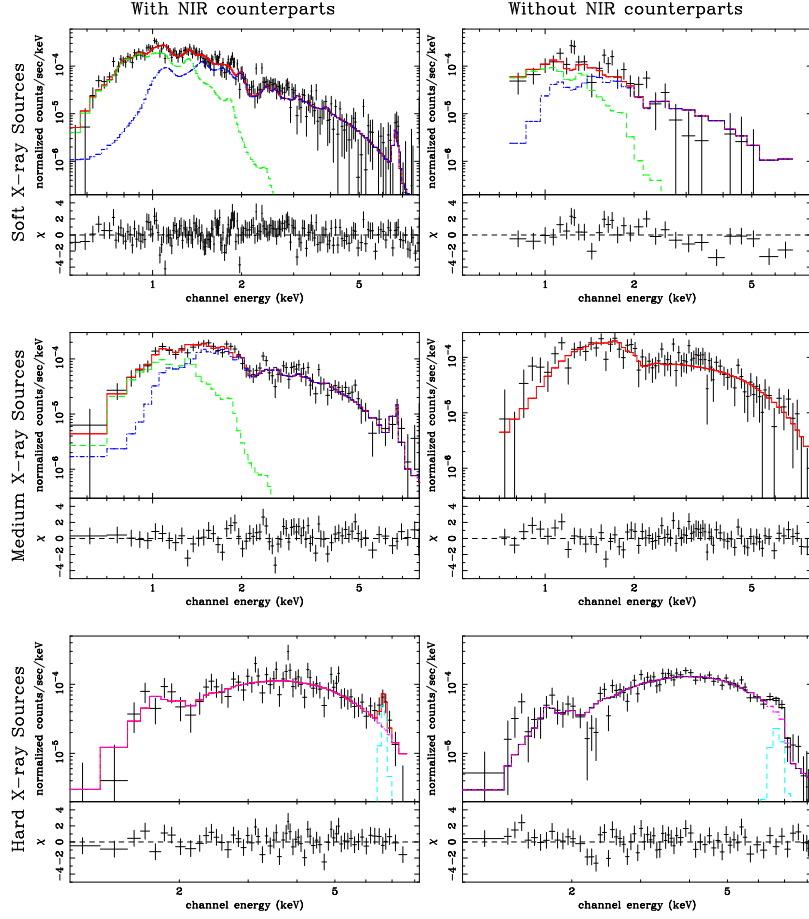


Fig. 13.— Composite energy spectra and model fitting of the point sources grouped by the X-ray spectral hardness and absence or presence of the NIR counterpart. Those having the NIR counterpart are in the left-hand side, and those without the NIR counterpart are in the right-hand side. The top two panels are the soft source spectra, the middle ones are the medium, and the bottom ones the hard. See the text (section 3.5.2) for the fitting models.

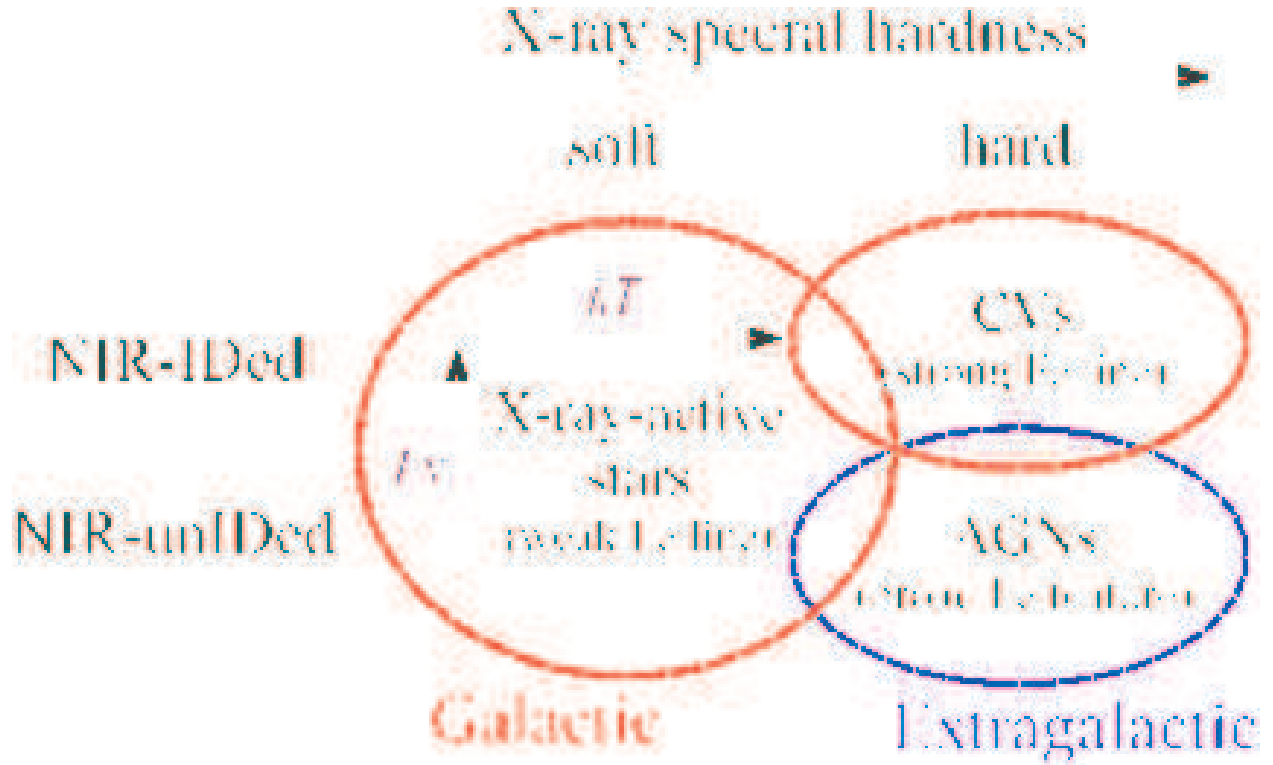


Fig. 14.— Classification of the point X-ray sources according to the X-ray spectral hardness and on the presence or absence of the NIR counterpart.

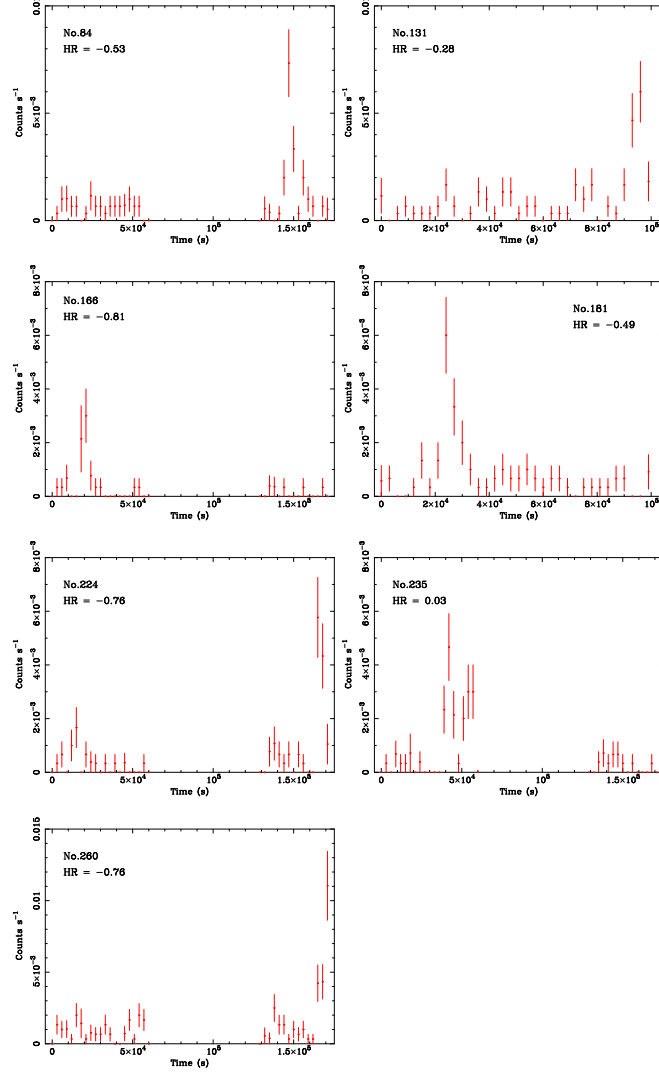


Fig. 15.— Light curves of the seven variable sources exhibiting flare-like phenomena.

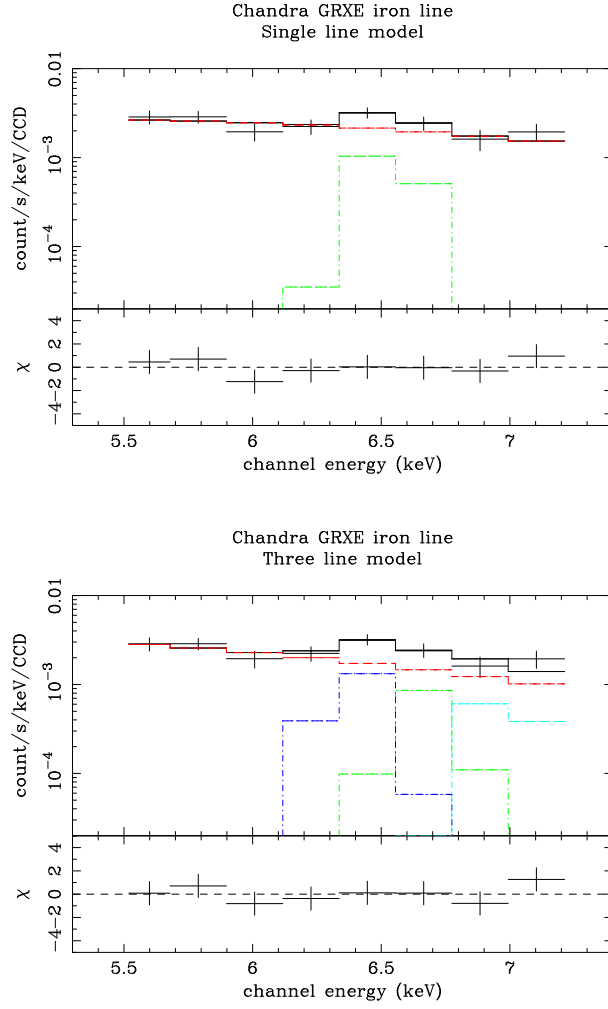


Fig. 16.— The iron line from the Galactic ridge diffuse X-ray emission fitted with a single line (top) or three lines (bottom; differentiated with different colors). Both models fit the observed spectrum equally well.

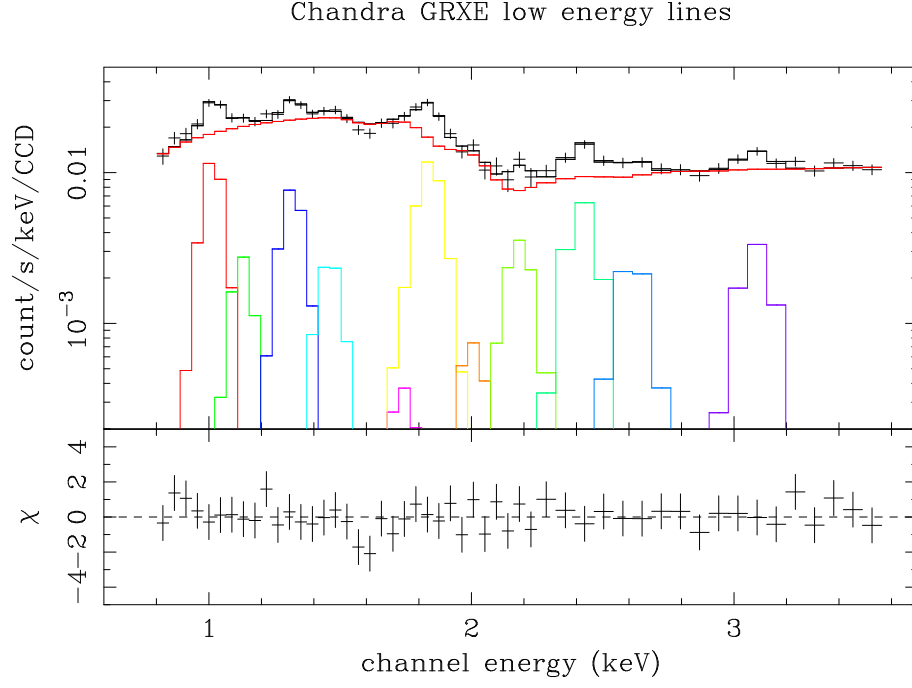


Fig. 17.— Emission lines from the Galactic ridge diffuse X-ray emission in the soft energy band. Eleven gaussians (differentiated with different colors) are put with a power-law continuum.

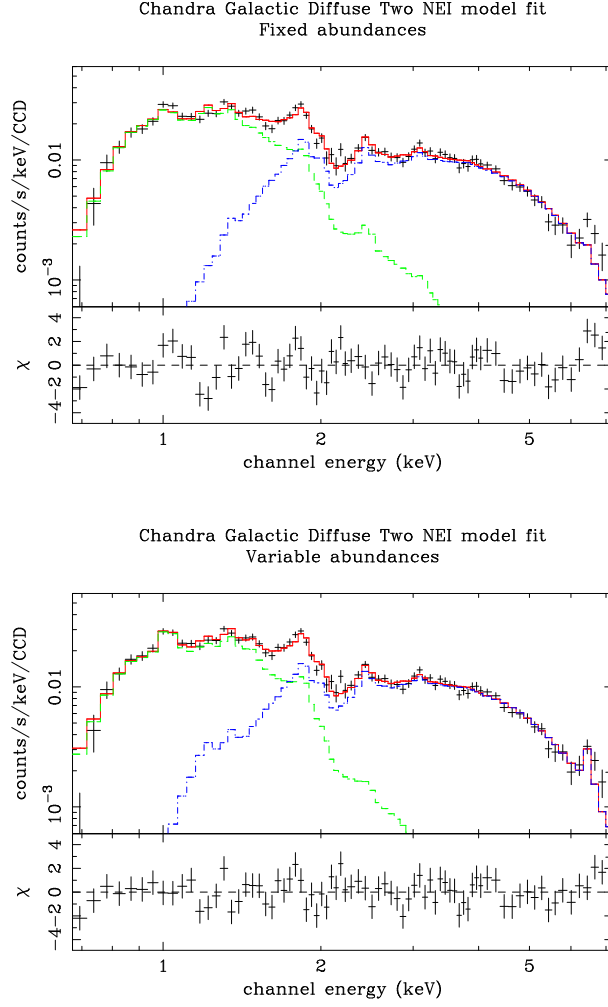


Fig. 18.— Spectral fitting of the Galactic diffuse emission with a two component NEI model (Masai 1984) with fixed abundances for each component (top) or variable abundances (bottom). Note that the iron line (~ 6.7 keV) and neon line (~ 1.0 keV) features are fitted in the bottom figure, but not in the top.

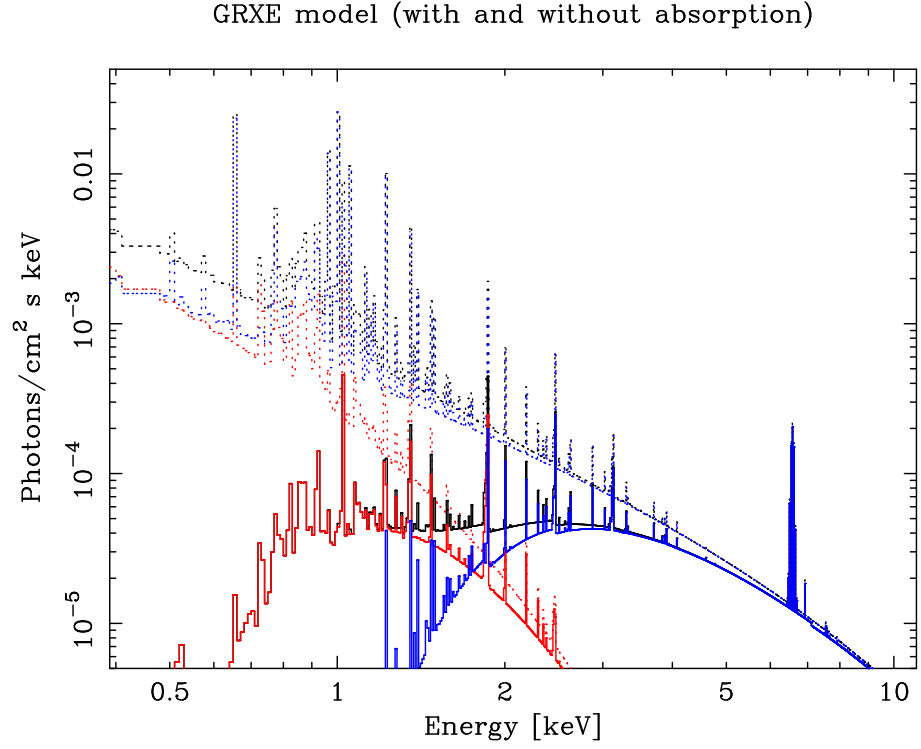


Fig. 19.— Best fit spectral model used in Fig. 18 including interstellar absorption (solid lines) and removing the absorption (dotted lines). Hard component is drawn in blue, soft component is in red, and total is in black.

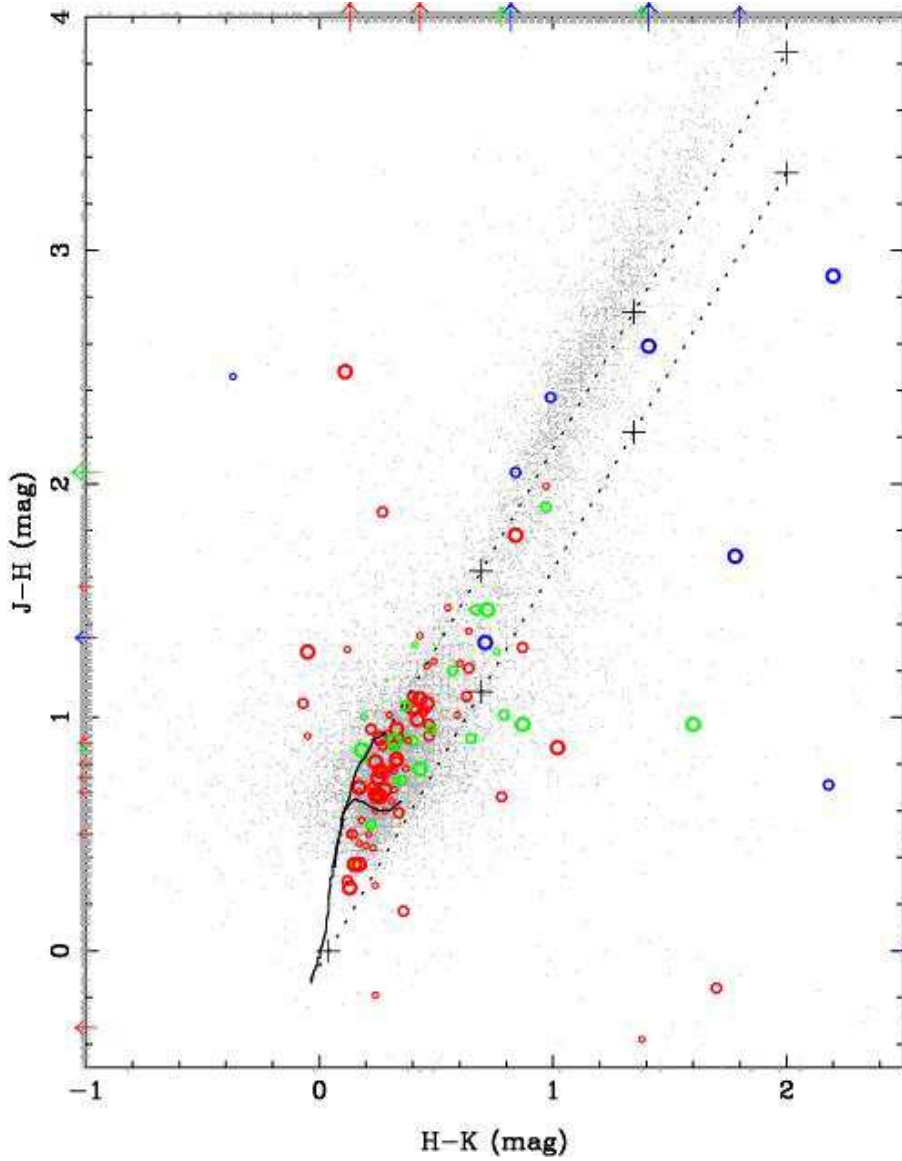


Fig. 20.— NIR color-color diagram of all the SOFI sources (gray) and the *Chandra* sources with NIR counterparts (red, green and blue circles for soft, medium and hard sources, respectively). The symbol size for *Chandra* sources is approximately proportional to the X-ray counting rates. Solid curves indicate the loci for dwarfs (main sequence stars) and giants, and dotted lines show the reddening (towards upper-right), such that distance between the crosses correspond to $A_V=10$ mag (data taken from Cox 1999). Sources detected only in two bands are marked at the border of the graph. Note that there are many SOFI sources which are detected only in one band, thus cannot be plotted in this diagram.

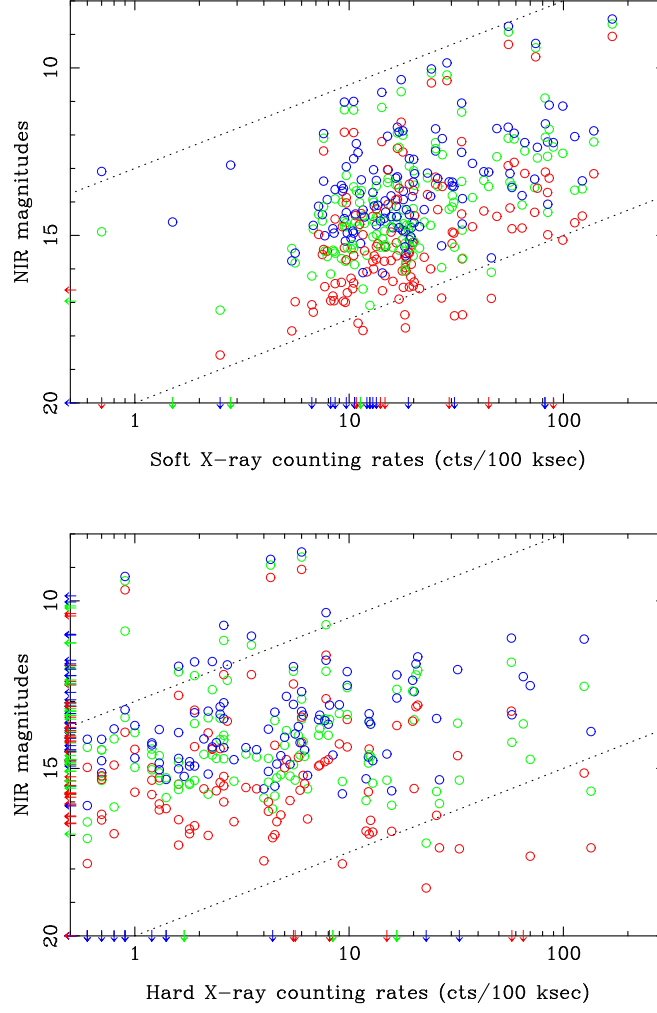


Fig. 21.— Correlation between the X-ray counting rates (top = 0.5 – 2 keV band, bottom = 2 – 10 keV band) and the NIR magnitudes (red= J , green = H and blue = K_S). The black dotted lines indicate the slopes for the sources with the constant luminosities at different distances.

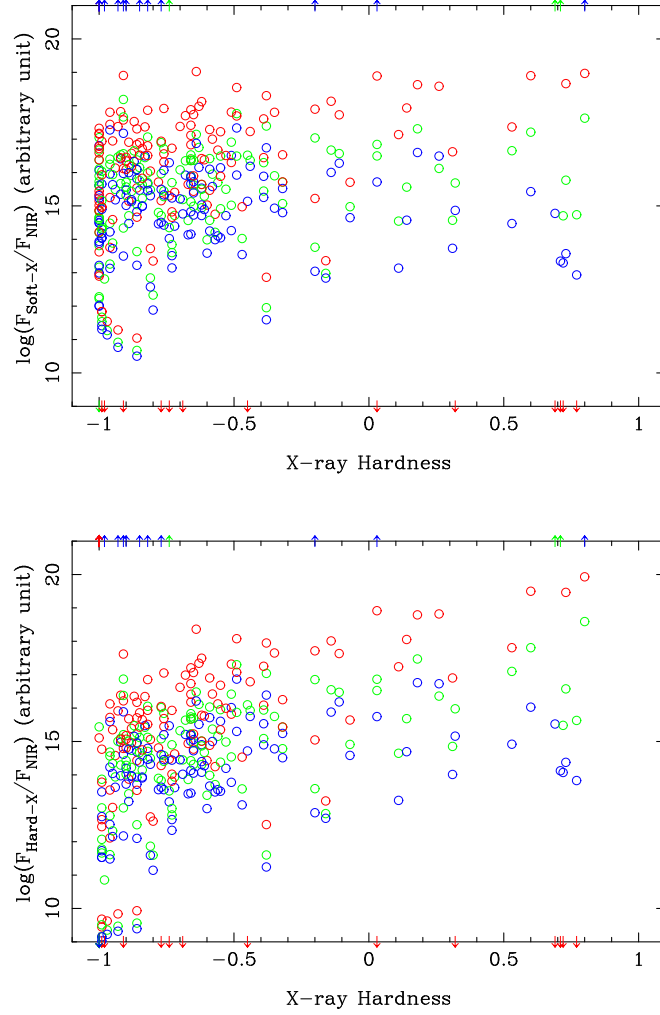


Fig. 22.— X-ray spectral hardness versus the X-ray and NIR flux ratio. Top panel gives the soft X-ray flux over NIR flux ratio, and the bottom is for the hard X-ray flux. Red, green and blue colors indicate J , H and K_S band fluxes, respectively.

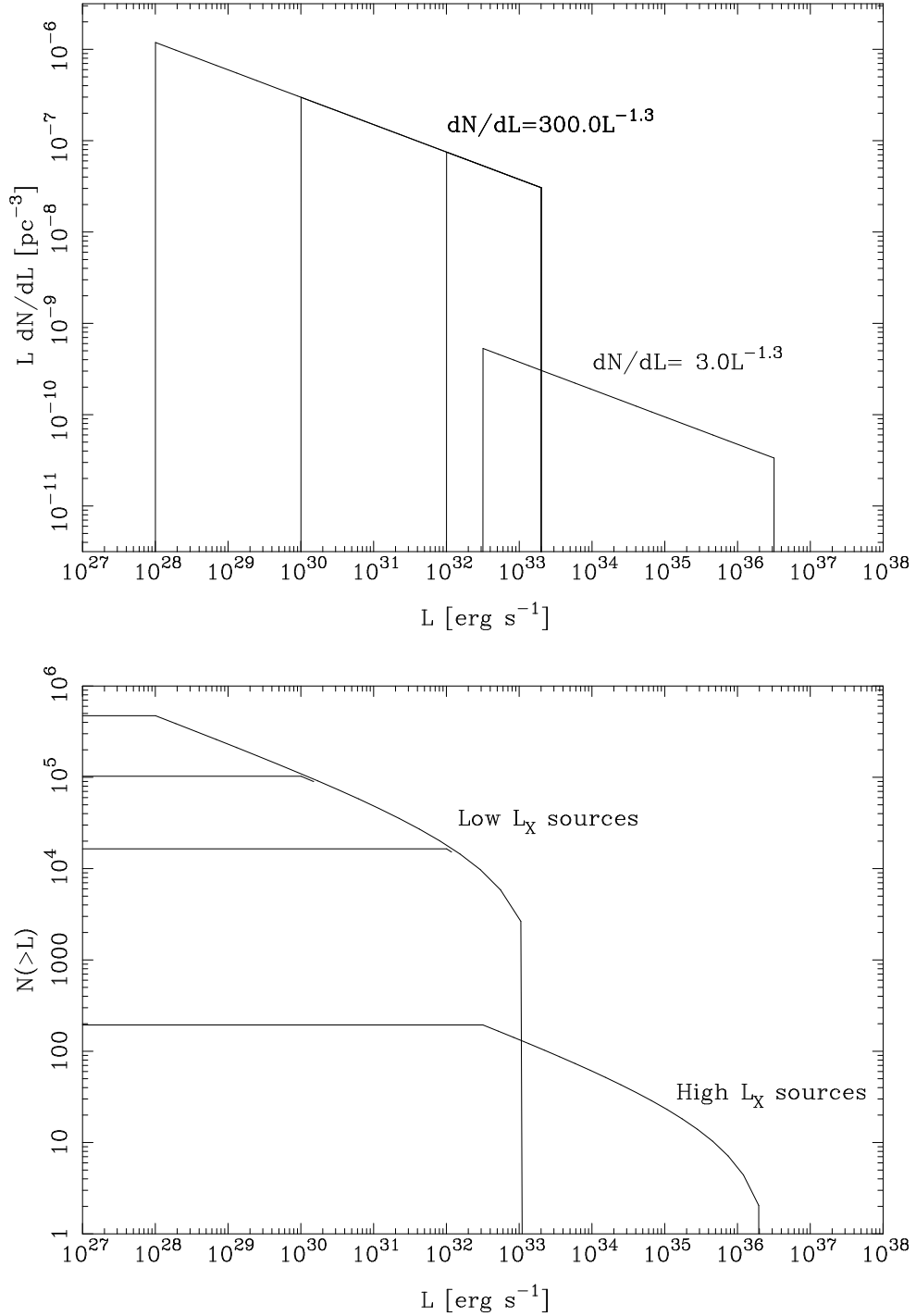


Fig. 23.— Top: Differential X-ray source luminosity functions we adopt to model the $\log N - \log S$ curve (see Fig. 24). We consider distinct high luminosity and low luminosity source populations. For the low luminosity source population, we try three different lower cut-off luminosities. Bottom: Cumulative luminosity functions obtained by integrating over the Galactic source distribution.

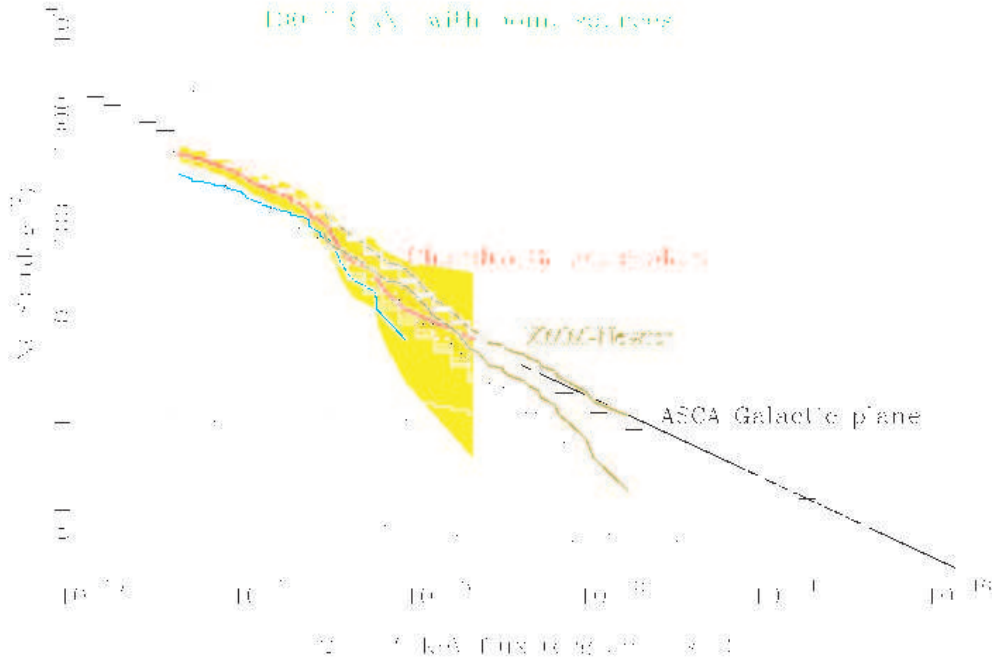


Fig. 24.— Modeling of 2 – 10 keV $\log N - \log S$ curves on the Galactic plane obtained with *Chandra* (same as in Fig. 9), *XMM* (Hands et al. 2004) and *ASCA* (Sugizaki et al. 2001). Galactic luminosity functions in Fig. 23 are adopted. As in Fig. 9, the line in cyan indicates the sources with near-infrared counterparts. Note, three different lower cut-off luminosities in the low luminosity source population (Fig. 23 top) are reflected in only small differences in the $\log N - \log S$ curves.

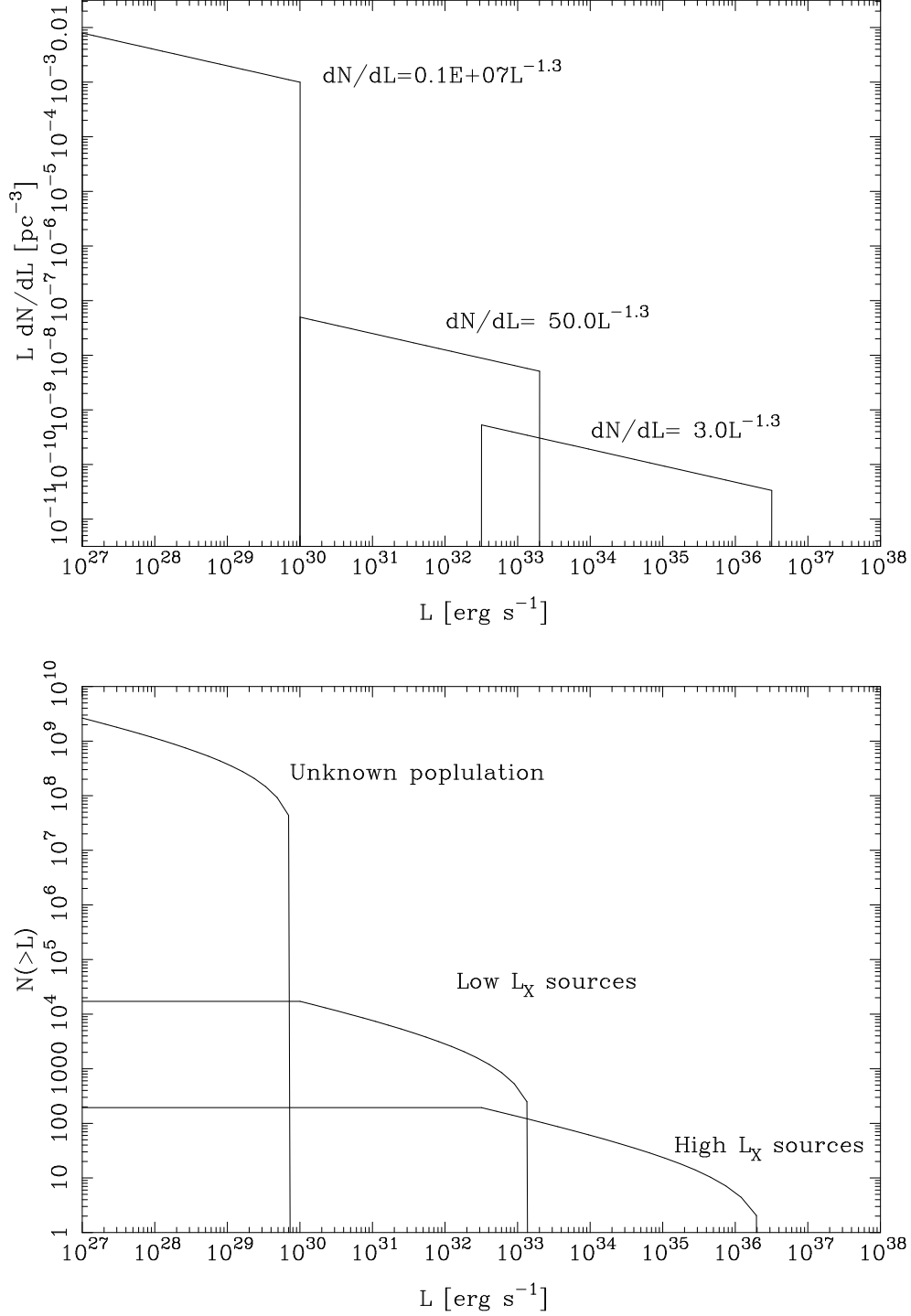


Fig. 25.— Top: Differential X-ray source luminosity functions assuming a hypothetical population of very dim sources ($L_X \leq 10^{30} \text{ erg s}^{-1}$) to model the $\log N - \log S$ curve (see Fig. 26). Bottom: Cumulative luminosity functions obtained by integrating over the source distributions above.

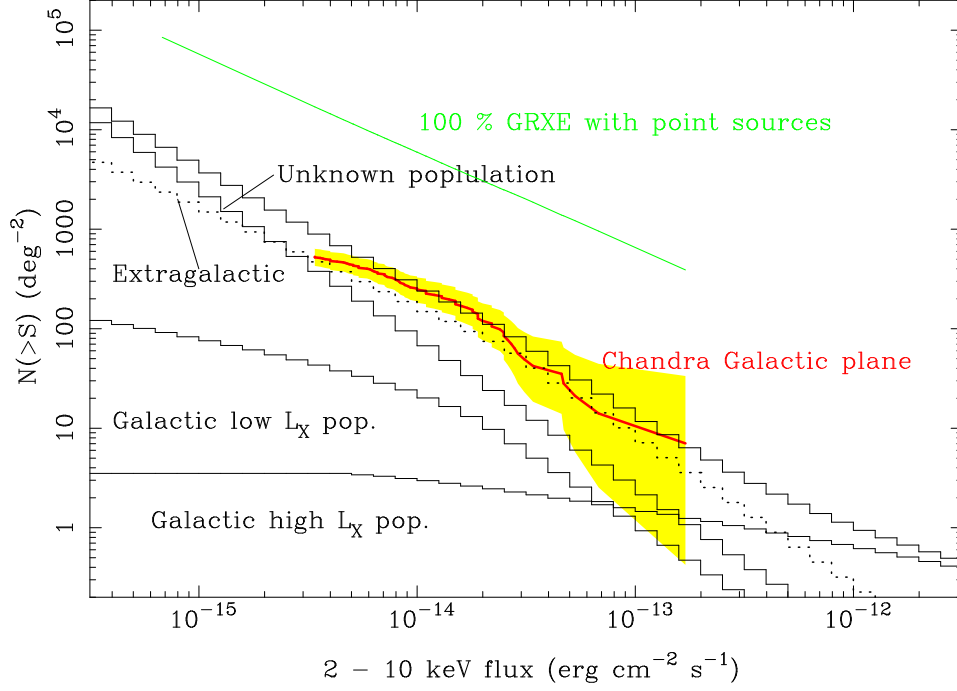


Fig. 26.— A trial modeling of 2 – 10 keV $\log N - \log S$ curve on the Galactic plane obtained with *Chandra* (same as in Fig. 9), assuming the hypothetical luminosity functions in Fig. 25. Note, introducing extremely dim and numerous point sources below $L_X \leq 10^{30} \text{ erg s}^{-1}$ hardly contributes to the Galactic Ridge X-ray Emission flux.

Table 1. Detected Source List

| ID ^a | AO | R.A. | Dec. | Error | Significance | Normalized counts | Hardness | Flux | NIR counterpart | | | | |
|-----------------|----|--------------------------|-------------|----------|---------------------------------|---------------------------------|--------------|--|-------------------------|------------------------|----------------|----------------|------------------|
| | | (hh:mm:ss.ss) (J2000) | (d:mm:ss.s) | (arcsec) | (σ) Total/Soft/Hard | (cnts/100ks) Total/Soft/Hard | (H-S)/(H+S) | (ergs s ⁻¹ cm ⁻²) 0.5-2keV/2-10keV | ID ^b | seperation (arcsec) | J^c (mag) | H^c (mag) | K_S^c (mag) |
| 1 | 2 | 18:42:51.77 | -3 51 11.2 | 0.86 | 5.5/5.1/0.0 | 27.3/27.1/0.0 | -1.00 ± 0.09 | 4.0E-16/1.6E-16 | OoF | ... | ... | ... | ... |
| 2 ^T | 2 | 18:42:53.53 | -3 49 19.6 | 0.93 | 6.9/3.6/6.3 | 67.7/21.3/48.8 | 0.39 ± 0.12 | 3.5E-16/1.0E-14 | OoF | ... | ... | ... | ... |
| 3 | 2 | 18:42:58.30 | -3 53 28.1 | 0.49 | 11.3/0.0/11.4 | 79.2/11.0/70.0 | 0.73 ± 0.08 | 4.2E-17/3.1E-14 | J18425832-0353271 | 1.00 | 17.62 | 14.73 | 12.53 |
| 4 ^T | 2 | 18:43:00.41 | -3 53 48.9 | 0.36 | 19.0/18.5/6.0 | 144.7/112.9/32.1 | -0.56 ± 0.07 | 2.5E-15/1.0E-14 | J18430043-0353486 | 0.36 | 14.62 | 13.65 | 12.05 |
| 5 | 2 | 18:43:01.50 | -3 50 47.3 | 0.69 | 5.0/0.0/5.5 | 17.8/2.5/15.8 | 0.73 ± 0.20 | 8.8E-18/6.4E-15 | OoF | ... | ... | ... | ... |
| 6 | 2 | 18:43:01.83 | -3 54 42.4 | 0.48 | 7.4/6.7/2.0 | 45.9/29.8/16.3 | -0.29 ± 0.15 | 9.5E-16/3.9E-15 | OoF | ... | ... | ... | ... |
| 7 | 2 | 18:43:06.14 | -3 54 54.8 | 0.43 | 4.1/4.6/0.0 | 20.9/15.2/5.8 | -0.45 ± 0.21 | 4.3E-16/1.8E-15 | OoF | ... | ... | ... | ... |
| 8 | 2 | 18:43:06.88 | -3 55 37.0 | 0.35 | 8.1/6.0/4.0 | 30.1/17.0/13.2 | -0.12 ± 0.19 | 2.1E-16/6.2E-15 | OoF | ... | ... | ... | ... |
| 9 | 2 | 18:43:07.25 | -3 49 55.2 | 0.55 | 5.2/8.2/0.0 | 28.2/28.1/0.0 | -1.00 ± 0.08 | 8.3E-16/3.4E-16 | OoF | ... | ... | ... | ... |
| 10 | 2 | 18:43:07.27 | -3 48 58.4 | 0.75 | 4.1/0.0/4.0 | 16.8/0.0/17.2 | 1.00 ± 0.13 | 1.1E-17/8.0E-15 | OoF | ... | ... | ... | ... |
| 11 | 2 | 18:43:07.98 | -3 53 17.1 | 0.40 | 8.1/7.2/0.0 | 30.6/18.3/12.4 | -0.19 ± 0.19 | 2.3E-16/6.8E-15 | No | ... | ... | ... | ... |
| 12 | 2 | 18:43:08.73 | -3 50 01.8 | 0.53 | 4.6/3.5/2.4 | 10.7/6.3/5.7 | -0.06 ± 0.32 | 4.0E-17/1.2E-15 | OoF | ... | ... | ... | ... |
| 13 | 2 | 18:43:10.86 | -3 55 35.5 | 0.38 | 4.3/6.3/0.0 | 20.2/19.3/0.9 | -0.91 ± 0.10 | 5.0E-16/2.0E-16 | No | ... | ... | ... | ... |
| 14 | 2 | 18:43:11.41 | -3 59 50.1 | 0.46 | 8.1/7.6/1.8 | 39.9/28.9/10.9 | -0.45 ± 0.15 | 7.2E-16/3.0E-15 | OoF | ... | ... | ... | ... |
| 15 | 2 | 18:43:11.81 | -3 58 23.7 | 0.27 | 7.2/8.8/0.0 | 26.7/26.7/0.0 | -1.00 ± 0.08 | 7.0E-16/2.8E-16 | OoF | ... | ... | ... | ... |
| 16 | 2 | 18:43:12.15 | -3 48 16.2 | 0.72 | 3.6/6.0/0.0 | 21.1/19.7/1.3 | -0.88 ± 0.15 | 7.2E-16/2.9E-16 | J18431219-0348167 | 0.93 | 15.28 | 14.62 | 13.84 |
| 17 | 2 | 18:43:12.42 | -3 57 36.8 | 0.49 | 4.3/4.0/0.0 | 15.6/13.0/2.6 | -0.66 ± 0.22 | 3.8E-16/1.6E-15 | J18431239-0357363 | 0.61 | 16.00 | 14.01 | 13.04 |
| 18 | 2 | 18:43:12.87 | -3 50 42.0 | 0.55 | 4.6/4.9/0.0 | 14.8/14.8/0.0 | -1.00 ± 0.15 | 4.8E-16/1.9E-16 | OoF | ... | ... | ... | ... |
| 19 | 2 | 18:43:12.92 | -3 49 36.8 | 0.49 | 5.9/6.8/0.0 | 25.4/25.3/0.0 | -1.00 ± 0.09 | 7.9E-16/3.2E-16 | J18431289-0349369 | 0.36 | 13.47 | 12.41 | 12.48 |
| 20 | 2 | 18:43:13.36 | -4 02 36.1 | 0.80 | 5.2/5.5/0.0 | 29.5/25.3/4.3 | -0.71 ± 0.15 | 8.2E-16/3.4E-15 | OoF | ... | ... | ... | ... |
| 21 | 2 | 18:43:13.77 | -3 57 07.4 | 0.35 | 6.4/6.9/0.0 | 20.1/20.0/0.1 | -0.99 ± 0.11 | 5.9E-16/2.4E-16 | J18431378-0357073 | 0.28 | 13.66 | 13.07 | 12.73 |
| 22 | 2 | 18:43:14.45 | -3 52 11.5 | 0.32 | 4.2/4.3/0.0 | 12.7/12.7/0.0 | -1.00 ± 0.17 | 2.6E-16/1.1E-16 | No | ... | ... | ... | ... |
| 23 | 2 | 18:43:14.97 | -3 58 12.8 | 0.45 | 4.9/3.8/0.0 | 16.3/10.5/5.8 | -0.29 ± 0.26 | 4.1E-16/1.7E-15 | OoF | ... | ... | ... | ... |
| 24 | 2 | 18:43:15.29 | -3 54 19.5 | 0.17 | 9.1/9.7/0.0 | 24.1/24.2/0.1 | -0.99 ± 0.08 | 6.9E-16/2.8E-16 | S687/J18431530-0354190 | 0.38 | 10.45 | 10.15 | 10.03 |
| 25 | 2 | 18:43:15.29 | -3 56 17.2 | 0.22 | 10.6/10.7/0.0 | 30.1/26.3/3.8 | -0.75 ± 0.13 | 8.6E-16/3.6E-15 | No | ... | ... | ... | ... |
| 26 | 2 | 18:43:15.40 | -3 50 49.1 | 0.34 | 4.5/5.0/0.0 | 13.9/12.9/1.0 | -0.86 ± 0.15 | 6.1E-16/2.5E-16 | J18431539-0350483 | 0.74 | 14.43 | 13.93 | 13.72 |
| 27 | 2 | 18:43:15.54 | -3 47 58.5 | 0.67 | 4.7/0.0/4.9 | 21.4/4.7/15.9 | 0.55 ± 0.21 | 1.3E-16/4.0E-15 | OoF | ... | ... | ... | ... |
| 28 | 2 | 18:43:15.81 | -3 56 40.4 | 0.42 | 4.3/0.0/2.9 | 13.7/8.5/6.3 | -0.15 ± 0.28 | 7.3E-17/2.2E-15 | OoF | ... | ... | ... | ... |
| 29 | 2 | 18:43:17.43 | -3 56 00.2 | 0.22 | 5.9/3.9/2.8 | 13.0/7.6/5.5 | -0.16 ± 0.30 | 1.3E-16/3.9E-15 | S1031/J18431748-0355597 | 0.90 | 12.48 | 12.10 | 11.96 |
| 30 | 2 | 18:43:17.43 | -3 57 32.7 | 0.23 | 7.0/7.4/0.0 | 19.8/19.1/0.7 | -0.92 ± 0.11 | 5.5E-16/2.2E-16 | S1018 | 0.13 | 16.54 | 15.25 | 15.13 |
| 31 | 2 | 18:43:17.47 | -3 48 52.6 | 0.40 | 5.3/5.9/0.0 | 18.4/18.4/0.0 | -1.00 ± 0.12 | 4.9E-16/2.0E-16 | S1038 | 0.63 | 16.06 | 15.78 | 15.54 |
| 32 | 2 | 18:43:17.97 | -3 47 14.9 | 0.82 | 3.6/4.5/0.0 | 19.6/19.5/0.0 | -1.00 ± 0.12 | 4.5E-16/1.8E-16 | OoF | ... | ... | ... | ... |
| 33 | 2 | 18:43:18.18 | -3 47 32.4 | 0.89 | 3.0/4.0/0.0 | 14.6/14.5/0.0 | -1.00 ± 0.16 | 4.1E-16/1.7E-16 | OoF | ... | ... | ... | ... |
| 34 | 2 | 18:43:18.41 | -4 00 54.9 | 0.77 | 3.6/4.1/0.0 | 9.7/9.7/0.0 | -1.00 ± 0.23 | 4.2E-16/1.7E-16 | OoF | ... | ... | ... | ... |
| 35 | 2 | 18:43:18.59 | -3 58 52.1 | 0.35 | 5.8/6.8/0.0 | 19.5/19.5/0.0 | -1.00 ± 0.11 | 4.6E-16/1.9E-16 | S1360 | 0.36 | 15.86 | 15.08 | 14.77 |
| 36 | 2 | 18:43:18.73 | -3 54 25.2 | 0.20 | 5.1/3.3/0.0 | 11.0/6.7/4.4 | -0.20 ± 0.31 | 7.3E-17/2.2E-15 | S1398 | 0.22 | 17.07 | 16.21 | ... |
| 37 | 2 | 18:43:18.95 | -3 53 27.3 | 0.24 | 4.4/4.2/0.0 | 12.8/11.6/1.2 | -0.81 ± 0.21 | 4.3E-16/1.7E-16 | S1479 | 0.74 | 14.98 | 14.42 | 14.24 |
| 38 | 2 | 18:43:19.01 | -3 59 33.4 | 0.38 | 8.8/0.0/8.6 | 33.9/6.4/27.4 | 0.62 ± 0.14 | 1.8E-17/1.3E-14 | No | ... | ... | ... | ... |
| 39 | 2 | 18:43:19.22 | -3 57 31.9 | 0.28 | 4.7/4.8/0.0 | 13.0/11.3/1.7 | -0.74 ± 0.21 | 3.4E-16/1.4E-15 | S1544 | 0.73 | ... | ... | 15.24 |
| 40 | 2 | 18:43:19.47 | -4 01 36.9 | 0.73 | 3.3/5.1/0.0 | 19.1/19.1/0.0 | -1.00 ± 0.12 | 5.5E-16/2.2E-16 | OoF | ... | ... | ... | ... |
| 41 | 2 | 18:43:19.61 | -3 55 02.1 | 0.25 | 3.8/4.2/0.0 | 8.9/8.6/0.3 | -0.93 ± 0.22 | 2.3E-16/9.2E-17 | S1652 | 0.81 | 16.44 | 15.53 | ... |
| 42 | 2 | 18:43:20.55 | -3 48 59.9 | 0.24 | 8.1/0.0/8.7 | 26.3/0.0/26.3 | 1.00 ± 0.08 | 2.1E-17/1.5E-14 | No | ... | ... | ... | ... |
| 43 | 2 | 18:43:20.56 | -3 49 03.3 | 0.31 | 9.1/0.0/10.1 | 35.2/0.0/35.3 | 1.00 ± 0.06 | 2.0E-17/1.5E-14 | No | ... | ... | ... | ... |
| 44 | 2 | 18:43:20.86 | -3 52 46.5 | 0.11 | 20.6/8.3/14.9 | 50.2/17.6/32.7 | 0.30 ± 0.14 | 3.5E-16/1.1E-14 | No | ... | ... | ... | ... |
| 45 | 2 | 18:43:21.10 | -3 52 15.0 | 0.16 | 4.7/0.0/4.7 | 9.4/0.6/8.6 | 0.87 ± 0.21 | 4.7E-18/3.4E-15 | No | ... | ... | ... | ... |
| 46 | 2 | 18:43:21.11 | -3 54 30.0 | 0.20 | 5.0/0.0/4.2 | 10.0/1.5/8.4 | 0.69 ± 0.26 | 6.4E-18/4.6E-15 | S2107 | 0.21 | ... | ... | 14.60 |
| 47 | 2 | 18:43:21.22 | -3 49 31.2 | 0.37 | 9.0/11.5/0.0 | 42.8/37.6/5.1 | -0.76 ± 0.10 | 9.6E-16/4.0E-15 | S2159/J18432128-0349314 | 0.97 | 14.74 | 13.87 | 12.85 |
| 48 | 2 | 18:43:21.37 | -4 01 02.9 | 0.27 | 26.1/12.0/22.0 | 184.7/52.7/131.9 | 0.43 ± 0.07 | 1.1E-15/3.4E-14 | OoF | ... | ... | ... | ... |
| 49 | 2 | 18:43:21.62 | -3 55 28.0 | 0.23 | 4.5/4.8/0.0 | 9.8/9.7/0.0 | -1.00 ± 0.22 | 5.0E-16/2.0E-16 | S2284 | 0.24 | 14.03 | 14.62 | ... |

Table 1—Continued

| ID ^a | AO | R.A. (hh:mm:ss.ss) (J2000) | Dec. (d:mm:ss.s) | Error (arcsec) | Significance (σ) Total/Soft/Hard | Normalized counts (cnts/100ks) Total/Soft/Hard | Hardness (H-S)/(H+S) | Flux (ergs s ⁻¹ cm ⁻²) 0.5-2keV/2-10keV | NIR counterpart | | | | |
|-----------------|-----|----------------------------------|---------------------|-------------------|---|--|-------------------------|--|-------------------------|------------------------|-------------------|-------------------|-------------------|
| | | | | | | | | | ID ^b | separation (arcsec) | J^c (mag) | H^c (mag) | K_S^c (mag) |
| 50 | 2 | 18:43:21.76 | -4 00 39.6 | 0.53 | 4.9/5.7/0.0 | 18.4/17.9/0.5 | -0.94 \pm 0.12 | 6.1E-16/2.5E-16 | J18432180-0400395 | 0.73 | 14.88 | 14.24 | 13.93 |
| 51 | 2 | 18:43:21.81 | -3 53 03.3 | 0.19 | 8.3/8.0/0.0 | 18.7/16.5/2.2 | -0.77 \pm 0.17 | 4.0E-16/1.7E-15 | S2354/J18432182-0353031 | 0.24 | 13.94 | 13.49 | 13.29 |
| 52 | 2 | 18:43:22.09 | -3 54 26.4 | 0.17 | 7.4/7.5/0.0 | 16.1/14.7/1.4 | -0.83 \pm 0.17 | 6.1E-16/2.5E-16 | S2458 | 0.34 | 16.20 | 15.28 | 15.33 |
| 53 | 2 | 18:43:22.82 | -3 52 28.6 | 0.24 | 4.4/0.0/2.8 | 10.6/1.3/9.1 | 0.75 \pm 0.25 | 6.2E-18/4.5E-15 | No | ... | ... | ... | ... |
| 54 | 2 | 18:43:22.98 | -3 57 53.0 | 0.19 | 7.5/7.7/0.0 | 17.8/16.8/0.9 | -0.89 \pm 0.11 | 6.0E-16/2.4E-16 | S2739/J18432299-0357526 | 0.47 | 13.92 | 13.48 | 13.25 |
| 55 | 2 | 18:43:23.03 | -3 57 25.3 | 0.26 | 5.2/5.0/0.0 | 11.9/9.6/2.2 | -0.63 \pm 0.27 | 3.0E-16/1.2E-15 | S2749 | 0.66 | 17.00 | 15.77 | 15.17 |
| 56 | 2 | 18:43:23.30 | -3 48 51.7 | 0.31 | 15.3/17.2/0.0 | 64.1/64.1/0.0 | -1.00 \pm 0.03 | 2.9E-15/1.2E-15 | S2844/J18432331-0348521 | 0.47 | 14.78 | 14.09 | 13.81 |
| 57 | 2 | 18:43:23.39 | -3 58 05.1 | 0.21 | 9.6/10.9/0.0 | 27.1/25.3/1.9 | -0.86 \pm 0.11 | 8.1E-16/3.3E-16 | S2871/J18432340-0358050 | 0.19 | 13.26 | 12.23 | 11.82 |
| 58 | 2 | 18:43:23.62 | -3 53 14.1 | 0.21 | 4.6/3.4/0.0 | 10.9/7.5/3.3 | -0.39 \pm 0.30 | 2.5E-16/1.0E-15 | S2932/J18432360-0353138 | 0.13 | 15.57 | 14.57 | 14.38 |
| 59 | 2 | 18:43:23.68 | -3 51 40.6 | 0.23 | 6.6/6.0/0.0 | 14.4/13.4/1.0 | -0.86 \pm 0.19 | 5.2E-16/2.1E-16 | S2956 | 0.09 | 15.71 | 14.97 | 14.69 |
| 60 | 2 | 18:43:23.72 | -4 00 26.0 | 0.42 | 8.5/5.4/3.1 | 40.9/28.4/11.4 | -0.43 \pm 0.15 | 7.5E-16/3.1E-15 | OoF | ... | ... | ... | ... |
| 61 | 2 | 18:43:23.89 | -3 53 31.4 | 0.18 | 5.4/2.8/4.6 | 17.4/6.2/10.8 | 0.27 \pm 0.25 | 1.1E-16/3.4E-15 | No | ... | ... | ... | ... |
| 62 ^T | 2 | 18:43:23.96 | -3 57 58.9 | 0.18 | 13.2/10.7/5.2 | 39.0/27.0/12.0 | -0.38 \pm 0.15 | 8.7E-16/3.6E-15 | S3040 | 0.65 | 16.87 | 15.96 | 15.31 |
| 63 | 2 | 18:43:24.33 | -4 03 38.5 | 1.09 | 0.0/4.3/0.0 | 21.5/21.5/0.0 | -1.00 \pm 0.11 | 2.2E-16/8.7E-17 | OoF | ... | ... | ... | ... |
| 64 | 2 | 18:43:24.47 | -3 53 49.8 | 0.06 | 42.1/39.3/9.0 | 101.2/84.3/16.7 | -0.67 \pm 0.07 | 2.2E-15/9.1E-15 | S3203/J18432446-0353495 | 0.05 | 13.72 | 12.64 | 12.21 |
| 65 | 2 | 18:43:24.81 | -3 59 16.2 | 0.34 | 5.6/5.6/0.0 | 16.7/16.0/0.7 | -0.91 \pm 0.12 | 5.8E-16/2.4E-16 | S3312 | 0.47 | 16.37 | 15.36 | 14.77 |
| 66 | 2 | 18:43:25.04 | -3 57 51.0 | 0.22 | 6.5/6.9/0.0 | 17.3/16.6/0.7 | -0.92 \pm 0.12 | 6.2E-16/2.5E-16 | S3394/J18432504-0357511 | 0.17 | 15.22 | 14.45 | 14.13 |
| 67 | 2 | 18:43:25.25 | -3 59 15.3 | 0.30 | 6.6/6.4/0.0 | 23.6/18.3/5.3 | -0.55 \pm 0.19 | 6.1E-16/2.5E-15 | S3450/J18432523-0359150 | 0.55 | 15.96 | 15.23 | 14.88 |
| 68 | 2 | 18:43:26.14 | -3 56 49.7 | 0.14 | 11.2/9.4/2.3 | 26.4/19.9/6.4 | -0.51 \pm 0.18 | 7.1E-16/2.9E-15 | S3833 | 0.42 | 16.51 | 15.61 | 15.21 |
| 69 | 2 | 18:43:26.41 | -3 57 05.9 | 0.17 | 4.0/0.0/4.2 | 9.9/0.0/9.8 | 1.00 \pm 0.21 | 6.5E-18/4.7E-15 | No | ... | ... | ... | ... |
| 70 | 1 | 18:43:28.34 | -4 07 33.2 | 0.31 | 21.3/25.4/0.0 | 175.1/169.0/6.0 | -0.93 \pm 0.03 | 4.2E-15/1.7E-15 | J18432835-0407331 | 0.26 | 9.06 | 8.69 | 8.54 |
| 71 | 2 | 18:43:28.35 | -3 46 18.2 | 0.76 | 4.0/3.8/0.0 | 17.4/17.4/0.0 | -1.00 \pm 0.13 | 6.6E-16/2.7E-16 | OoF | ... | ... | ... | ... |
| 72 | 2 | 18:43:28.67 | -3 56 22.8 | 0.15 | 4.0/3.4/0.0 | 8.4/6.8/1.6 | -0.62 \pm 0.30 | 1.8E-16/7.2E-16 | S4885 | 0.27 | 17.29 | 14.81 | 14.70 |
| 73 | 2 | 18:43:28.91 | -3 57 33.3 | 0.12 | 10.8/10.6/0.0 | 22.7/20.2/2.5 | -0.78 \pm 0.14 | 5.1E-16/2.1E-15 | S4992/J18432891-0357332 | 0.04 | 14.41 | 13.50 | 13.16 |
| 74 | 2 | 18:43:29.11 | -3 59 42.3 | 0.39 | 4.3/0.0/2.5 | 14.8/5.4/9.3 | 0.26 \pm 0.27 | 8.2E-17/2.5E-15 | S5111 | 0.69 | 17.85 | 15.39 | 15.76 |
| 75 | 2 | 18:43:29.26 | -3 50 50.9 | 0.25 | 6.7/7.1/0.0 | 16.4/15.7/0.8 | -0.90 \pm 0.12 | 4.7E-16/1.9E-16 | S5148/J18432926-0350504 | 0.16 | 14.90 | 14.12 | 13.82 |
| 76 | 2 | 18:43:29.32 | -3 56 48.7 | 0.15 | 8.9/0.0/9.3 | 22.1/0.5/21.5 | 0.95 \pm 0.09 | 1.5E-17/1.1E-14 | No | ... | ... | ... | ... |
| 77 | 1 | 18:43:29.33 | -4 05 19.4 | 0.48 | 3.9/5.3/0.0 | 23.3/23.2/0.0 | -1.00 \pm 0.11 | 9.2E-16/3.7E-16 | J18432934-0405185 | 0.84 | 13.78 | 13.28 | 13.14 |
| 78 | 2 | 18:43:29.55 | -3 46 56.5 | 0.52 | 3.8/0.0/4.0 | 18.4/0.7/17.7 | 0.93 \pm 0.12 | 1.1E-17/7.7E-15 | OoF | ... | ... | ... | ... |
| 79 | 2 | 18:43:29.70 | -3 50 15.1 | 0.31 | 5.5/0.0/2.6 | 20.1/2.8/16.7 | 0.71 \pm 0.17 | 1.2E-17/8.4E-15 | S5359 | 0.30 | ... | ... | 12.90 |
| 80 | 2 | 18:43:30.20 | -3 51 18.2 | 0.21 | 4.5/4.0/0.0 | 9.2/7.8/1.4 | -0.70 \pm 0.28 | 2.8E-16/1.1E-15 | No | ... | ... | ... | ... |
| 81 | 2 | 18:43:30.21 | -3 53 44.3 | 0.17 | 4.2/4.7/0.0 | 9.9/9.5/0.5 | -0.90 \pm 0.19 | 3.4E-16/1.4E-16 | S5569/J18433019-0353440 | 0.33 | 15.37 | 14.73 | 14.50 |
| 82 | 2 | 18:43:30.27 | -3 54 11.4 | 0.05 | 49.2/42.1/10.7 | 103.5/82.4/20.9 | -0.60 \pm 0.08 | 3.7E-15/1.5E-14 | S5602/J18433026-0354110 | 0.39 | 13.11 | 12.07 | 11.67 |
| 83 | 1/2 | 18:43:30.35 | -3 59 43.3 | 0.43 | 0.0/5.0/0.0 | 15.8/15.8/0.0 | -1.00 \pm 0.11 | 3.5E-16/1.4E-16 | No | ... | ... | ... | ... |
| 84 ^T | 1 | 18:43:30.52 | -4 03 50.3 | 0.48 | 6.4/6.0/0.0 | 33.1/25.5/7.8 | -0.53 \pm 0.17 | 7.3E-16/3.0E-15 | No | ... | ... | ... | ... |
| 85 | 2 | 18:43:30.63 | -3 53 52.0 | 0.14 | 5.4/5.8/0.0 | 10.5/10.5/0.0 | -1.00 \pm 0.18 | 3.5E-16/1.4E-16 | S5758/J18433062-0353515 | 0.29 | 11.93 | 11.26 | 11.00 |
| 86 ^T | 1/2 | 18:43:30.75 | -4 01 02.5 | 0.26 | 16.5/20.5/0.0 | 75.8/74.2/0.9 | -0.97 \pm 0.03 | 2.2E-15/9.0E-16 | S5825/J18433077-0401025 | 0.41 | 9.67 ^b | 9.40 ^b | 9.27 ^b |
| 87 | 1 | 18:43:30.80 | -4 00 45.9 | 0.65 | 4.3/4.5/0.0 | 19.0/18.9/0.0 | -1.00 \pm 0.13 | 5.6E-16/2.3E-16 | S5840/J18433081-0400459 | 0.35 | 15.51 | 14.83 | ... |
| 88 | 2 | 18:43:31.28 | -3 50 29.1 | 0.23 | 12.6/2.8/9.3 | 37.7/11.8/25.1 | 0.36 \pm 0.16 | 2.4E-16/7.2E-15 | No | ... | ... | ... | ... |
| 89 | 2 | 18:43:31.30 | -3 46 18.0 | 0.70 | 6.4/7.6/0.0 | 34.6/34.8/-0.0 | -1.00 \pm 0.07 | 9.5E-16/3.8E-16 | OoF | ... | ... | ... | ... |
| 90 | 2 | 18:43:31.47 | -3 55 15.8 | 0.23 | 4.9/2.9/0.0 | 10.0/5.6/4.5 | -0.11 \pm 0.33 | 2.2E-17/6.7E-16 | S6146 | 0.48 | 16.98 | 15.82 | 15.53 |
| 91 | 1/2 | 18:43:31.59 | -3 56 49.4 | 0.11 | 14.9/14.0/2.4 | 32.0/25.9/6.0 | -0.62 \pm 0.11 | 5.5E-16/2.3E-15 | S6217/J18433157-0356492 | 0.18 | 14.23 | 13.53 | 13.30 |
| 92 | 2 | 18:43:31.68 | -3 48 39.3 | 0.45 | 4.3/4.5/0.0 | 16.8/16.8/0.0 | -1.00 \pm 0.13 | 5.3E-16/2.1E-16 | S6289/J18433170-0348390 | 0.56 | 12.40 | 11.94 | 11.77 |
| 93 | 2 | 18:43:31.72 | -3 59 56.1 | 0.48 | 4.0/0.0/2.7 | 10.9/5.7/5.2 | -0.05 \pm 0.32 | 5.0E-17/1.5E-15 | No | ... | ... | ... | ... |
| 94 | 2 | 18:43:31.75 | -3 51 26.7 | 0.15 | 10.7/9.3/1.9 | 26.1/19.9/6.1 | -0.53 \pm 0.17 | 5.7E-16/2.4E-15 | S6293/J18433170-0351268 | 0.55 | 15.21 | 14.20 | 13.41 |
| 95 | 2 | 18:43:31.76 | -3 57 39.3 | 0.15 | 13.2/3.7/11.0 | 34.0/8.3/25.7 | 0.51 \pm 0.16 | 2.4E-16/7.1E-15 | No | ... | ... | ... | ... |
| 96 | 2 | 18:43:31.78 | -3 57 17.2 | 0.20 | 4.3/3.8/0.0 | 9.5/7.9/1.6 | -0.66 \pm 0.27 | 1.7E-16/6.9E-16 | S6318 | 0.07 | 15.47 | 15.63 | 13.93 |
| 97 | 2 | 18:43:32.27 | -3 54 44.7 | 0.16 | 6.9/6.2/0.0 | 16.0/14.6/1.5 | -0.81 \pm 0.17 | 4.5E-16/1.8E-16 | No | ... | ... | ... | ... |
| 98 | 1/2 | 18:43:32.41 | -4 00 50.4 | 0.39 | 5.2/5.7/0.0 | 14.0/12.9/1.2 | -0.85 \pm 0.18 | 3.9E-16/1.6E-16 | S6584/J18433236-0400507 | 0.70 | 15.78 | 15.04 | ... |

Table 1—Continued

| ID ^a | AO | R.A. | Dec. | Error (arcsec) | Significance | Normalized counts | Hardness (H-S)/(H+S) | Flux | NIR counterpart | | | | |
|------------------|-----|--------------------------|-------------|-------------------|---------------------------------|---------------------------------|-------------------------|--|--------------------------|------------------------|----------------|----------------|-------------------|
| | | (hh:mm:ss.ss) (J2000) | (d:mm:ss.s) | | (σ) Total/Soft/Hard | (cnts/100ks) Total/Soft/Hard | | (ergs s ⁻¹ cm ⁻²) 0.5-2keV/2-10keV | ID ^b | separation (arcsec) | J^c (mag) | H^c (mag) | K_S^c (mag) |
| 99 | 1 | 18:43:32.47 | -4 08 49.7 | 0.51 | 9.9/0.0/10.1 | 77.3/13.0/64.7 | 0.67 ±0.10 | 3.4E-17/2.5E-14 | OoF | ... | ... | ... | ... |
| 100 | 1 | 18:43:32.58 | -4 04 18.7 | 0.21 | 31.3/19.7/23.9 | 222.8/99.3/125.0 | 0.11 ±0.07 | 1.6E-15/4.7E-14 | J18433257-0404190 | 0.32 | 15.14 | 12.55 | 11.14 |
| 101 | 2 | 18:43:32.67 | -3 49 07.6 | 0.37 | 4.5/0.0/5.1 | 16.0/0.0/15.7 | 1.00 ±0.14 | 8.1E-18/5.9E-15 | No | ... | ... | ... | ... |
| 102 | 2 | 18:43:33.36 | -3 54 36.0 | 0.17 | 4.6/3.9/0.0 | 9.3/7.7/1.6 | -0.66 ±0.27 | 2.4E-16/9.8E-16 | S7035 | 0.05 | 16.53 | 15.47 | 15.01 |
| 103 | 2 | 18:43:33.41 | -3 50 19.5 | 0.20 | 11.2/11.6/1.8 | 32.7/30.2/2.6 | -0.84 ±0.10 | 7.0E-16/2.8E-16 | S7055/J18433338-0350200 | 0.58 | 15.24 | 14.15 | 13.52 |
| 104 | 1 | 18:43:33.47 | -4 03 54.3 | 0.51 | 3.6/4.5/0.0 | 25.2/17.5/7.8 | -0.38 ±0.21 | 6.3E-16/2.6E-15 | J18433350-0403541 | 0.52 | 11.62 | 10.71 | 10.35 |
| 105 | 2 | 18:43:33.94 | -3 52 53.0 | 0.12 | 4.7/0.0/3.9 | 6.5/0.7/5.5 | 0.77 ±0.30 | 4.5E-18/3.3E-15 | S7294/J18433392-0352529 | 0.08 | ... | 14.89 | 13.09 |
| 106 | 2 | 18:43:34.12 | -3 55 23.8 | 0.15 | 7.0/7.2/0.0 | 13.6/13.6/0.0 | -1.00 ±0.15 | 2.8E-16/1.1E-16 | S7436 | 0.45 | 15.25 | 14.47 | 14.10 |
| 107 | 2 | 18:43:34.13 | -3 50 47.5 | 0.32 | 3.7/4.3/0.0 | 9.0/8.2/0.8 | -0.82 ±0.21 | 2.3E-16/9.3E-17 | S7413 | 0.24 | 16.95 | 16.15 | ... |
| 108 | 1 | 18:43:34.63 | -4 10 32.2 | 0.92 | 3.8/0.0/5.0 | 24.2/7.0/17.3 | 0.43 ±0.21 | 1.3E-16/3.8E-15 | OoF | ... | ... | ... | ... |
| 109 | 2 | 18:43:34.79 | -3 46 04.2 | 0.70 | 4.4/4.5/0.0 | 28.5/26.8/1.7 | -0.88 ±0.11 | 8.6E-16/3.5E-16 | OoF | ... | ... | ... | ... |
| 110 | 1/2 | 18:43:35.33 | -4 00 44.7 | 0.35 | 7.1/7.4/0.0 | 20.3/16.7/3.7 | -0.66 ±0.13 | 5.0E-16/2.1E-15 | S8090/J18433529-0400448 | 0.48 | 15.61 | 14.66 | 14.44 |
| 111 | 2 | 18:43:35.38 | -3 55 56.6 | 0.13 | 4.1/4.4/0.0 | 8.5/8.7/-0.3 | -1.00 ±0.03 | 2.4E-16/9.6E-17 | S8139 | 0.32 | 16.63 | 16.96 | ... |
| 112 | 2 | 18:43:35.41 | -3 57 14.8 | 0.25 | 4.9/5.0/0.0 | 10.7/10.5/0.2 | -0.96 ±0.19 | 2.5E-16/1.0E-16 | S8164 | 0.08 | 16.42 | 15.38 | 14.93 |
| 113 | 1/2 | 18:43:35.45 | -4 01 12.7 | 0.34 | 10.1/1.9/7.9 | 34.5/9.2/25.6 | 0.53 ±0.10 | 1.8E-16/5.4E-15 | S8192 | 0.35 | 16.40 | 15.69 | 13.51 |
| 114 | 2 | 18:43:35.48 | -3 58 46.1 | 0.29 | 4.6/3.1/3.3 | 17.3/9.3/8.0 | -0.07 ±0.25 | 6.4E-17/1.9E-15 | S8194/J18433545-0358456 | 0.27 | 14.74 | 14.01 | 13.68 |
| 115 | 2 | 18:43:35.59 | -3 46 00.8 | 0.58 | 6.2/6.0/0.0 | 60.7/51.5/9.3 | -0.69 ±0.10 | 1.2E-15/5.0E-15 | OoF | ... | ... | ... | ... |
| 116 | 2 | 18:43:35.82 | -3 58 54.4 | 0.29 | 4.9/4.6/0.0 | 13.1/11.4/1.9 | -0.72 ±0.20 | 1.5E-16/6.1E-16 | S8433/J18433584-0358539 | 0.68 | 14.35 | 13.66 | 13.34 |
| 117 | 2 | 18:43:35.84 | -3 46 52.7 | 0.33 | 20.1/9.5/17.5 | 143.1/39.9/103.1 | 0.44 ±0.08 | 8.9E-16/2.7E-14 | OoF | ... | ... | ... | ... |
| 118 | 2 | 18:43:35.89 | -3 57 58.7 | 0.24 | 6.1/6.5/0.0 | 14.8/14.6/0.1 | -0.99 ±0.14 | 2.5E-16/1.0E-16 | S8454/J18433588-0357587 | 0.10 | 15.77 | 14.87 | 14.49 |
| 119 | 1/2 | 18:43:36.18 | -4 01 54.2 | 0.38 | 5.6/6.3/0.0 | 12.1/12.1/0.0 | -1.00 ±0.16 | 4.2E-16/1.7E-16 | S8621 | 0.94 | 16.09 | 15.59 | ... |
| 120 | 2 | 18:43:36.39 | -3 55 50.1 | 0.13 | 5.1/0.0/6.0 | 9.6/0.0/9.5 | 1.00 ±0.21 | 5.9E-18/4.3E-15 | No | ... | ... | ... | ... |
| 121 | 2 | 18:43:36.43 | -3 55 53.7 | 0.15 | 5.5/1.5/4.8 | 12.3/2.7/9.5 | 0.56 ±0.25 | 1.6E-16/4.8E-15 | No | ... | ... | ... | ... |
| 122 | 1/2 | 18:43:36.74 | -3 57 47.9 | 0.21 | 6.7/7.8/0.0 | 21.8/19.1/2.6 | -0.82 ±0.11 | 5.2E-16/2.1E-16 | S8957/J18433676-0357478 | 0.32 | 15.52 | 14.71 | 14.38 |
| 123 | 2 | 18:43:36.85 | -3 54 29.4 | 0.19 | 6.6/6.9/0.0 | 14.5/14.3/0.3 | -0.96 ±0.13 | 4.1E-16/1.7E-16 | S9010 | 0.27 | 16.65 | 15.09 | 16.12 |
| 124 | 1 | 18:43:37.01 | -4 02 34.5 | 0.45 | 4.3/2.9/0.0 | 15.1/13.0/2.2 | -0.71 ±0.21 | 1.9E-16/7.7E-16 | No | ... | ... | ... | ... |
| 125 | 2 | 18:43:37.67 | -3 57 44.4 | 0.28 | 3.8/4.4/0.0 | 9.5/9.5/0.0 | -1.00 ±0.21 | 3.1E-16/1.2E-16 | S9480/J18433767-0357442 | 0.29 | 11.92 | 11.25 | 11.02 |
| 126 ^T | 1 | 18:43:37.87 | -4 03 53.2 | 0.25 | 16.6/4.7/14.6 | 75.7/21.8/55.1 | 0.43 ±0.11 | 5.8E-16/1.8E-14 | No | ... | ... | ... | ... |
| 127 | 1 | 18:43:38.17 | -4 09 46.9 | 0.37 | 10.8/12.6/0.0 | 51.1/48.9/2.3 | -0.91 ±0.07 | 1.8E-15/7.1E-16 | J18433817-0409465 | 0.39 | 14.43 | 12.65 | 11.81 |
| 128 | 2 | 18:43:38.28 | -3 52 01.1 | 0.18 | 4.8/5.6/0.0 | 9.6/9.7/0.0 | -1.00 ±0.20 | 4.2E-16/1.7E-16 | S9809/J18433826-0352012 | 0.30 | 15.73 | 14.74 | 14.32 |
| 129 | 1 | 18:43:38.59 | -4 05 58.7 | 0.37 | 4.8/5.1/0.0 | 19.2/15.6/3.7 | -0.62 ±0.22 | 5.5E-16/2.3E-15 | No | ... | ... | ... | ... |
| 130 | 2 | 18:43:38.63 | -3 57 32.7 | 0.19 | 7.9/7.9/0.0 | 19.0/17.7/1.3 | -0.86 ±0.14 | 3.0E-16/1.2E-16 | S10021 | 0.38 | 16.06 | 15.13 | 14.84 |
| 131 ^T | 2 | 18:43:38.73 | -3 48 34.4 | 0.35 | 6.1/3.4/4.9 | 38.5/24.5/13.9 | -0.28 ±0.16 | 5.7E-16/2.4E-15 | No | ... | ... | ... | ... |
| 132 | 2 | 18:43:39.02 | -3 54 44.0 | 0.14 | 6.3/6.6/0.0 | 13.0/12.5/0.6 | -0.91 ±0.14 | 3.6E-16/1.4E-16 | S10269 | 0.19 | ... | 17.09 | ... |
| 133 | 2 | 18:43:39.04 | -3 52 45.9 | 0.06 | 57.2/56.8/5.8 | 159.0/138.6/20.5 | -0.74 ±0.05 | 2.9E-15/1.2E-14 | S10275/J18433902-0352459 | 0.25 | 13.16 | 12.21 | 11.88 |
| 134 | 2 | 18:43:39.04 | -3 52 13.6 | 0.16 | 7.7/8.5/0.0 | 18.1/17.8/0.4 | -0.96 ±0.11 | 6.9E-16/2.8E-16 | S10271/J18433901-0352138 | 0.45 | 12.51 | 12.01 | 11.88 |
| 135 | 2 | 18:43:39.26 | -3 52 52.5 | 0.14 | 12.0/13.1/0.0 | 28.6/28.6/0.2 | -0.99 ±0.07 | 9.7E-16/3.9E-16 | S10406/J18433923-0352523 | 0.41 | 10.38 | 10.21 | 9.85 ^b |
| 136 | 1 | 18:43:39.26 | -4 07 02.5 | 0.46 | 4.7/0.0/3.8 | 16.6/2.5/14.1 | 0.70 ±0.22 | 1.0E-17/7.5E-15 | No | ... | ... | ... | ... |
| 137 | 2 | 18:43:39.38 | -3 49 53.7 | 0.17 | 30.1/2.1/34.0 | 146.5/7.8/135.7 | 0.89 ±0.04 | 7.3E-17/5.3E-14 | No | ... | ... | ... | ... |
| 138 | 1 | 18:43:39.51 | -4 05 14.2 | 0.22 | 15.8/2.0/15.7 | 62.0/9.4/52.8 | 0.70 ±0.10 | 3.5E-17/2.6E-14 | No | ... | ... | ... | ... |
| 139 | 2 | 18:43:39.76 | -3 54 08.8 | 0.15 | 8.2/8.8/0.0 | 20.6/19.4/1.3 | -0.87 ±0.12 | 6.3E-16/2.5E-16 | S10699 | 0.42 | 16.24 | 15.36 | 15.04 |
| 140 | 2 | 18:43:40.34 | -3 51 54.3 | 0.22 | 4.7/4.6/0.0 | 12.9/10.7/2.3 | -0.65 ±0.24 | 2.8E-16/1.1E-15 | S11045/J18434031-0351544 | 0.11 | 14.41 | 14.60 | 14.36 |
| 141 | 1 | 18:43:40.60 | -4 03 42.1 | 0.36 | 6.8/5.2/1.3 | 20.4/13.8/6.8 | -0.34 ±0.23 | 3.2E-16/1.3E-15 | No | ... | ... | ... | ... |
| 142 | 2 | 18:43:40.95 | -3 49 54.9 | 0.42 | 2.7/4.1/0.0 | 10.9/10.9/0.1 | -0.98 ±0.19 | 2.8E-16/1.2E-16 | No | ... | ... | ... | ... |
| 143 | 1/2 | 18:43:41.02 | -3 58 02.3 | 0.32 | 3.9/4.3/0.0 | 16.8/14.2/2.6 | -0.80 ±0.18 | 3.7E-16/1.5E-15 | S11475/J18434103-0358024 | 0.27 | 12.20 | 11.18 | 10.73 |
| 144 | 1/2 | 18:43:41.13 | -3 57 40.6 | 0.11 | 36.9/32.7/9.4 | 62.4/55.2/7.8 | -0.73 ±0.08 | 1.6E-15/6.6E-15 | S11523/J18434111-0357404 | 0.19 | 12.92 | 12.10 | 11.77 |
| 145 | 2 | 18:43:41.51 | -3 50 55.0 | 0.27 | 4.5/0.0/2.5 | 11.4/5.3/6.1 | 0.07 ±0.32 | 9.7E-17/2.9E-15 | No | ... | ... | ... | ... |
| 146 | 1 | 18:43:41.81 | -4 11 18.6 | 0.53 | 4.0/0.0/5.1 | 16.7/0.0/16.9 | 1.00 ±0.15 | 1.1E-17/7.9E-15 | OoF | ... | ... | ... | ... |
| 147 | 2 | 18:43:42.17 | -3 57 59.0 | 0.22 | 6.3/6.2/0.0 | 16.9/14.8/1.2 | -0.85 ±0.17 | 2.7E-16/1.1E-16 | S12123 | 0.40 | 15.35 | 14.59 | 14.30 |

Table 1—Continued

| ID ^a | AO | R.A. | Dec. | Error | Significance | Normalized counts | Hardness | Flux | NIR counterpart | | | | |
|------------------|-----|--------------------------|-------------|----------|---------------------------------|---------------------------------|------------------|--|--------------------------|------------------------|----------------|----------------|------------------|
| | | (hh:mm:ss.ss) (J2000) | (d:mm:ss.s) | (arcsec) | (σ) Total/Soft/Hard | (cnts/100ks) Total/Soft/Hard | (H-S)/(H+S) | (ergs s ⁻¹ cm ⁻²) 0.5-2keV/2-10keV | ID ^b | separation (arcsec) | J^c (mag) | H^c (mag) | K_S^c (mag) |
| 148 | 2 | 18:43:42.37 | -3 55 07.4 | 0.15 | 6.0/5.9/0.0 | 12.1/11.6/0.6 | -0.91 \pm 0.15 | 3.4E-16/1.4E-16 | S12222 | 0.24 | 17.84 | 16.60 | 16.11 |
| 149 | 1/2 | 18:43:42.57 | -3 59 41.1 | 0.26 | 6.0/5.8/0.0 | 18.0/11.8/6.2 | -0.32 \pm 0.17 | 4.0E-16/1.6E-15 | S12331 | 0.70 | 15.46 | 14.64 | 14.45 |
| 150 | 2 | 18:43:42.73 | -3 54 24.7 | 0.16 | 9.3/8.7/0.0 | 22.5/18.3/4.0 | -0.64 \pm 0.17 | 5.1E-16/2.1E-15 | S12469 | 0.21 | 17.76 | 15.88 | 15.61 |
| 151 | 2 | 18:43:43.26 | -3 51 56.9 | 0.22 | 12.6/0.0/13.3 | 47.9/5.1/41.7 | 0.78 \pm 0.10 | 2.6E-17/1.9E-14 | No | ... | ... | ... | ... |
| 152 | 1 | 18:43:43.42 | -4 04 51.1 | 0.27 | 3.7/4.1/0.0 | 9.9/9.9/0.0 | -1.00 \pm 0.23 | 3.6E-16/1.5E-16 | No | ... | ... | ... | ... |
| 153 | 2 | 18:43:43.80 | -3 47 33.2 | 0.48 | 6.7/7.1/0.0 | 44.6/36.6/6.9 | -0.68 \pm 0.12 | 1.0E-15/4.2E-15 | OoF | ... | ... | ... | ... |
| 154 | 1 | 18:43:45.01 | -4 03 34.5 | 0.26 | 4.8/4.6/0.0 | 11.9/10.6/1.4 | -0.77 \pm 0.25 | 4.8E-16/2.0E-15 | S14192 | 0.65 | ... | 15.87 | ... |
| 155 | 1 | 18:43:45.04 | -4 05 01.6 | 0.16 | 17.2/17.6/2.7 | 52.9/44.8/8.1 | -0.69 \pm 0.11 | 1.1E-15/4.5E-15 | S14243/J18434503-0405015 | 0.17 | ... | 13.54 | 13.11 |
| 156 | 2 | 18:43:45.35 | -3 53 16.7 | 0.25 | 4.6/3.8/0.0 | 17.0/11.2/5.8 | -0.32 \pm 0.24 | 3.9E-16/1.6E-15 | S14512/J18434537-0353163 | 0.60 | 14.67 | 14.02 | 13.75 |
| 157 | 1 | 18:43:45.87 | -4 07 39.6 | 0.32 | 4.5/5.1/0.0 | 14.1/13.4/0.7 | -0.90 \pm 0.16 | 2.2E-16/8.7E-17 | S14852/J18434586-0407387 | 0.83 | 15.33 | 14.44 | ... |
| 158 | 2 | 18:43:46.06 | -3 53 51.8 | 0.17 | 5.7/6.6/0.0 | 16.0/15.7/0.4 | -0.95 \pm 0.12 | 4.5E-16/1.8E-16 | S15011/J18434607-0353521 | 0.12 | 15.75 | 14.74 | 14.44 |
| 159 | 1 | 18:43:46.08 | -4 03 24.6 | 0.21 | 4.0/4.6/0.0 | 8.6/8.6/0.0 | -1.00 \pm 0.26 | 2.2E-16/9.0E-17 | S15029/J18434610-0403248 | 0.38 | 14.51 | 13.91 | 13.63 |
| 160 | 1 | 18:43:46.08 | -4 05 48.7 | 0.23 | 5.8/6.2/0.0 | 15.5/15.2/0.3 | -0.96 \pm 0.14 | 4.7E-16/1.9E-16 | S15003/J18434605-0405488 | 0.49 | 14.07 | 13.30 | 13.04 |
| 161 | 2 | 18:43:46.43 | -3 54 11.6 | 0.23 | 5.1/6.2/0.0 | 13.3/13.4/0.0 | -1.00 \pm 0.15 | 4.9E-16/2.0E-16 | S15282/J18434644-0354117 | 0.33 | 14.21 | 13.53 | 13.36 |
| 162 | 1 | 18:43:46.62 | -4 04 30.1 | 0.11 | 22.9/0.0/25.3 | 67.8/1.4/66.4 | 0.96 \pm 0.05 | 3.8E-17/2.8E-14 | No | ... | ... | ... | ... |
| 163 | 2 | 18:43:46.66 | -3 46 23.8 | 0.78 | 3.8/5.6/0.0 | 24.8/24.7/0.0 | -1.00 \pm 0.09 | 8.8E-16/3.6E-16 | OoF | ... | ... | ... | ... |
| 164 | 2 | 18:43:46.72 | -3 54 43.5 | 0.21 | 4.5/3.7/0.0 | 10.1/7.6/2.5 | -0.51 \pm 0.29 | 2.0E-16/8.1E-16 | S15492/J18434671-0354434 | 0.06 | 15.42 | 14.14 | 13.38 |
| 165 ^T | 1 | 18:43:46.79 | -4 07 06.3 | 0.29 | 7.9/6.9/0.0 | 21.8/16.7/5.1 | -0.53 \pm 0.20 | 4.6E-16/1.9E-15 | No | ... | ... | ... | ... |
| 166 ^T | 1 | 18:43:46.81 | -4 01 25.7 | 0.18 | 12.2/12.8/0.0 | 37.0/33.5/3.5 | -0.81 \pm 0.12 | 6.5E-16/2.7E-16 | S15573/J18434683-0401264 | 0.83 | 12.20 | 11.32 | 11.05 |
| 167 | 1 | 18:43:46.96 | -4 10 32.7 | 0.31 | 9.3/8.8/3.0 | 37.6/30.3/7.3 | -0.61 \pm 0.15 | 8.9E-16/3.7E-15 | S15657/J18434694-0410326 | 0.36 | 14.90 | 13.81 | 13.41 |
| 168 | 1 | 18:43:47.10 | -4 08 40.6 | 0.37 | 5.8/4.2/0.0 | 17.8/10.7/7.0 | -0.21 \pm 0.26 | 1.9E-16/7.7E-16 | No | ... | ... | ... | ... |
| 169 | 2 | 18:43:47.11 | -3 53 18.3 | 0.18 | 10.3/9.8/0.0 | 28.3/22.4/5.9 | -0.58 \pm 0.15 | 7.0E-16/2.9E-15 | S15778/J18434709-0353182 | 0.11 | 15.65 | 14.60 | 14.23 |
| 170 | 1 | 18:43:47.37 | -4 08 30.4 | 0.17 | 23.7/27.2/0.0 | 89.8/89.7/0.2 | -0.99 \pm 0.03 | 2.3E-15/9.5E-16 | S15972/J18434736-0408301 | 0.32 | ... | 12.36 | 12.23 |
| 171 ^T | 1 | 18:43:47.55 | -4 04 06.1 | 0.19 | 5.2/3.8/1.5 | 13.8/8.5/5.2 | -0.24 \pm 0.29 | 2.9E-16/1.2E-15 | No | ... | ... | ... | ... |
| 172 | 1/2 | 18:43:47.63 | -3 56 10.3 | 0.18 | 13.5/14.4/0.0 | 46.1/33.7/12.3 | -0.44 \pm 0.12 | 9.6E-16/3.9E-15 | S16177/J18434762-0356105 | 0.20 | 15.70 | 14.84 | 14.66 |
| 173 | 1/2 | 18:43:47.79 | -3 59 19.0 | 0.29 | 6.1/0.0/6.5 | 18.3/1.3/16.4 | 0.85 \pm 0.12 | 1.1E-17/8.2E-15 | No | ... | ... | ... | ... |
| 174 | 2 | 18:43:48.04 | -3 53 57.5 | 0.26 | 6.0/0.0/6.8 | 22.3/2.7/19.3 | 0.76 \pm 0.15 | 1.3E-17/9.3E-15 | No | ... | ... | ... | ... |
| 175 | 1 | 18:43:48.08 | -4 03 03.4 | 0.28 | 4.4/0.0/4.2 | 10.9/1.6/9.2 | 0.71 \pm 0.27 | 5.5E-18/4.0E-15 | No | ... | ... | ... | ... |
| 176 | 1 | 18:43:48.67 | -4 01 36.1 | 0.10 | 37.6/40.3/4.7 | 134.8/122.4/12.4 | -0.82 \pm 0.05 | 1.7E-15/6.8E-16 | S16952/J18434867-0401362 | 0.13 | 14.42 | 13.61 | 13.37 |
| 177 ^T | 1 | 18:43:48.72 | -4 01 17.6 | 0.32 | 4.5/3.1/0.0 | 16.8/10.2/6.5 | -0.22 \pm 0.26 | 1.2E-16/5.0E-16 | No | ... | ... | ... | ... |
| 178 | 1/2 | 18:43:49.03 | -3 59 57.1 | 0.24 | 7.4/7.1/4.7 | 30.6/17.9/12.6 | -0.35 \pm 0.12 | 4.4E-16/1.8E-15 | S17276 | 0.92 | 16.55 | 14.65 | 13.68 |
| 179 | 1 | 18:43:49.11 | -4 02 56.4 | 0.18 | 4.3/4.2/0.0 | 10.4/8.5/1.8 | -0.66 \pm 0.27 | 3.5E-16/1.4E-15 | S17301 | 0.22 | 16.95 | 15.48 | 14.93 |
| 180 | 1 | 18:43:49.21 | -4 00 54.1 | 0.30 | 5.4/2.5/3.8 | 14.2/4.4/9.8 | 0.39 \pm 0.27 | 5.0E-17/1.5E-15 | No | ... | ... | ... | ... |
| 181 ^T | 2 | 18:43:49.22 | -3 52 38.3 | 0.22 | 15.2/14.2/3.7 | 61.8/46.1/15.8 | -0.49 \pm 0.11 | 1.2E-15/4.9E-15 | S17370 | 0.46 | 16.88 | 16.10 | 15.67 |
| 182 | 1 | 18:43:49.39 | -4 04 13.7 | 0.18 | 8.5/4.2/5.1 | 21.1/9.5/11.7 | 0.11 \pm 0.24 | 1.7E-16/5.1E-15 | No | ... | ... | ... | ... |
| 183 | 1 | 18:43:50.42 | -4 02 29.5 | 0.17 | 4.0/4.3/0.0 | 9.7/9.7/0.0 | -1.00 \pm 0.22 | 2.5E-16/1.0E-16 | S18344/J18435042-0402294 | 0.11 | 13.87 | 13.21 | 12.95 |
| 184 | 1 | 18:43:50.51 | -4 02 07.2 | 0.17 | 4.7/4.1/0.0 | 11.5/9.8/1.9 | -0.68 \pm 0.24 | 3.1E-16/1.3E-15 | S18402 | 0.19 | 16.71 | 15.36 | 14.93 |
| 185 | 1/2 | 18:43:50.67 | -3 58 52.1 | 0.31 | 2.7/4.0/0.0 | 7.9/7.2/0.6 | -0.84 \pm 0.24 | 2.6E-16/1.1E-16 | S18522/J18435067-0358526 | 0.62 | 14.97 | 14.37 | 14.13 |
| 186 | 1/2 | 18:43:50.71 | -3 57 38.8 | 0.33 | 7.0/0.0/7.3 | 33.9/6.9/27.0 | 0.65 \pm 0.10 | 1.9E-17/1.4E-14 | No | ... | ... | ... | ... |
| 187 | 2 | 18:43:51.09 | -3 52 39.1 | 0.18 | 21.4/25.0/0.0 | 82.9/82.0/0.9 | -0.98 \pm 0.02 | 2.4E-15/9.8E-16 | S18799 | 0.29 | ... | 10.90 | ... |
| 188 | 1/2 | 18:43:51.81 | -3 59 22.3 | 0.21 | 13.6/12.6/2.2 | 38.0/30.8/7.2 | -0.62 \pm 0.10 | 9.2E-16/3.8E-15 | S19355/J18435181-0359222 | 0.03 | 14.93 | 14.01 | 13.54 |
| 189 | 1 | 18:43:52.37 | -4 07 29.9 | 0.20 | 7.4/6.8/0.0 | 19.0/16.3/2.7 | -0.71 \pm 0.19 | 5.1E-16/2.1E-15 | No | ... | ... | ... | ... |
| 190 | 2 | 18:43:52.78 | -3 53 59.3 | 0.35 | 5.8/4.0/0.0 | 23.0/18.4/4.6 | -0.60 \pm 0.18 | 4.4E-16/1.8E-15 | No | ... | ... | ... | ... |
| 191 | 1/2 | 18:43:52.78 | -4 00 50.1 | 0.24 | 7.9/8.6/0.0 | 24.4/20.1/4.8 | -0.49 \pm 0.13 | 5.0E-16/2.0E-15 | S20105 | 0.67 | 16.39 | 15.19 | 14.62 |
| 192 | 1 | 18:43:52.85 | -4 04 11.4 | 0.21 | 4.4/2.4/0.0 | 10.1/8.4/1.7 | -0.66 \pm 0.28 | 3.1E-16/1.3E-15 | No | ... | ... | ... | ... |
| 193 | 1/2 | 18:43:53.11 | -3 57 59.8 | 0.30 | 5.5/7.2/0.0 | 25.0/19.1/6.0 | -0.57 \pm 0.14 | 5.3E-16/2.2E-15 | S20390/J18435312-0357594 | 0.48 | 13.47 | 12.93 | 12.71 |
| 194 | 2 | 18:43:53.58 | -3 51 16.3 | 0.42 | 5.0/6.8/0.0 | 33.9/26.4/7.6 | -0.55 \pm 0.16 | 8.9E-16/3.7E-15 | No | ... | ... | ... | ... |
| 195 | 1/2 | 18:43:54.18 | -3 58 44.0 | 0.43 | 0.0/4.9/0.0 | 14.4/10.2/4.2 | -0.59 \pm 0.18 | 2.8E-16/1.2E-15 | S21144 | 0.37 | 16.28 | 15.41 | 15.09 |
| 196 | 1/2 | 18:43:54.56 | -3 58 06.3 | 0.34 | 6.2/6.2/0.0 | 39.7/28.0/11.7 | -0.41 \pm 0.11 | 6.4E-16/2.7E-15 | No | ... | ... | ... | ... |

Table 1—Continued

| ID ^a | AO | R.A. | Dec. | Error (arcsec) | Significance | Normalized counts | Hardness (H-S)/(H+S) | Flux | NIR counterpart | | | | |
|------------------|-----|--------------------------|-------------|-------------------|---------------------------------|---------------------------------|-------------------------|--|--------------------------|------------------------|-------------------|-------------------|-------------------|
| | | (hh:mm:ss.ss) (J2000) | (d:mm:ss.s) | | (σ) Total/Soft/Hard | (cnts/100ks) Total/Soft/Hard | | (ergs s ⁻¹ cm ⁻²) 0.5-2keV/2-10keV | ID ^b | separation (arcsec) | J^c (mag) | H^c (mag) | K_S^c (mag) |
| 197 | 1/2 | 18:43:54.61 | -3 56 41.5 | 0.27 | 14.0/9.9/5.7 | 80.5/37.6/42.3 | 0.07 \pm 0.08 | 5.2E-16/1.6E-14 | No | ... | ... | ... | ... |
| 198 | 2 | 18:43:54.65 | -3 53 36.5 | 0.43 | 5.3/5.6/0.0 | 20.9/18.5/2.4 | -0.77 \pm 0.16 | 6.0E-16/2.5E-15 | S21470/J18435466-0353364 | 0.34 | 15.67 | 14.70 | 14.23 |
| 199 | 1 | 18:43:54.83 | -4 07 42.0 | 0.14 | 22.0/24.4/0.0 | 77.8/73.4/4.5 | -0.88 \pm 0.06 | 1.9E-15/7.6E-16 | S21566 | 0.42 | 14.31 | 13.57 | 13.32 |
| 200 | 1/2 | 18:43:55.10 | -3 58 29.6 | 0.11 | 90.8/23.3/91.4 | 577.7/73.8/501.4 | 0.74 \pm 0.02 | 2.3E-16/1.7E-13 | No | ... | ... | ... | ... |
| 201 | 1 | 18:43:55.15 | -4 04 20.1 | 0.15 | 7.2/7.6/0.0 | 15.1/15.1/0.0 | -1.00 \pm 0.15 | 5.0E-16/2.0E-16 | S21808 | 0.36 | 13.04 | 13.42 | 12.04 |
| 202 | 2 | 18:43:55.42 | -3 52 52.9 | 0.21 | 21.7/18.8/11.8 | 98.7/55.3/42.4 | -0.13 \pm 0.10 | 8.0E-16/2.4E-14 | No | ... | ... | ... | ... |
| 203 | 2 | 18:43:55.69 | -3 57 04.3 | 0.49 | 4.3/0.0/5.0 | 25.6/2.5/22.9 | 0.80 \pm 0.14 | 1.2E-17/8.7E-15 | S22226 | 0.39 | 18.57 | 17.23 | ... |
| 204 | 2 | 18:43:55.70 | -3 52 50.2 | 0.30 | 10.1/0.0/8.0 | 45.6/18.2/26.4 | 0.18 \pm 0.15 | 3.7E-16/1.1E-14 | S22272 | 0.93 | 17.37 | 16.05 | 15.34 |
| 205 | 1 | 18:43:55.78 | -4 08 25.8 | 0.29 | 5.2/6.7/0.0 | 18.9/16.8/2.0 | -0.78 \pm 0.16 | 4.0E-16/1.6E-15 | No | ... | ... | ... | ... |
| 206 | 2 | 18:43:55.90 | -3 55 03.9 | 0.40 | 4.4/3.4/0.0 | 39.2/28.8/10.4 | -0.47 \pm 0.15 | 5.8E-16/2.4E-15 | No | ... | ... | ... | ... |
| 207 | 1 | 18:43:56.59 | -4 06 08.0 | 0.13 | 7.2/0.0/6.3 | 11.6/0.9/10.7 | 0.85 \pm 0.18 | 7.5E-18/5.4E-15 | No | ... | ... | ... | ... |
| 208 ^E | 2 | 18:43:56.68 | -3 54 47.8 | 0.25 | 16.8/17.4/3.1 | 238.3/197.9/40.6 | -0.66 \pm 0.05 | 2.7E-15/1.1E-14 | No | ... | ... | ... | ... |
| 209 | 1/2 | 18:43:56.90 | -3 57 33.5 | 0.37 | 5.6/7.4/0.0 | 18.2/18.2/0.0 | -1.00 \pm 0.10 | 5.5E-16/2.2E-16 | No | ... | ... | ... | ... |
| 210 ^E | 2 | 18:43:56.90 | -3 54 37.0 | 0.30 | 8.4/0.0/0.0 | 125.1/86.8/38.4 | -0.39 \pm 0.09 | 1.6E-15/6.5E-15 | No | ... | ... | ... | ... |
| 211 | 1 | 18:43:57.35 | -4 01 23.3 | 0.21 | 5.5/2.4/2.8 | 14.3/4.9/9.2 | 0.30 \pm 0.28 | 1.2E-16/3.5E-15 | No | ... | ... | ... | ... |
| 212 | 2 | 18:43:57.68 | -3 51 57.1 | 0.53 | 5.3/4.1/0.0 | 29.9/17.1/12.9 | -0.14 \pm 0.19 | 2.0E-16/6.0E-15 | S23609 | 0.90 | 16.90 | 15.44 | 14.77 |
| 213 ^E | 2 | 18:43:57.87 | -3 54 45.9 | 0.31 | 6.4/0.0/4.2 | 188.3/126.2/61.1 | -0.35 \pm 0.07 | 1.8E-15/7.4E-15 | No | ... | ... | ... | ... |
| 214 | 1 | 18:43:57.87 | -4 07 37.7 | 0.10 | 23.3/24.6/0.0 | 60.5/58.9/1.6 | -0.95 \pm 0.05 | 2.7E-15/1.1E-15 | S23783/J18435787-0407379 | 0.37 | 12.82 | 12.12 | 11.95 |
| 215 | 1/2 | 18:43:57.91 | -3 59 19.8 | 0.34 | 7.4/3.0/4.9 | 12.4/6.3/6.2 | 0.00 \pm 0.23 | 1.2E-16/3.7E-15 | No | ... | ... | ... | ... |
| 216 ^E | 2 | 18:43:57.92 | -3 54 37.5 | 0.34 | 8.5/5.4/0.0 | 123.9/93.1/30.7 | -0.50 \pm 0.08 | 1.4E-15/5.9E-15 | No | ... | ... | ... | ... |
| 217 | 1 | 18:43:58.30 | -4 03 21.2 | 0.16 | 4.5/3.9/0.0 | 10.3/8.4/1.8 | -0.65 \pm 0.26 | 2.6E-16/1.1E-15 | S24066 | 0.35 | 16.81 | 15.44 | 14.80 |
| 218 | 1/2 | 18:43:58.53 | -3 56 21.6 | 0.31 | 9.4/2.1/9.0 | 36.8/8.6/28.3 | 0.53 \pm 0.12 | 2.4E-16/7.3E-15 | No | ... | ... | ... | ... |
| 219 | 2 | 18:43:59.02 | -3 51 15.7 | 0.55 | 6.7/7.2/1.7 | 26.5/26.2/0.2 | -0.98 \pm 0.08 | 1.0E-15/4.1E-16 | No | ... | ... | ... | ... |
| 220 | 2 | 18:43:59.28 | -3 50 26.2 | 0.81 | 4.4/5.1/0.0 | 36.2/30.7/6.7 | -0.64 \pm 0.13 | 8.7E-16/3.6E-15 | OoF | ... | ... | ... | ... |
| 221 | 2 | 18:43:59.67 | -3 55 18.3 | 0.41 | 10.0/10.5/0.0 | 59.6/55.4/4.3 | -0.86 \pm 0.08 | 1.7E-15/6.8E-16 | S25062/J18435965-0355183 | 0.21 | 9.30 ^b | 8.93 ^b | 8.76 ^b |
| 222 | 1 | 18:43:59.92 | -4 07 21.5 | 0.23 | 5.2/2.4/0.0 | 11.9/8.2/3.6 | -0.39 \pm 0.30 | 2.4E-16/1.0E-15 | No | ... | ... | ... | ... |
| 223 | 1 | 18:44:00.31 | -4 05 59.2 | 0.13 | 8.4/7.6/0.0 | 19.8/17.1/2.7 | -0.73 \pm 0.17 | 5.0E-16/2.0E-15 | S25554/J18440036-0405594 | 0.81 | 13.59 | 12.37 | 11.91 |
| 224 ^T | 1 | 18:44:01.13 | -3 57 40.7 | 0.55 | 5.8/5.4/0.0 | 24.1/21.3/2.9 | -0.76 \pm 0.16 | 2.7E-16/1.1E-15 | S26066 | 0.61 | 16.59 | 15.38 | 14.74 |
| 225 | 1 | 18:44:01.93 | -4 05 11.7 | 0.19 | 4.4/3.4/0.0 | 10.1/7.2/2.7 | -0.46 \pm 0.31 | 2.1E-16/8.5E-16 | No | ... | ... | ... | ... |
| 226 | 1 | 18:44:02.16 | -4 05 23.7 | 0.11 | 20.8/22.4/0.0 | 56.2/56.3/0.4 | -0.99 \pm 0.04 | 1.7E-15/6.8E-16 | S26833/J18440213-0405243 | 0.93 | 14.18 | 13.41 | 13.15 |
| 227 | 1 | 18:44:02.44 | -4 12 44.8 | 0.89 | 4.7/0.0/4.8 | 19.1/0.0/19.3 | 1.00 \pm 0.13 | 5.6E-18/4.0E-15 | OoF | ... | ... | ... | ... |
| 228 | 2 | 18:44:02.45 | -3 51 51.7 | 0.68 | 4.0/3.5/0.0 | 26.7/16.8/10.0 | -0.25 \pm 0.20 | 4.5E-16/1.8E-15 | No | ... | ... | ... | ... |
| 229 | 1 | 18:44:02.54 | -4 09 22.3 | 0.19 | 18.5/2.0/19.3 | 77.2/10.8/65.0 | 0.72 \pm 0.09 | 4.0E-17/2.9E-14 | S27070/J18440256-0409228 | 0.38 | ... | 13.67 | 12.26 |
| 230 | 1/2 | 18:44:03.27 | -3 58 19.0 | 0.27 | 21.0/23.4/0.0 | 66.3/66.0/0.2 | -0.99 \pm 0.03 | 1.9E-15/7.8E-16 | S27370/J18440331-0358188 | 0.63 | 13.15 | 12.48 | 12.23 |
| 231 | 1 | 18:44:03.47 | -4 10 41.8 | 0.50 | 5.8/2.4/3.2 | 25.5/17.6/7.8 | -0.39 \pm 0.20 | 2.8E-16/1.2E-15 | No | ... | ... | ... | ... |
| 232 | 1 | 18:44:03.84 | -4 11 23.6 | 0.70 | 4.2/0.0/4.4 | 23.2/7.6/15.5 | 0.34 \pm 0.22 | 1.8E-16/5.4E-15 | OoF | ... | ... | ... | ... |
| 233 ^T | 1 | 18:44:03.95 | -4 02 57.6 | 0.10 | 31.2/11.8/24.4 | 90.3/29.3/57.5 | 0.32 \pm 0.11 | 6.3E-16/1.9E-14 | S27641/J18440392-0402577 | 0.43 | ... | 14.22 | 13.40 |
| 234 | 2 | 18:44:03.97 | -3 54 06.6 | 0.73 | 5.8/6.1/4.7 | 44.2/24.3/19.9 | -0.10 \pm 0.16 | 2.8E-16/8.3E-15 | OoF | ... | ... | ... | ... |
| 235 ^T | 1 | 18:44:05.05 | -4 04 36.9 | 0.10 | 25.2/13.1/15.0 | 64.9/31.0/32.7 | 0.03 \pm 0.13 | 6.7E-16/2.0E-14 | S28081 | 0.80 | 17.40 | 15.35 | ... |
| 236 | 1 | 18:44:05.41 | -4 08 32.4 | 0.14 | 24.5/25.4/0.0 | 89.4/84.5/5.0 | -0.89 \pm 0.05 | 2.3E-15/9.3E-16 | S28203/J18440540-0408325 | 0.17 | 14.98 | 14.31 | 14.07 |
| 237 | 1 | 18:44:05.56 | -4 05 39.1 | 0.19 | 6.4/4.8/0.0 | 15.1/10.4/4.6 | -0.39 \pm 0.26 | 3.8E-16/1.6E-15 | S28248 | 0.52 | 16.59 | 15.28 | 14.87 |
| 238 | 1 | 18:44:05.91 | -4 06 12.2 | 0.10 | 21.0/18.8/3.9 | 51.6/42.5/9.0 | -0.65 \pm 0.11 | 1.1E-15/4.6E-15 | S28382/J18440589-0406124 | 0.53 | 14.27 | 13.36 | 13.10 |
| 239 | 1 | 18:44:06.10 | -4 08 43.5 | 0.22 | 5.7/6.3/0.0 | 19.7/18.4/1.3 | -0.87 \pm 0.15 | 5.2E-16/2.1E-16 | No | ... | ... | ... | ... |
| 240 | 1 | 18:44:06.35 | -4 07 04.0 | 0.20 | 5.6/0.0/5.6 | 13.6/0.8/12.5 | 0.88 \pm 0.16 | 8.4E-18/6.1E-15 | No | ... | ... | ... | ... |
| 241 | 1 | 18:44:07.60 | -4 05 14.1 | 0.17 | 8.5/0.0/6.7 | 21.7/2.8/18.3 | 0.74 \pm 0.17 | 1.2E-17/8.4E-15 | No | ... | ... | ... | ... |
| 242 | 2 | 18:44:08.59 | -3 53 55.8 | 0.68 | 6.2/0.0/6.8 | 53.2/4.5/49.7 | 0.84 \pm 0.09 | 3.0E-17/2.2E-14 | OoF | ... | ... | ... | ... |
| 243 | 1 | 18:44:09.49 | -4 07 31.6 | 0.17 | 12.8/0.0/11.8 | 41.0/2.0/37.0 | 0.90 \pm 0.08 | 2.4E-17/1.8E-14 | No | ... | ... | ... | ... |
| 244 | 1 | 18:44:10.98 | -4 05 16.8 | 0.14 | 12.6/4.3/9.3 | 30.8/10.5/20.1 | 0.31 \pm 0.19 | 2.4E-16/7.1E-15 | S30315/J18441095-0405170 | 0.51 | 15.60 | 13.55 | 12.71 |
| 245 | 1 | 18:44:11.89 | -4 05 12.6 | 0.18 | 14.1/0.9/13.1 | 40.3/7.9/31.9 | 0.60 \pm 0.14 | 2.3E-17/1.7E-14 | No | ... | ... | ... | ... |

Table 1—Continued

| ID ^a | AO | R.A. | Dec. | Error | Significance | Normalized counts | Hardness | Flux | NIR counterpart | | | | |
|------------------|----|--------------------------|-------------|----------|---------------------------------|---------------------------------|------------------|--|--------------------------|------------------------|----------------|----------------|------------------|
| | | (hh:mm:ss.ss) (J2000) | (d:mm:ss.s) | (arcsec) | (σ) Total/Soft/Hard | (cnts/100ks) Total/Soft/Hard | (H-S)/(H+S) | (ergs s ⁻¹ cm ⁻²) 0.5-2keV/2-10keV | ID ^b | separation (arcsec) | J^c (mag) | H^c (mag) | K_S^c (mag) |
| 246 | 1 | 18:44:11.90 | -4 06 30.7 | 0.23 | 7.3/4.7/2.3 | 20.3/14.7/5.6 | -0.45 \pm 0.22 | 5.9E-16/2.4E-15 | S30539/J18441188-0406311 | 0.55 | ... | 15.35 | 13.97 |
| 247 | 1 | 18:44:12.17 | -4 08 08.2 | 0.32 | 2.3/0.0/4.1 | 13.0/2.5/10.2 | 0.61 \pm 0.27 | 8.7E-18/6.3E-15 | No | ... | ... | ... | ... |
| 248 | 1 | 18:44:13.16 | -4 06 20.2 | 0.25 | 5.4/0.0/4.1 | 15.2/0.3/13.5 | 0.95 \pm 0.16 | 9.1E-18/6.6E-15 | No | ... | ... | ... | ... |
| 249 ^T | 1 | 18:44:13.72 | -4 02 32.8 | 0.29 | 4.0/2.6/0.0 | 11.5/8.2/3.3 | -0.42 \pm 0.32 | 2.8E-16/1.1E-15 | No | ... | ... | ... | ... |
| 250 | 1 | 18:44:13.77 | -4 12 17.4 | 0.53 | 12.9/0.0/14.9 | 106.2/9.5/97.9 | 0.82 \pm 0.06 | 6.3E-17/4.6E-14 | OoF | ... | ... | ... | ... |
| 251 | 1 | 18:44:14.75 | -4 11 34.7 | 0.44 | 11.0/11.0/2.0 | 64.3/50.6/13.7 | -0.57 \pm 0.12 | 1.4E-15/5.9E-15 | OoF | ... | ... | ... | ... |
| 252 | 1 | 18:44:15.62 | -4 03 56.9 | 0.31 | 6.5/2.8/4.0 | 22.0/9.4/12.4 | 0.14 \pm 0.24 | 1.6E-16/4.9E-15 | S31107/J18441558-0403569 | 0.55 | 16.96 | 14.59 | 13.60 |
| 253 | 1 | 18:44:15.73 | -4 08 58.0 | 0.49 | 4.6/0.0/4.2 | 18.3/5.8/12.4 | 0.36 \pm 0.25 | 1.7E-16/5.1E-15 | No | ... | ... | ... | ... |
| 254 | 1 | 18:44:16.25 | -4 12 57.0 | 0.82 | 5.7/0.0/3.5 | 40.4/7.7/33.4 | 0.62 \pm 0.14 | 2.4E-17/1.7E-14 | OoF | ... | ... | ... | ... |
| 255 | 1 | 18:44:18.54 | -4 06 02.5 | 0.29 | 8.3/6.2/3.9 | 37.1/27.2/9.8 | -0.47 \pm 0.16 | 8.8E-16/3.6E-15 | S31539/J18441855-0406027 | 0.35 | 13.54 | 12.59 | 12.11 |
| 256 | 1 | 18:44:21.13 | -3 57 06.3 | 0.33 | 26.1/25.6/10.6 | 312.3/244.1/66.3 | -0.57 \pm 0.05 | 5.4E-15/2.2E-14 | OoF | ... | ... | ... | ... |
| 257 | 1 | 18:44:21.60 | -4 04 53.2 | 0.40 | 5.5/3.7/3.3 | 29.1/14.0/15.0 | 0.03 \pm 0.21 | 3.3E-16/1.0E-14 | S31826 | 0.25 | ... | 15.35 | 14.57 |
| 258 | 1 | 18:44:21.77 | -4 12 30.1 | 0.48 | 14.5/12.7/6.7 | 179.3/124.8/55.4 | -0.39 \pm 0.08 | 3.1E-15/1.3E-14 | OoF | ... | ... | ... | ... |
| 259 | 1 | 18:44:22.57 | -3 59 39.8 | 0.57 | 6.1/7.2/0.0 | 55.6/39.1/16.5 | -0.40 \pm 0.14 | 9.8E-16/4.0E-15 | OoF | ... | ... | ... | ... |
| 260 ^T | 1 | 18:44:22.61 | -4 03 51.0 | 0.35 | 11.8/12.4/0.0 | 65.3/57.5/7.7 | -0.76 \pm 0.09 | 1.5E-15/6.2E-15 | S31912/J18442259-0403518 | 0.85 | 14.80 | 13.52 | 13.57 |
| 261 | 1 | 18:44:22.63 | -4 00 40.0 | 0.50 | 6.7/0.0/8.2 | 42.8/0.0/42.9 | 1.00 \pm 0.06 | 2.7E-17/1.9E-14 | OoF | ... | ... | ... | ... |
| 262 | 1 | 18:44:22.67 | -4 00 17.4 | 0.50 | 6.7/6.5/0.0 | 43.3/33.5/9.8 | -0.55 \pm 0.15 | 7.0E-16/2.9E-15 | J18442265-0400176 | 0.30 | 14.36 | 13.39 | 12.52 |
| 263 | 1 | 18:44:23.45 | -4 03 08.5 | 0.50 | 5.1/0.0/3.3 | 23.8/3.7/20.0 | 0.69 \pm 0.18 | 1.1E-17/8.2E-15 | No | ... | ... | ... | ... |
| 264 | 1 | 18:44:24.09 | -3 59 11.9 | 0.57 | 11.6/11.7/3.6 | 95.2/75.6/19.8 | -0.59 \pm 0.09 | 1.8E-15/7.5E-15 | J18442406-0359111 | 0.86 | 13.59 | 12.69 | 12.37 |
| 265 | 1 | 18:44:24.24 | -4 01 35.1 | 0.52 | 5.4/5.2/0.0 | 28.3/24.0/4.2 | -0.70 \pm 0.16 | 7.7E-16/3.2E-15 | J18442423-0401343 | 0.72 | 16.00 | 14.70 | 13.83 |
| 266 | 1 | 18:44:26.23 | -3 57 48.8 | 0.54 | 11.8/13.9/0.0 | 118.7/118.4/0.0 | -1.00 \pm 0.02 | 2.7E-15/1.1E-15 | OoF | ... | ... | ... | ... |
| 267 | 1 | 18:44:26.45 | -4 06 35.5 | 0.47 | 5.7/4.7/0.0 | 28.3/20.8/7.6 | -0.47 \pm 0.19 | 5.1E-16/2.1E-15 | No | ... | ... | ... | ... |
| 268 | 1 | 18:44:26.66 | -4 04 50.1 | 0.53 | 4.1/3.5/0.0 | 15.0/13.1/2.1 | -0.73 \pm 0.21 | 3.0E-16/1.2E-15 | S32241 | 0.80 | 15.61 | 14.58 | 14.12 |
| 269 | 1 | 18:44:26.71 | -4 03 27.3 | 0.46 | 9.8/10.5/0.0 | 61.5/53.8/7.6 | -0.75 \pm 0.10 | 1.2E-15/4.8E-15 | No | ... | ... | ... | ... |
| 270 | 1 | 18:44:27.75 | -4 07 49.3 | 0.55 | 4.3/4.0/0.0 | 30.1/24.8/5.2 | -0.65 \pm 0.16 | 8.2E-16/3.4E-15 | OoF | ... | ... | ... | ... |
| 271 | 1 | 18:44:28.51 | -4 08 15.3 | 0.63 | 6.2/3.8/4.1 | 36.3/14.3/22.2 | 0.22 \pm 0.18 | 2.9E-16/8.8E-15 | OoF | ... | ... | ... | ... |
| 272 | 1 | 18:44:28.87 | -4 01 03.9 | 0.48 | 14.3/12.1/8.3 | 142.0/85.8/57.2 | -0.20 \pm 0.09 | 8.2E-16/2.5E-14 | J18442884-0401033 | 0.60 | 13.29 | 11.83 | 11.11 |
| 273 | 1 | 18:44:30.35 | -4 10 44.5 | 0.50 | 16.6/7.9/15.6 | 164.6/33.8/134.5 | 0.60 \pm 0.07 | 9.4E-17/6.8E-14 | J18443035-0410445 | 0.12 | 17.37 | 15.68 | 13.90 |
| 274 | 1 | 18:44:32.73 | -4 07 04.4 | 0.58 | 9.2/9.8/0.0 | 55.9/55.7/0.0 | -1.00 \pm 0.05 | 1.9E-15/7.6E-16 | OoF | ... | ... | ... | ... |

^aSources with *T* in the ID column show significant time variations, and those with *E* are extended.

^bSOFI ID in Table 1 (starts with S) and/or 2MASS ID (starts with J) of the NIR source within 1'' from the Chandra position. "No" means that the source is in the SOFI field of view, but there are no SOFI counterparts. "OoF" means that the source is out of the SOFI field, and no 2MASS counterparts.

^c2MASS magnitudes are taken for stars brighter than 10 mag, since SOFI starts to saturate for < 10 mag (see Fig. 5).

Table 2. SOFI NIR source catalog.

| ID | R.A. (J2000) | Decl. (J2000) | J (mag) | H (mag) | K_S (mag) | 2MASS ID | Chandra ID |
|-------|--------------|---------------|--------------|--------------|----------------|------------------|------------|
| 1 | 18:43:08.380 | −03:54:34.12 | −999 | 17.64 | 15.58 | ... | ... |
| 2 | 18:43:08.382 | −03:52:29.29 | 16.69 | 15.33 | 15.09 | ... | ... |
| 3 | 18:43:08.382 | −03:53:46.51 | 17.37 | 16.56 | 16.40 | ... | ... |
| ... | | | | | | | |
| 8 | 18:43:08.451 | −03:54:07.29 | −999 | 16.04 | 14.56 | 18430845−0354075 | ... |
| ... | | | | | | | |
| 687 | 18:43:15.299 | −03:54:19.16 | 10.45 | 10.15 | 10.03 | 18431530−0354190 | 24 |
| ... | | | | | | | |
| 1018 | 18:43:17.438 | −03:57:32.71 | 16.54 | 15.25 | 15.13 | ... | 30 |
| ... | | | | | | | |
| 32397 | 18:44:28.474 | −04:06:50.97 | 15.72 | 13.80 | 12.64 | ... | ... |
| 32398 | 18:44:28.477 | −04:04:33.27 | −999 | −999 | 15.18 | ... | ... |

Note. — We have detected 32,398 sources from our SOFI fields (Fig. 3). For each source, the position, J , H and K_S magnitudes, and the 2MASS and/or *Chandra* counterparts are given. When not detected, −999 is put for the magnitude. The *Chandra* source identification number is defined in Table 1. The complete version of this table is in the electronic edition of the Journal. The printed edition contains only a sample.

Table 3. Summary of the point source characteristics.

| hardness ratio | soft ≤ -0.60 | Medium -0.59 to 0.1 | Hard ≥ 0.11 | Total |
|--------------------------------|----------------------|----------------------------|---------------------|---------------|
| All | 137 | 68 | 69 | 274 |
| Extended ^a | 1 | 3 | 0 | 4 |
| Point Source | 136 | 65 | 69 | 270 |
| Time variation ^b | 4 (3 %) | 10 (15 %) | 3 (4 %) | 17 (6 %) |
| 2MASS counterpart ^b | 62 (45 %) | 17 (26 %) | 8 (12 %) | 87 (32 %) |
| Covered by SOFI ^b | 106 (78 %) | 47 (72 %) | 49 (71 %) | 202 (75 %) |
| SOFI counterpart ^c | 88 (83 %) | 25 (53 %) | 11 (22 %) | 124 (61 %) |
| NIR counterpart ^d | 98 (72 %) | 30 (46 %) | 14 (20 %) | 142 (53 %) |

^aSources associated with the thermal blob-like feature CXOU J184357-035441 (Ueno et al. 2003).

^bThe percentage gives the fraction among all the point sources, excluding the extended sources. Note that the 2MASS covers the entire *Chandra* field, but SOFI does not.

^cThe percentage gives the fraction among the point sources covered by SOFI.

^dPresence of either 2MASS or SOFI counterparts. The percentage gives the fraction among all the point sources.

Table 4. Spectral fitting results of the average spectra with absorbed power-law model

| hardness ratio | Soft ≤ -0.60 | Medium -0.59 to 0.1 | Hard ≥ 0.11 |
|--|----------------------|----------------------------|---------------------|
| <i>Sources with NIR counterparts</i> | | | |
| N_H (10^{22} cm $^{-2}$) | 0.50 ± 0.05 | 0.9 ± 0.1 | 3.5 ± 0.4 |
| photon-index | $2.8^{+0.2}_{-0.1}$ | 2.0 ± 0.2 | 0.90^d |
| N^a | 1.5 ± 0.2 | $1.6^{+0.4}_{-0.3}$ | 1.34 ± 0.11 |
| reduced χ^2 (dof) | 1.7 (181) | 0.99 (137) | 1.2 (62) |
| observed flux ^b (0.5 – 10 keV) | 2.1 | 4.7 | 17 |
| intrinsic flux ^c (0.5 – 10 keV) | 4.8 | 7.8 | 23 |
| <i>Sources without NIR counterparts</i> | | | |
| N_H (10^{22} cm $^{-2}$) | 0.50 ± 0.15 | 1.6 ± 0.5 | 5.0 ± 0.8 |
| photon-index | 2.8^d | 2.0^d | $0.9^{+0.1}_{-0.3}$ |
| N^a | 0.85 ± 0.2 | 2.9 ± 0.3 | $1.8^{+0.9}_{-0.7}$ |
| reduced χ^2 (dof) | 1.7 (29) | 1.1 (45) | 1.27 (170) |
| observed flux ^b (0.5 – 10 keV) | 1.2 | 7.1 | 23 |
| intrinsic flux ^c (0.5 – 10 keV) | 2.7 | 13 | 33 |

^aPower-law normalization in 10^{-6} photons s $^{-1}$ keV $^{-1}$ cm $^{-2}$ at 1 keV.

^bAverage source flux in units of 10^{-15} erg s $^{-1}$ cm $^{-2}$.

^cIntrinsic source flux in units of 10^{-15} erg s $^{-1}$ cm $^{-2}$ when hydrogen column density is set to null.

^dFixed to the best-fit value obtained for the other group in the same spectral hardness with/without NIR counterpart.

Note. — Errors correspond to 90 % confidence.

Table 5. Spectral fitting results of the average spectra with physical models

| | With NIR counterparts | Without NIR counterparts |
|---|--------------------------|-----------------------------|
| <i>Soft spectra</i> (two MEKAL model) | | |
| Overall normalization ^a | 1.0 | 0.52 |
| N_H (10^{22} cm ⁻²) | 1.19 ± 0.15 | |
| kT (keV; soft) | 0.25 ± 0.02 | |
| N^b (soft) | 56 | |
| kT (keV; hard) | 2.2 ± 0.5 | |
| N^b (hard) | 2.8 | |
| reduced χ^2 (dof) | 1.35 (179) | 1.85 (30) |
| <i>Medium spectra</i> (two MEKAL model) | | |
| N_H (10^{22} cm ⁻²) | 1.4 ± 0.3 | ... |
| kT (keV; soft) | 0.23 ± 0.10 | ... |
| N^b (soft) | 68 | ... |
| kT (keV; hard) | 3.0 ± 0.4 | ... |
| N^b (hard) | 5.5 | ... |
| reduced χ^2 (dof) | 1.21 (89) | ... |
| <i>Hard spectra</i> (power-law with iron line and edge) | | |
| N_H (10^{22} cm ⁻²) | 4.5 ± 0.3 | 4.8 ± 0.6 |
| photon-index | 1.47 ± 0.03 | 0.77 ± 0.20 |
| N^c | 3.26 | 1.57 |
| E_{line} (keV) | 6.67 ± 0.08 | 6.71 ± 0.08 |
| Line intrinsic width (keV) | < 0.05 | 0.18 ± 0.11 |
| Line equivalent width (eV) | 540 ± 200 | 340 ± 270 |
| E_{edge} (keV) | ... | 7.11 (frozen) |
| Edge depth | ... | 1.2 ± 0.5 |
| reduced χ^2 (dof) | 1.06 (59) | 1.28 (67) |

^aThe same two temperature MEKAL model parameters are used for the soft spectra with or without the NIR counterparts with the exception of the overall normalization. Hydrogen density of the plasma is fixed to $n_H = 1$ cm⁻³. Parameter errors are for the spectrum with NIR counterparts.

^bMEKAL model normalization, $10^{-20}/4\pi d^2 \int n_e n_H dV$, where d is distance (cm), n_e and n_H are electron and hydrogen densities (in cm⁻³), respectively.

^cPower-law normalization in 10^{-6} photons s⁻¹ keV⁻¹ cm⁻² at 1 keV.

Note. — Errors correspond to 90 % confidence. The spectral model for the medium sources without NIR

counterpart is given in Table 4.

Table 6. Iron line parameters of the Galactic diffuse emission

| | Energy (keV) | Line flux (photons s ⁻¹ cm ⁻² str ⁻¹) | Equivalent width (eV) | Identification |
|--------------------------------------|--------------------------|--|--------------------------|------------------------------------|
| <i>Single line model^a</i> | | | | |
| | 6.52 $\pm_{0.14}^{0.08}$ | 0.55 \pm 0.39 | 170 \pm 120 | NEI plasma? |
| <i>Three line model^b</i> | | | | |
| | 6.40 (fixed) | 0.6 $\pm_{0.6}^{0.3}$ | 100 \pm_{100}^{50} | Fluorescence from low-ionized iron |
| | 6.67 (fixed) | 0.4 $\pm_{0.3}^{0.8}$ | 180 \pm_{140}^{360} | He-like iron |
| | 6.97 (fixed) | 0.5 $\pm_{0.5}^{0.8}$ | 160 \pm_{160}^{260} | H-like iron |

^aReduced $\chi^2 = 0.83$ with dof=4.

^bReduced $\chi^2 = 1.19$ with dof=3.

Note. — Errors correspond to 90 % confidence. Intrinsic line width is fixed to zero, assuming that the lines are narrower than the instrumental width (~ 100 eV).

Table 7. Low energy line parameters of the Galactic diffuse emission

| Energy (keV) | Line flux (photons/s/cm ² /str) | Equivalent width (eV) | Identification |
|-----------------------------|---|--------------------------|--------------------------------|
| $1.021 \pm_{0.002}^{0.009}$ | $0.60 \pm_{0.11}^{0.14}$ | $64 \pm_{12}^{15}$ | Ne X, Ly α (1.02 keV) |
| $1.13 \pm_{0.03}^{0.07}$ | $0.12 \pm_{0.09}^{0.12}$ | $13 \pm_{10}^{13}$ | Fe L? |
| $1.32 \pm_{0.01}^{0.02}$ | 0.32 ± 0.08 | 36 ± 10 | Mg XI, K α (1.35 keV) |
| $1.46 \pm_{0.03}^{0.04}$ | $0.11 \pm_{0.08}^{0.11}$ | $12 \pm_9^{12}$ | Mg XII, Ly α (1.47 keV) |
| $1.74 \pm_{0.04}^{0.06}$ | < 0.32 | < 25 | Low ionized Si? |
| $1.849 \pm_{0.017}^{0.003}$ | $0.87 \pm_{0.46}^{0.17}$ | $110 \pm_{10}^{20}$ | Si XIII, K α (1.86 keV) |
| 2.00 (fixed) | $0.05 \pm_{0.05}^{0.11}$ | $6 \pm_6^{13}$ | Si XIV, Ly α (2.00 keV) |
| $2.188 \pm_{0.034}^{0.012}$ | 0.48 ± 0.24 | 60 ± 30 | Instrumental Au M-complex |
| 2.42 ± 0.02 | 0.71 ± 0.15 | 90 ± 20 | S XV, K α (2.45 keV) |
| $2.61 \pm_{0.05}^{0.04}$ | 0.30 ± 0.14 | 40 ± 20 | S XVI, Ly α (2.62 keV) |
| 3.08 ± 0.03 | 0.34 ± 0.12 | 48 ± 17 | Ar XVII, K α (3.12 keV) |

Note. — Reduced $\chi^2 = 1.03$ with dof = 27. Errors correspond to 90 % confidence. Intrinsic line width is fixed to zero, assuming it is narrower than the instrumental width (~ 100 eV).

Table 8. Two NEI model fitting of the Galactic diffuse emission

| | Fixed abundance model | Free abundance model |
|--|-----------------------|----------------------|
| <i>Soft Component</i> | | |
| kT (keV) | 0.86 | 0.59 ± 0.09 |
| $\log n_e t$ ($\text{cm}^{-3} \text{ s}$) | 11.1 | 11.8 ± 0.5 |
| Abundance (except Ne, Mg, Si) | 0.11 | 0.044 ± 0.037 |
| Ne abundance | 0.11 | 0.30 ± 0.2 |
| Mg abundance | 0.11 | 0.14 ± 0.06 |
| Si abundance | 0.11 | 0.25 ± 0.05 |
| N_H (10^{22} cm^{-2}) | 0.75 | 0.81 ± 0.12 |
| Observed flux ^a ($\text{erg cm}^{-2} \text{ s}^{-1} \text{ str}^{-1}$) | 3.1×10^{-8} | 2.6×10^{-8} |
| Intrinsic flux ^a ($\text{erg cm}^{-2} \text{ s}^{-1} \text{ str}^{-1}$) | 1.0×10^{-7} | 1.1×10^{-7} |
| <i>Hard Component</i> | | |
| kT (keV) | 6.52 | 5.0 ± 0.8 |
| $\log n_e t$ ($\text{cm}^{-3} \text{ s}$) | 10.18 | 10.6 ± 0.1 |
| Abundance (except Fe) | 0.23 | 0.17 ± 0.04 |
| Fe abundance | 0.23 | 0.9 ± 0.3 |
| N_H (10^{22} cm^{-2}) | 4.00 | 3.9 ± 0.4 |
| Observed flux ^a ($\text{erg cm}^{-2} \text{ s}^{-1} \text{ str}^{-1}$) | 2.1×10^{-7} | 2.1×10^{-7} |
| Intrinsic flux ^a ($\text{erg cm}^{-2} \text{ s}^{-1} \text{ str}^{-1}$) | 8.1×10^{-7} | 7.6×10^{-7} |
| reduced χ^2 (dof) | 1.97 (68) | 1.52 (64) |

^aIn 0.7 – 10 keV.

Note. — Errors correspond to 90 % confidence.

Table 9. Comparison of the 2–10 keV GRXE fluxes by different satellites

| Satellite | GRXE flux ^a (erg s ⁻¹ cm ⁻² deg ⁻²) | Threshold flux ^a (erg s ⁻¹ cm ⁻²) | Region | Area (deg ²) | Reference |
|----------------|---|--|---|-----------------------------|------------------------|
| <i>ASCA</i> | $5.5 \times 10^{-11b,c}$ | 5×10^{-13d} | $l \approx 28.5, -0.5 \lesssim b \lesssim 2$ | 3.3 | Kaneda et al. (1997) |
| <i>ASCA</i> | 5.2×10^{-11b} | 10^{-11} | $ l \lesssim 35, b \lesssim 0.4$ | 63 | Sugizaki et al. (2001) |
| <i>XMM</i> | 9.6×10^{-11} | 2×10^{-12} | $19 \lesssim l \lesssim 22, b \lesssim 0.6$ | 3 | Hands et al. (2004) |
| <i>XMM</i> | 9.3×10^{-11} | 2×10^{-13} | $19 \lesssim l \lesssim 22, b \lesssim 0.6$ | 3 | Hands et al. (2004) |
| <i>Chandra</i> | 7.4×10^{-11} | 2×10^{-13} | $(l, b) \approx (28.5, 0.0)$ | 0.07 | This work |
| <i>Chandra</i> | 6.5×10^{-11} | 3×10^{-15} | $(l, b) \approx (28.5, 0.0)$ | 0.07 | This work |

^aSources brighter than the threshold flux are excluded in the calculation of the GRXE flux which includes point sources below the threshold and the diffuse emission.

^bAssuming a uniform spatial distribution with 1.°5 radius.

^cCalculated from the best-fit spectral parameters in the paper.

^dTaken from Yamauchi et al. (1996) in the same observation area.